High-Accuracy Torque Control and Estimation for Interior Permanent Magnet Synchronous Machine Drives with Loss Minimization

HIGH-ACCURACY TORQUE CONTROL AND ESTIMATION FOR INTERIOR PERMANENT MAGNET SYNCHRONOUS MACHINE DRIVES WITH LOSS MINIMIZATION

BY

YU MIAO, M.Sc., B.Sc.

A THESIS SUBMITTED TO THE DEPARTMENT OF ELECTRICAL & COMPUTER ENGINEERING AND THE SCHOOL OF GRADUATE STUDIES OF MCMASTER UNIVERSITY IN PARTIAL FULFILMENT OF THE REQUIREMENTS FOR THE DEGREE OF DOCTOR OF PHILOSOPHY

Doctor of Philosophy (2018) McMaster University

(Electrical & Computer Engineering) Hamilton, Ontario, Canada

TITLE: High-Accuracy Torque Control and Estimation for Interior Permanent Magnet Synchronous Machine Drives with Loss Minimization

AUTHOR: Yu Miao

B. Sc., (Electrical Engineering)

M. Sc. (Electrical Engineering)

Northeastern University, Shenyang, China

SUPERVISORS: Dr. Ali Emadi, Dr. Bing Cheng

NUMBER OF PAGES: xx, 166

谨以此献给我的家人

To My Family

Abstract

This thesis studies the high-accuracy torque control for the interior permanent magnet synchronous machine (IPMSM) drives with loss minimization.

A nonlinear flux-linkage model for the IPMSM with twelve coefficients is proposed. It can generally be used to estimate the *d*-axis flux-linkage, *q*-axis flux-linkage, MTPA locus, and torque without the information of the machine known, such as the geometry and material of the permanent magnet. The new torque equation and MTPA condition are derived from the proposed flux-linkage model. An optimization problem is formulated to find the appropriate factors for the proposed model based on the measured flux-linkage data at only nine specific operating points. No selection of weight factors is required in the cost function. The desired copper-loss minimization control can be achieved and good torque estimate can be achieved in real-time.

A novel model for IPMSM drives with all the losses considered is proposed. The model-based loss minimization control (LMC) algorithm with respect to motor current contributing to the flux-linkage generation is presented. The analytical solution to the optimization problem is provided. Based on the proposed IPMSM drive model, LMC with respect to the winding current in wide speed range is studied as well. The optimality is proved. The influences of the stator resistance, the equivalent inverter-loss and core-loss resistance in the proposed circuit are researched. Compared to maximum torque per ampere (MTPA) control, LMC introduces more efficient energy utilization.

Due to the nonlinearities, the characteristics of the inverter loss, the core loss, the mechanical loss, the *d*- and *q*-axis flux-linkage profiles of the IPMSM drive system are researched. The process of the parameters' characterization with respect to the speed, the *d*- and *q*-axis current is stated. The back-fitting based torque estimation technique is proposed, which eliminates the necessity of the manufacture of the dummy rotor. The separation of the core loss and mechanical loss is not required for the calculation. The accuracy of the prediction of the voltage limit ellipse based on the proposed model is enhanced compared to the conventional method. The torque control system for the IPMSM drives is designed, aiming at accurate motor torque control, high efficiency, and fast dynamic response performance.

2004 Prius IPMSM and one prototype motor are used to validate the proposed algorithms for the parameters' characterization, torque estimation, and loss minimization control.

Acknowledgments

First and foremost, I would like to give my sincere gratitude to my supervisor, Dr. Ali Emadi, for his invaluable support, guidance, and patience on me and my research work. It has been my great honor to work with him. His enthusiasm and creativity guided me and will guide me for the rest of my life.

I also would like to thank Dr. Bing Cheng. He encouraged me to pursue higher level of studies and gave me lots of precious suggestions on my research. His wisdom has broadened my vision. I would like to thank my committee meeting members, Dr. Nigel Schofield, Dr. Shahin Sirouspour, Dr. Mehdi Narimani, Dr. Jennifer Bauman, and Dr. Hong Yang, for their insightful comments and stimulating discussions throughout my Ph.D. program. I would also like to thank Dr. Hao Ge, Dr. Matthias Preindl, and Dr. Jin Ye for their advice in my research and generous help with my publications.

I am grateful to my colleagues in the Canada Excellence Research Chair in Hybrid Powertrain Program. Special thanks go to Hao Ge for sharing his expertise and assisting with the experiments. I would like to thank Jin Ye for reading the thesis and for her valuable comments. I want to thank Fei Peng, Jing Guo, Rong Yang, Ran Gu, Yingguang Sun, Shamsuddeen Nalakath, and Yi Huo for giving me valuable advice and inspiration. I will never forget the great time I spent working with Ying Cui, Xiao Wang, Deqiang Wang, Weisheng Jiang, Le Sun, Weizhong Wang, Michael Eull, Ben Danen, and Alan Callegaro. I also would like to thank Jianing Lin, Sandra Castano and Romina Rodriguez

for their kindness and concern. Special thanks go to Teresa Janes, Theresa Mitchell, Cheryl Gies, Dan Manolescu and Phuc Nguyen, who helped organize and coordinate the research needs.

Last but not the least I would like to express my deepest gratitude to my parents, my aunts, and my uncles. I cannot make it without your unconditional love. Thank you for being there for me.

This research was undertaken, in part, thanks to funding from the Canada Excellence Research Chairs Program.

List of Abbreviations

IPMSM	interior permanent magnet synchronous machine
LMC	loss minimization control
MTPA	maximum torque per ampere
MTPV	maximum torque per voltage
MTPF	maximum torque per flux
FW	flux weakening
LTI	linear time invariant
FLC	fuzzy logic controller
RLS	recursive least square
MI	modulation index
3D	three dimensional
4D	four dimensional
LUT	look up table
EMF	electromotive force
PWM	pulse width modulation
IGBT	insulated gate bipolar transistor

ICE	internal combustion engine
LPF	low pass filter
VSI	voltage source inverter
FEA	finite element analysis

Contents

List of Figures

List of Tables

Chapter 1
Introduction

1.1 Motivation

Interior permanent magnet synchronous machines, IPMSMs, shown in Fig. 1.1, are emerging in various applications due to the small volume, light weight, low loss, high efficiency, high power density, and fast dynamic performance [1]–[3]. They have been used in robotics, drivetrain, wind turbine, elevator, compressor, air-conditioner, washing machine, and so on [4]. IPMSMs have additional reluctance torque and are compatible with sensorless techniques [5], [6].

(a)

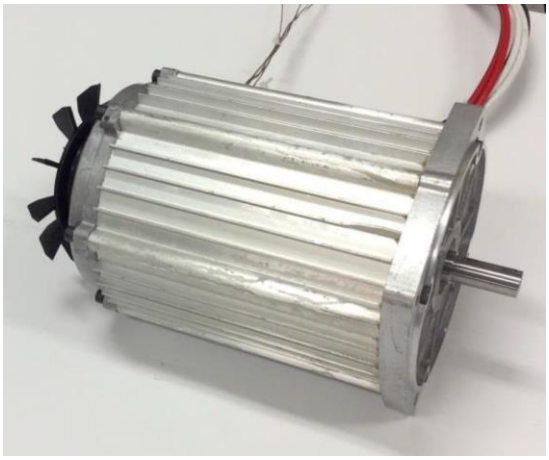

(b)

Fig. 1.1. IPMSM prototype [7]. (a) Lamination of the rotor. (b) Motor with cooling fan.

A good control system is supposed to be stable, have high control accuracy, high efficiency, and fast dynamic response performance. The classical control theory is established upon the linear time-invariant (LTI) systems. Although they are well developed, they cannot be used to control the IPM motor properly. Some characteristics of the IPMSM drives, such as the nonlinearity of the inverter, and the saturation and cross-coupling effects on the flux-linkage profiles, make the motor a nonlinear control object. The classical linear control algorithms cannot satisfy the requirement of high performance for the IPMSM drives, because they cannot adjust themselves to the parameters' variation. For example, the *d*- and *q*-axis inductances can be expressed as the functions of the *d*- and *q*-axis current [8]–[10]. The value of the inductance decreases as the current increases. If only a fixed-gain PI controller is used in the system, the

nonlinearities cannot be compensated and this leads to poor dynamic response or even unstable performance.

Thus, for high-efficiency and high-accuracy control performance for the IPMSM drives, a good control system should include the optimizer, the controller, and the estimator, as shown in Fig. 1.2. For a given command, which is either the motor speed or the output torque, the optimizer offers the optimal current reference. The controller sends out the appropriate signals to the inverter so as to make the motor follow the reference. Based on the feedback information of the current and speed/position, the estimator provides the optimizer and the controller with the estimated motor parameters, such as the flux-linkage profiles, the losses, and even torque information for the torque closed-loop control, to improve the control precision. Due to the fact that the parameters are motor speed and motor current dependent, the estimates are nonlinear functions at different operating conditions. For example, the same current command can lead to different torque outputs due to the existence of the mechanical loss and the core loss at different speeds.

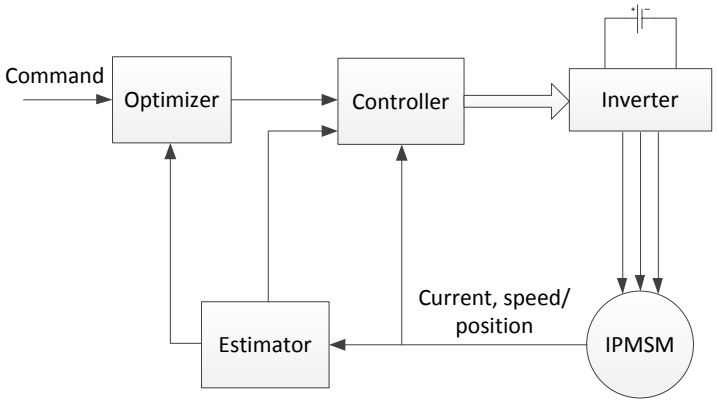

Fig. 1.2. Diagram of the IPMSM drive system.

In order to achieve high operating efficiency, the loss is usually used for the optimization. For given torque and speed the output power is fixed. The maximum efficiency of the IPMSM drives can be achieved only if the loss is minimized. The most common cost function is the copper loss, used for MTPA control [11]. The maximum torque per voltage/flux (MTPV/MTPF) locus encloses the feasible operating region at high speed [12]. The current and voltage constraints limit the range where the current vectors can be selected [13]. Moreover, the core loss and inverter loss are considered during the optimization [14].

The loss minimization control (LMC) can be categorized into two major categories: search-based control and loss-model-based control [15]. The search-based algorithm accomplishes the quest by measuring the input power and changing the control variable in small steps in a certain searching manner at certain load and speed [16]–[23]. For example, the golden section search is used to find the optimal phase angle for LMC by comparing the power losses [19].

In Fig. 1.3, one example of the application of the search-based technique is shown. The authors proposed several fuzzy-logic controllers (FLC) to achieve high efficiency and high performance for IPMSM drive system. The steady-state fuzzy efficiency controller is applied to determine the *d*-axis current reference according to the loss power.

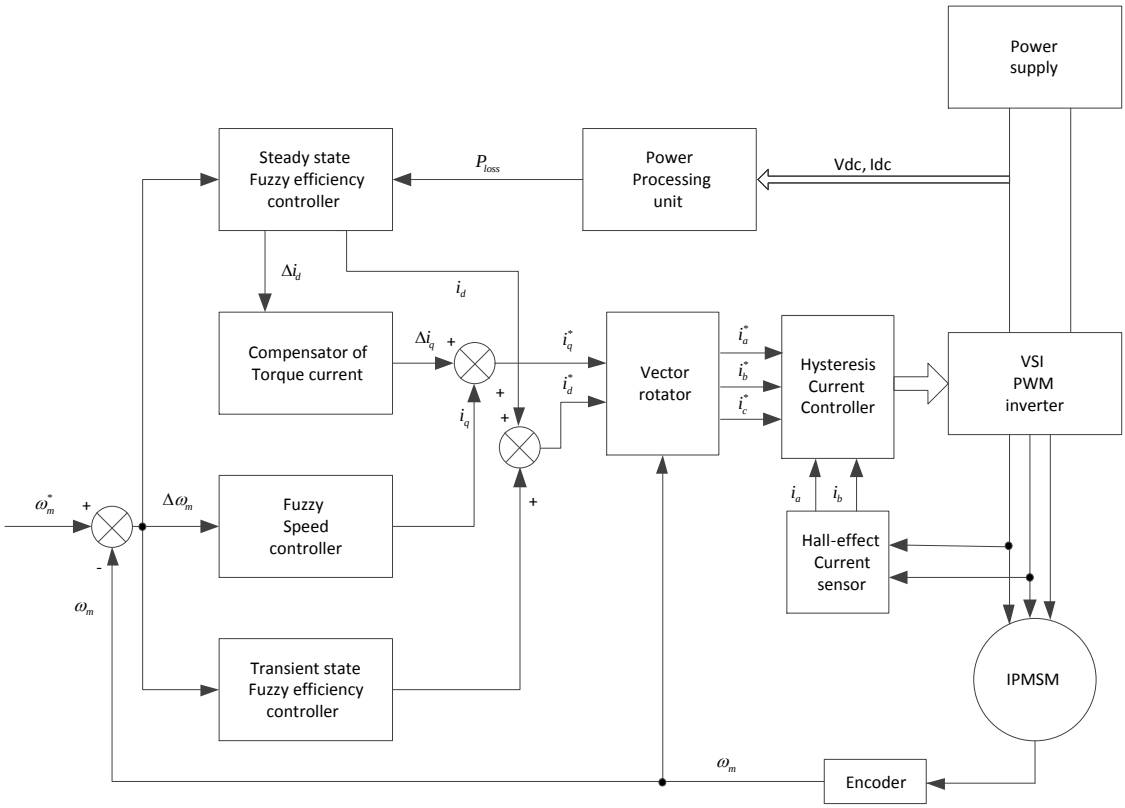

Fig. 1.3. Block diagram of the proposed FLC-based efficiency optimization of IPMSM drive [23].

The search-based technique is independent of the loss model, so it doesn't need the motor parameters to implement the algorithm. Because it drives the motor in small steps this leads to torque ripples, which is not desirable in high-performance drives. Even though the search-based algorithm calculates the output in the right direction, it still takes too much time to try different references in order to find the optimal ones. Furthermore, it is sensitive to the disturbance. The online operation of the search-based algorithm is not secured, because the search result can be located outside of the feasible operating region.

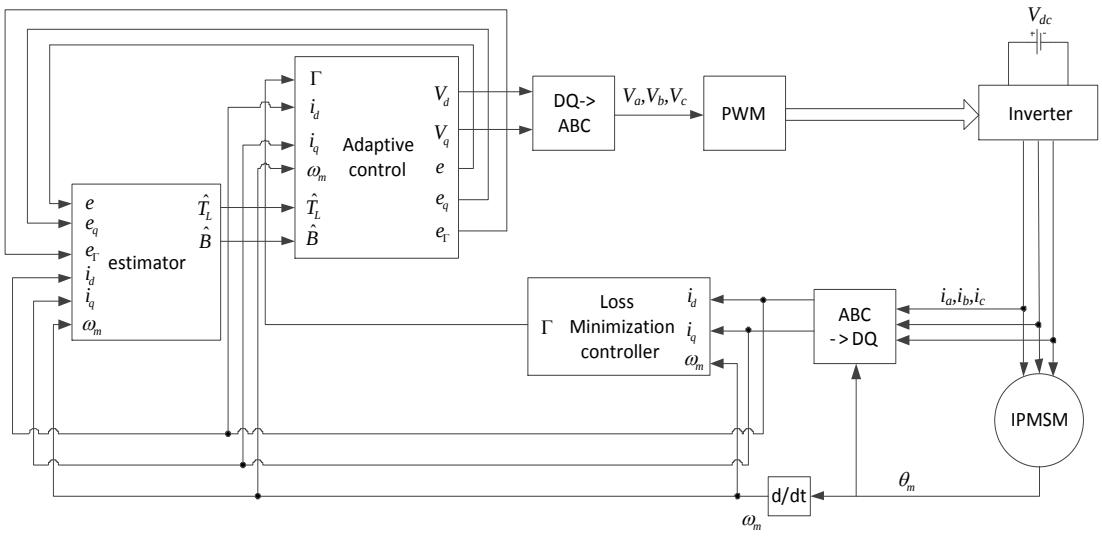

Fig. 1.4. Block diagram of the proposed loss minimization based adaptive backstepping technique for IPMSM drive [24].

The loss model of the IPM machine is adopted in the loss-model-based technique [24]–[29]. The desired commands can be quickly obtained. However, the algorithm suffers from the variation of the parameters, so the researchers also designed the adaptation law for the unknown parameters' estimation, as shown in Fig. 1.4. However, the estimation can only be established upon the model with other known parameters, and actually all the parameters are varying as the operating conditions change.

In one word, the search-based method is not suitable to be used online because it is easy to be disturbed and it is not safe to operate without the voltage limitation at high speed. The existing loss-model-based algorithms have much less searching time, but are not reliable due to the variation of the parameters. If all the nonlinearities in the IPMSM

drive can be identified and used for the optimization and control, the fast, stable, efficient, and accurate control performance can be achieved.

In order to achieve the high-precision and high-efficiency control performance, first of all, the model must be accurate. However, the conventional IPMSM model suffers from precisely depicting the behavior of the machine, because it does not contain all the nonlinearities of the drive system. The same set of the parameters can only fit either the conventional IPMSM's voltage equation or the torque equation. The accuracy of the torque control is influenced by the impact of the inverter loss on the flux-linkage estimation, and by the nonlinearities of the core loss with respect to the motor current and speed. The determination of the optimal current reference is also affected by these factors. Firstly, the total electrical loss is not minimized, because the core loss and the inverter loss are not considered in the conventional IPMSM model. Secondly, optimization constraint is not precisely characterized. If the predicted voltage limit ellipse is bigger than the real constraint, oscillation of control in transient mode could happen, and the feedback controller can be saturated.

In order to identify the nonlinearities of the IPMSM drive, first of all, the flux-linkage profiles must be estimated because they are used for the calculation of the output torque and voltage limitation. The saturation and cross-coupling effects on the flux-linkage generation should be considered [30]. In [31], the recursive least square (RLS) algorithm is used to estimate the stator winding resistance, *d*- and *q*-axis inductance according to the voltage and current commands. However, the voltage command is the desired sinusoidal fundamental component ahead of the inverter's output. The voltage drop across the inverter is supposed to be included in the flux-linkage estimation.

It is also important to identify the core loss of the machine. The loss affects the torque output, especially at high speed. The core loss of an IPMSM consists of the hysteresis loss, eddy current loss and excessive loss [32]–[35]. In literature, some researchers modeled the core loss as the function of the flux-linkage magnitude and the frequency [36]–[43]. However, there are more harmonics contributing to the loss generation [34]. In [44], the no-load torque measured at different speeds is compensated to the output torque, but it only can reflect the sum of the mechanical loss and the core loss generated by the permanent magnet flux-linkage. The indirect methods to separate the core loss from the mechanical loss are proposed in [45], [46]. However, they do not work for IPMSM because the injection of the *d*-axis current can bring more harmonics, instead of only neutralizing the permanent-magnet flux-linkage. To separate the mechanical loss from the core loss, it is more convincing to manufacture a dummy rotor. The unmagnetized rotor has the exact same dimensions with the IPMSM's rotor but does not have the permanent magnet embedded. In this case, the knowledge of the machine itself, such as the rotor's geometry, must be known.

In this thesis, all the issues mentioned above are addressed. Based on the novel IPMSM drive model, all the nonlinearities can be identified through experiment. For given torque and speed, the proposed LMC and torque calculation algorithms enable the IPMSM drives to output the desired torque with minimum loss power within the current and voltage constraints. High-accuracy torque control and fast dynamic response performance of IPMSM drives can be achieved due to the accurate modeling.

1.2 Contributions

The contributions have been made to the high-accuracy torque control for the IPMSM drive system with loss minimization.

Firstly, a novel nonlinear flux-linkage model for IPM machine is proposed, with the saturation and cross-coupling effects considered. The constant coefficients in the model can be determined by using the measured flux-linkage data at only nine specific operating points. The operating points are selected to characterize the envelope and curvature of the flux-linkage surface. The derived MTPA locus can minimize the copper loss, and the proposed torque estimation can be executed in real time.

Secondly, the novel IPMSM drive model with all the losses considered is proposed, which includes the inverter loss, copper loss, core loss, and mechanical loss. In the proposed circuit, the resistance is used to present the power loss. The equivalent inverter-loss resistor is connected to the stator resistor in series, and the core-loss resistor is placed across the flux-linkage branch in parallel.

Thirdly, the loss minimization control based on the proposed model with constant parameters is developed. The analytical solution to the optimization problem with respect to the motor current contributing to the flux-linkage generation is formulated. The method to obtain the winding current references, which minimizes the total electrical loss, is discussed in full speed range. The influences of the stator-winding, inverter-loss and core-loss resistances on the current limit circle and voltage limit ellipse in different coordinates are analyzed. Compared to MTPA, LMC provides with more efficient energy utilization because all the electrical losses are considered.

Fourthly, the detailed process of the nonlinear parameters' characterization in steady-state is proposed. It can be realized without the information of the IPM machine known, such as the geometry and the permanent-magnet flux-linkage.

Fifthly, the back-fitting based torque estimation technique is proposed, which treats the core loss and mechanical loss as a whole. The separation of the mechanical loss and the core loss is not required.

Sixthly, based on the proposed algorithms the torque control system for IPMSM drives is designed. How to build the four-dimensional (4D) lookup tables (LUTs) for the nonlinear parameters and the three-dimensional (3D) LUTs for the optimal current references in full speed range are explained in detail. The precise current feedforward control reduces the feedback controller's burden and improves the dynamic response performance. The torque control accuracy of the proposed methodology is significantly enhanced compared to the conventional IPMSM modeling.

1.3 Thesis Outline

The thesis is organized as follows:

In Chapter 2, the optimal current control based on the conventional IPMSM model is studied. The MTPA control, MTPV/MTPF control, the current limit circle and the voltage constraint are introduced. The determination of the optimal current vector is explained with different motor designs. The strategies of generating the optimal current reference with variable parameters are reviewed.

In Chapter 3, a virtual flux-linkage model for the IPMSM with constant coefficients is proposed. It can generally be used to estimate the *d*- and *q*-axis flux-linkage profiles, so as to fit the MTPA locus and identify the torque without the information of the machine known. An optimization problem is formulated to find the appropriate factors for the proposed model based on the measured flux-linkage data at only nine specific operating points. No selection of the weight factors is required in the cost function. 2004 Prius IPMSM and one prototype motor are used to validate the accuracy of the torque estimation and MTPA control. This chapter has been published in [47].

In Chapter 4, the novel model for the IPMSM drives is proposed, which involves all the losses in the system. Based on the model, the relationship between the loss minimization control and the current in the flux-linkage branch is established. The analytical solution to the optimization problem is derived. For given torque and speed the optimal current can be directly obtained. The influence of the stator resistance, the equivalent inverter-loss and core-loss resistors on the voltage limit ellipse is analyzed. In order to find the optimal stator-winding current, the cost functions and the optimization constraints for the LMC, MTPV control, and FW control are formulated. The way to search for the critical points and the optimality validation are stated. The simulation results are provided.

In Chapter 5, the nonlinearities in the IPMSM drives are analyzed, which are the functions of the speed, the *d*- and *q*-axis current. The detailed process of the parameters' characterization is illustrated. The proposed algorithm is independent of the knowledge of the IPM machine. The methods of separating the core loss and mechanical loss are discussed. The back-fitting based torque estimation technique is proposed, which

eliminates the necessity of the manufacturing the dummy rotor. The voltage constraints based on different motor models are studied. Based on the 4D LUTs of the parameters the strategy of generating the optimal current command is described, which minimizes the total electrical loss in the system. The torque control scheme for IPMSM drives is designed, aiming at the accurate, fast dynamic response performance. The proposed algorithms are validated on an IPMSM prototype. The conventional IPMSM modeling has been published in [44]. The proposed model for IPMSM drives, the parameters' characterization method, the back-fitting based torque estimation technique, and the optimal current reference generation have been presented in [48].

In Chapter 6, the thesis is concluded and the possible future work is listed.

Chapter 2
Study of Optimal Current Control Based on the Conventional Interior Permanent Magnet Synchronous Machine Model

2.1 Introduction

The current vector control scheme plays an important role in the performance of IPMSM. Under certain operating condition selecting different current vector leads to different torque/power. Based on the conventional IPMSM model with constant parameters, different criteria of the selection of the current reference has been researched in literature [1], [11], [12], [49]–[52], such as the maximum torque-per-ampere control whose object is to minimize the copper loss, the maximum voltage/flux-per-ampere control whose goal is to minimize the electromotive force (EMF) voltage, and the flux-weakening control.

It is also necessary to study the current and voltage constraints, which are a circle and an ellipse in the *dq* coordinates, respectively, because they limit the possible combinations of the *d*- and *q*-axis current. According to different motor design, they determine the maximum output torque that the machine can generate and the maximum speed at which the motor can operate.

The real IPM motor has nonlinearities, such as the saturation and cross-coupling effects on the flux-linkage profiles. The researchers devote themselves to searching for the

optimal current reference with variable parameters of the conventional IPMSM model. In [47], [49], [53]–[55], MTPA tracking techniques are studied. The feasible optimal operating plane is analyzed with nonlinear characteristics of the IPMSM in [44], [56].

In this chapter, the basis of the current vector control with constant parameters is introduced, including MTPA, MTPV/MTPF, FW, current limit circle, and voltage limit ellipse. The strategies for obtaining the optimal current reference with nonlinearities are reviewed.

2.2 Conventional IPMSM Model

A three-phase machine in the stationary frame can be transformed into two rotating phases by using Clark and Park transformation. The *dq* equivalent circuit of IPM machine is shown in Fig. 2.1. The conventional flux-linkage and the voltage equations of IPMSM are expressed in (2.1) and (2.2), respectively.

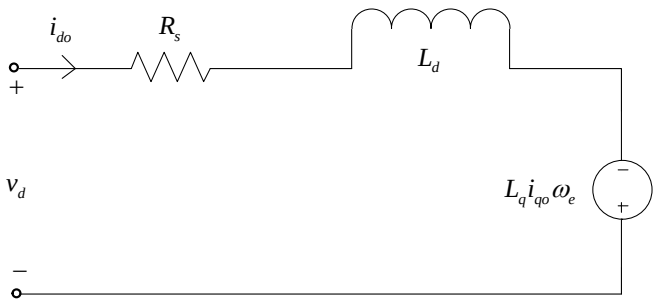

(a)

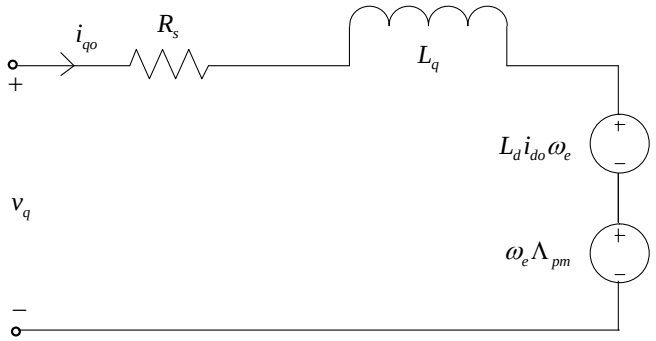

(b)

Fig. 2.1. Conventional IPMSM equivalent circuit. (a) *d*-axis. (b) *q*-axis.

$$\begin{bmatrix} \Lambda_d \\ \Lambda_q \end{bmatrix} = \begin{bmatrix} L_d & 0 \\ 0 & L_q \end{bmatrix} \begin{bmatrix} i_{do} \\ i_{qo} \end{bmatrix} + \begin{bmatrix} \Lambda_{pm} \\ 0 \end{bmatrix} \tag{2.1}$$

$$\begin{aligned} \begin{bmatrix} v_d \\ v_q \end{bmatrix} &= R_s \begin{bmatrix} i_{do} \\ i_{qo} \end{bmatrix} + \frac{d}{dt} \begin{bmatrix} \Lambda_d & 0 \\ 0 & \Lambda_q \end{bmatrix} + \omega_e \begin{bmatrix} 0 & -\Lambda_q \\ \Lambda_d & 0 \end{bmatrix} \\ &= R_s \begin{bmatrix} i_{do} \\ i_{qo} \end{bmatrix} + \frac{d}{dt} \begin{bmatrix} L_d & 0 \\ 0 & L_q \end{bmatrix} \begin{bmatrix} i_{do} \\ i_{qo} \end{bmatrix} + \begin{bmatrix} 0 & -\omega L_q \\ \omega L_d & 0 \end{bmatrix} \begin{bmatrix} i_{do} \\ i_{qo} \end{bmatrix} + \begin{bmatrix} 0 \\ \omega_e \Lambda_{pm} \end{bmatrix} \end{aligned} \tag{2.2}$$

where Λ_{pm} is the permanent-magnet flux-linkage, Λ_d is the *d*-axis flux-linkage, Λ_q is the *q*-axis flux-linkage, L_d is the *d*-axis inductance, L_q is the *q*-axis inductance, i_{do} is the *d*-axis winding current, i_{qo} is the *q*-axis winding current, v_d is the *d*-axis armature voltage, v_q is the *q*-axis armature voltage, ω_e is the electrical angular speed, and R_s is the stator winding resistance. In steady-state, the terms *d/dt* are zeros.

The electromagnetic torque of IPMSM consists of the magnet torque and reluctance torque, as described in (2.3).

$$\begin{aligned} T_e &= \frac{3}{2}P\left(\Lambda_d i_{qo} - \Lambda_q i_{do}\right) \\ &= \frac{3P}{2}\left[\Lambda_{pm} i_{qo} + (L_d - L_q) i_{do} i_{qo}\right] \\ &= \frac{3P}{2}\left[\Lambda_{pm} I_a \cos\beta + \frac{1}{2}(L_q - L_d) I_a^2 \sin 2\beta\right] \end{aligned} \tag{2.3}$$

where T_e is the electromagnetic torque, I_a is the amplitude of phase current, P is pole pair and β is the phase angle which is between the phase current vector and q-axis. The torque expression is derived from the energy transmission. The deduction is shown below.

$$P_{in} = \frac{3}{2}\left(v_d i_{do} + v_q i_{qo}\right)$$

$$= \frac{3}{2}\left[\left(R_s i_{do} - \omega_e \Lambda_q\right) i_{do} + \left(R_s i_{qo} + \omega_e \Lambda_d\right) i_{qo}\right]$$

$$= \frac{3}{2} R_s \left(i_{do}^2 + i_{qo}^2\right) + \frac{3}{2}\omega_e \left(\Lambda_d i_{qo} - \Lambda_q i_{do}\right)$$

$$= P_{Cu} + T_e \omega_m$$

$$\Rightarrow T_e = \frac{3}{2}P\left(\Lambda_d i_{qo} - \Lambda_q i_{do}\right)$$

where P_{in} is the electrical input power and P_{Cu} is the copper loss. ω_m is the mechanical angular speed, and it is equal to ω_e / P.

2.3 Optimal Current Control Schemes with Constant Parameters

2.3.1 Operating Constraints

The operating constraints of the IPMSM drives must be known before the optimal current reference could be found. They are the voltage and current limitation. The maximum voltage is constrained by the DC bus voltage. The capability of cooling for the copper loss and iron loss inside the machine defines the value of the maximum current. So the armature current I_a and the terminal voltage V_a are limited as shown in (2.4) and (2.5), respectively.

$$I_a = \sqrt{i_{do}^2 + i_{qo}^2} \le I_{am} \tag{2.4}$$

$$V_a = \sqrt{v_d^2 + v_q^2} \le V_{am} \tag{2.5}$$

where I_{am} is the maximum phase current and V_{am} is the maximum phase voltage.

The value of V_{am} is dependent upon the strategy of the pulse width modulation (PWM). If the winding is star-connected, the peak voltage on one phase is $2V_{dc}$ / 3. If SVPWM is applied and the pulse width modulation is undertaken in the linear range, in which the voltage reference is within the inscribed circle of the hexagon, $V_{am} = V_{dc} / \sqrt{3}$. If the overmodulation is involved, $V_{am} = 2V_{dc} / \pi$.

As shown in (2.2), the back EMF voltage accounts for the major proportion. The voltage drop across the stator resistor R_s is usually neglected while calculating the voltage constraint. (2.5) is reformulated as shown in (2.6).

$$\left(L_d i_{do} + \Lambda_{pm}\right)^2 + \left(L_q i_{qo}\right)^2 = \left(\frac{V_{am}}{\omega_e}\right)^2 \tag{2.6}$$

2.3.2 Maximum Torque-per-Ampere (MTPA) Control

For IPMSM's characteristic different current vectors can produce the same electromagnetic torque. It means that on the constant torque locus a current vector with the minimum amplitude can be found. In other words, among a set of current vectors with the same amplitude, a current vector with certain phase angle can be found to generate the maximum torque. This is the concept of MTPA control. Because for given torque the algorithm provides with the minimum phase current, it is also called the copper-loss minimization control.

The optimal phase angle can be found by making the derivative of the torque equation (2.3) with respect to phase angle be zero [51].

$$\frac{\partial T_e}{\partial \beta} = 0 \Rightarrow \beta = \sin^{-1}\left(\frac{-\Lambda_{pm} + \sqrt{\Lambda_{pm}^2 + 8(L_q - L_d)^2 I_a^2}}{4\left(L_q - L_d\right) I_a}\right) \tag{2.7}$$

The relationship between i_{do} and i_{qo} is expressed in (2.8) [54]. The current trajectory is plotted as a yellow curve in Fig. 2.2.

$$i_{do} = \frac{\Lambda_{pm}}{2\left(L_q - L_d\right)} - \sqrt{\frac{\Lambda_{pm}^2}{4\left(L_q - L_d\right)^2} + i_{qo}^2} \tag{2.8}$$

2.3.3 Maximum Torque-per-Voltage/Flux (MTPV/MTPF) Control

For IPMSM's characteristic a current vector with the minimum EMF voltage V_o ($=\omega_e\Lambda_m$) or flux-linkage Λ_m ($=\sqrt{\Lambda_d^2+\Lambda_q^2}$) on the constant torque locus can be found. This is the concept of the maximum-torque-per-flux-linkage/maximum-torque-per-voltage (MTPV/MTPF) control, shown as the green locus in Fig. 2.2.

Let $\Lambda_d = L_d i_{do} + \Lambda_{pm} = \Lambda_m \cos\delta$ and $\Lambda_q = L_q i_{qo} = \Lambda_m \sin\delta$. Use the flux-linkage Λ_m and δ to express the *d*- and *q*-axis current and substitute the expression into (2.3). Make the torque equation (2.3) with respect to δ be zero. Then the optimal current vector under MTPV/MTPF control strategy is obtained as shown in (2.9) and (2.10) [12].

$$i_{do} = -\frac{\Lambda_{pm} + \Delta\Lambda_d}{L_d} \tag{2.9}$$

$$i_{qo} = \frac{\sqrt{\Lambda_{mm}^2 - \Delta\Lambda_d^2}}{L_q} \tag{2.10}$$

where,

$$\Delta\Lambda_d = \frac{-L_d\Lambda_{pm} + \sqrt{\left(L_q\Lambda_{pm}\right)^2 + 8\left(L_q - L_d\right)^2\Lambda_{mm}^2}}{4\left(L_q - L_d\right)}.$$

MTPV is usually used to determine the maximum torque that can be achieved above base speed. It appears at the intersection where the constant torque locus and the voltage limit ellipse tangentially meet. Λ_{mm} in (2.10) refers to the maximum flux-linkage

amplitude. It can be calculated by using the maximum phase voltage V_{am} divided by the electrical angular speed.

2.3.4 Flux-Weakening (FW) Control

As the speed goes high, the EMF voltage increases. However, the line-to-line voltage is fixed at the DC bus voltage. In order to control the machine to spin at high speed, more *d*-axis current needs to be injected to contradict the permanent-magnet flux-linkage. The flux-linkage amplitude Λ_m decreases and higher speed can be reached. The current reference can be obtained by solving the voltage equation in (2.6). The relationship between the *d*- and *q*-axis current under FW control is described in (2.11) [49].

$$i_{do} = -\frac{\Lambda_{pm}}{L_d} \pm \frac{1}{L_d}\sqrt{\left(\frac{V_{am}}{\omega_e}\right)^2 - \left(L_q i_{qo}\right)^2} \tag{2.11}$$

2.3.5 Determination of the Optimal Current Reference

As expressed in (2.6), the voltage constraint is an ellipse in i_{dqo} plane. Its center is located at ($-\Lambda_{pm} / L_d$, 0). According to the motor design, the center of the voltage limit ellipse can be inside or outside of the current limit circle, as shown in Fig. 2.2(a) and Fig. 2.2(b), respectively.

In Fig. 2.2(a), $\Lambda_{pm} - L_d \cdot I_{am} < 0$, $T_0 < T_1 < T_2 < T_r$, and $\omega_b < \omega_1 < \omega_2$. MTPA is plotted in yellow, MTPV is drawn in green, the constant torque loci are in red, the current limit

circle is in black, and the voltage limit ellipses are in blue. Below base speed MTPA leads. At point A the constant torque curve tangentially meets the current limit circle. So T_r is the maximum torque that the IPM machine can produce. A voltage limit ellipse goes through point A. It determines the base speed ω_b. Above base speed, the flux-weakening control starts working. For example, at ω_1, the current vector at point B can generate the output torque T_2. If the electromagnetic torque T_1 is desired at ω_1, the current reference at point C should be applied. In order to achieve high efficiency at ω_1, when the command torque is smaller than T_0, the current vector along MTPA locus should be selected. As the speed increases, the voltage constraint shrinks. When the machine's speed is higher than ω_b and smaller than ω_2, the current limit circle enclosed between point A and point D indicates the maximum torque that the IPMSM can generate. As shown in the figure, MTPV appears at the intersection where the voltage limit ellipse and the constant torque locus tangentially meet, like point D. In other words, MTPV provides with the current reference that produces the maximum torque when the motor's speed is higher than ω_2. Because the center of the voltage constraint is located within the current limit circle, theoretically speaking, the motor's speed can be controlled to infinity at point M. Thus, when $\Lambda_{pm} - L_d \cdot I_{am} < 0$, from the control aspect, there is no upper limit of speed control. All in all, the bold lines, MTPA, current limit circle, MTPV, and the *d*-axis enclose the region where the optimal current vector can be selected.

In Fig. 2.2(b), $\Lambda_{pm} - L_d \cdot I_{am} > 0$, $T_1 < T_2 < T_r$, and $\omega_b < \omega_1 < \omega_2$. MTPA is plotted in yellow, the constant torque loci are drawn in red, the current limit circle is in black, and the voltage limit ellipses are in blue. Below base speed the MTPA control still leads. The

determination of the maximum torque T_r and the base speed ω_b is same as illustrated in Fig. 2.2(a). However, above base speed only the current limit circle defines the maximum output torque. The FW control works at the operating points like point B and C at ω_1. As the speed increases, the voltage limit ellipse continues shrinking until the speed reaches ω_2, where the current limit circle and the voltage constraint tangentially meet at point D. The current reference on ellipses, which are smaller than the one at ω_2, cannot be generated because its amplitude cannot be bigger than I_{am}. Thus, when $\Lambda_{pm} - L_d \cdot I_{am} > 0$, there is the boundary that limits the machine's maximum speed. All in all, the bold lines, MTPA, current limit circle, and the *d*-axis enclose the region where the optimal current vector can be selected.

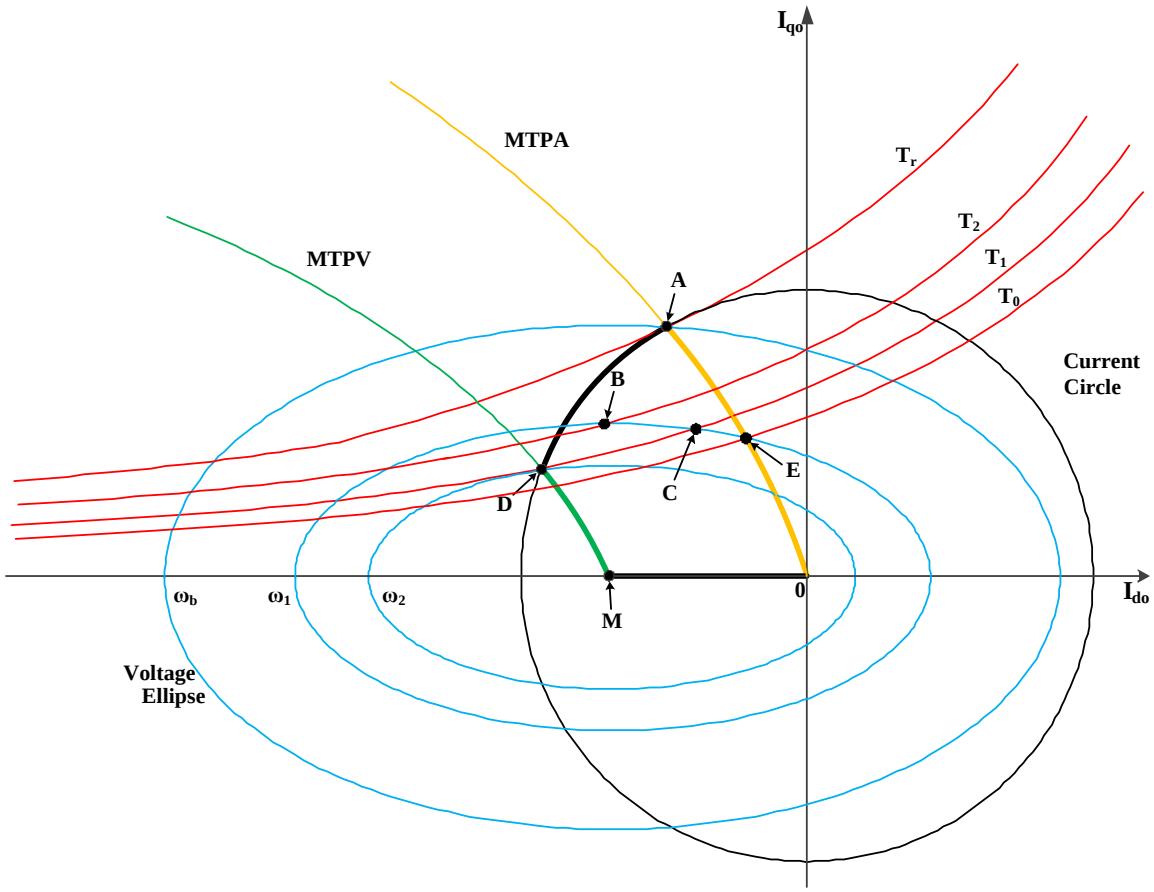
I_{q0}
MTPA
T_r
T_2
T_1
T_0
MTPV
A
B
C
D
E
Current Circle
ω_b
ω_1
ω_2
M
0
I_{do}
Voltage Ellipse

(a)

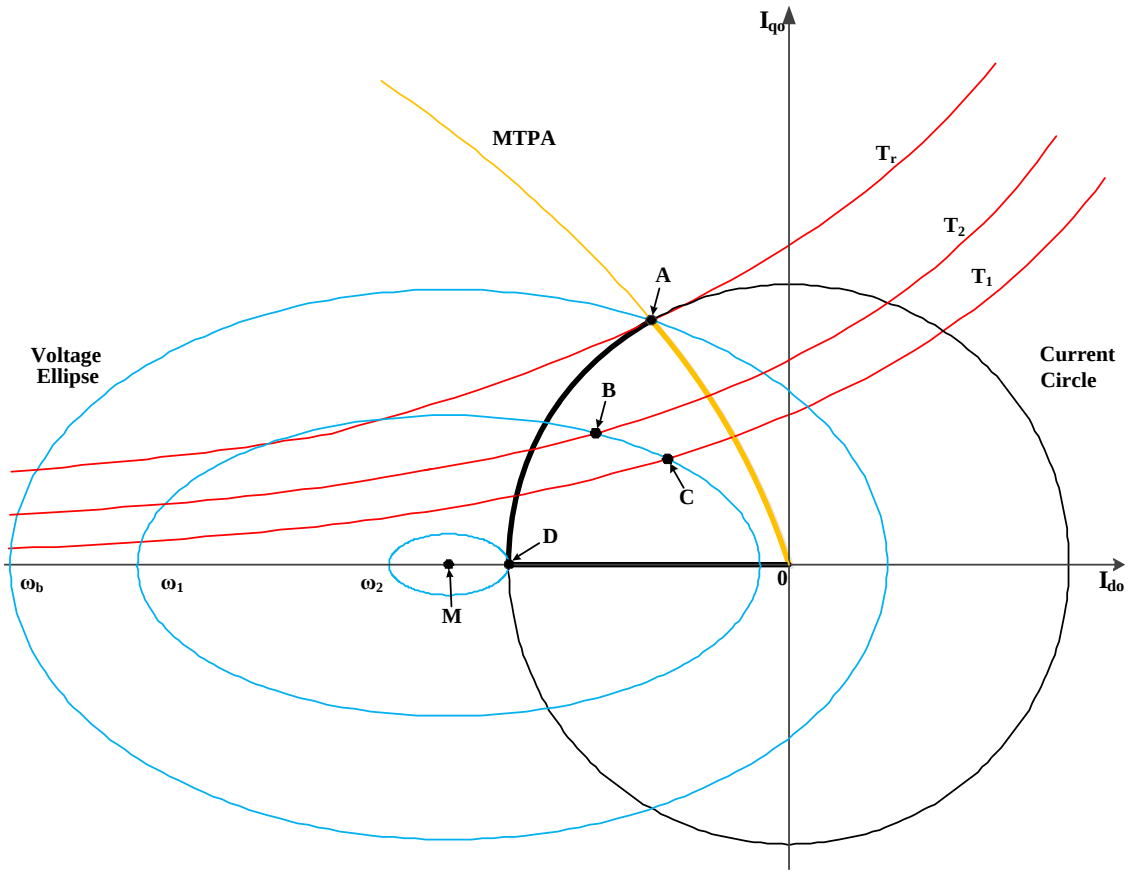

(b)

Fig. 2.2. Selection of the optimal current vector. (a) $\Lambda_{pm} - L_d \cdot I_{am} < 0$. (b) $\Lambda_{pm} - L_d \cdot I_{am} > 0$.

2.4 Optimal Current Control Schemes with Variable Parameters

The optimal current reference based on the conventional IPMSM can be obtained with constant parameters by using the strategies in section 2.3. However, the real machine's

characteristics are nonlinear, such as the *d*- and *q*-axis flux-linkage profiles shown in Fig. 2.3, which are FEA results of 2004 Prius IPMSM model in ANSYS.

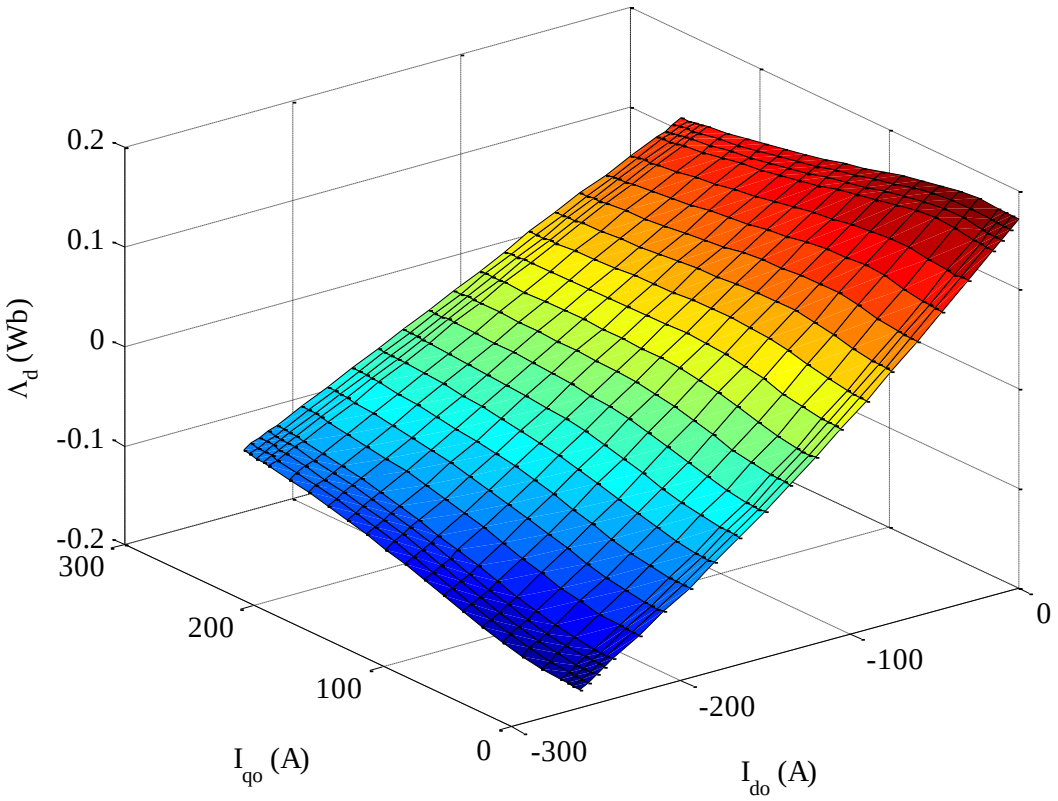

(a)

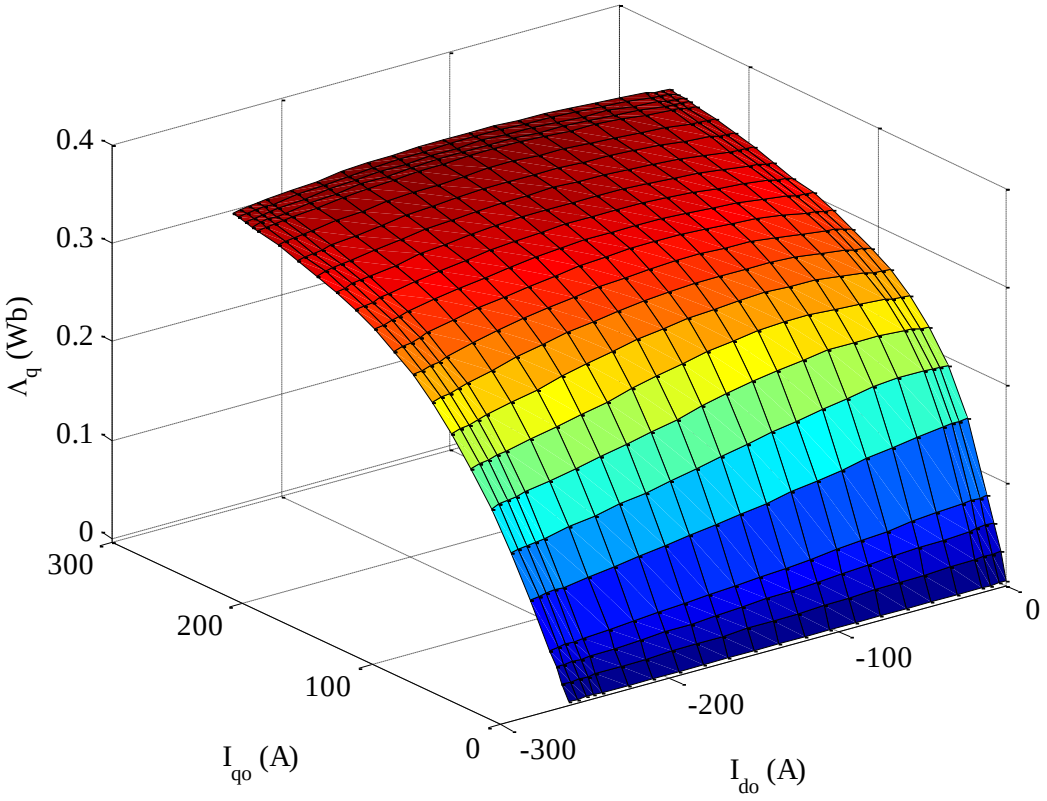

(b)

Fig. 2.3. Flux-linkage profiles of 2004 Prius IPMSM [34]. (a) *d*-axis flux-linkage. (b) *q*-axis flux-linkage.

In order to adjust the optimal current control to the nonlinearities, different schemes have been developed. In [47], a new model is proposed to capture the saturation and cross-coupling effects on the flux-linkage profiles. The MTPA condition is deducted correspondingly.

In [53], a mathematical model is proposed for MTPA trajectory estimation in the stator flux linkage synchronous frame. The magnetic saturation and cross-magnetization effects are taken into account. The factors in the model can be determined by some simple experiments.

In [49], the local optimization is proposed, aiming at a rough approximation of the real behavior. However, this algorithm can only be applied to the machines with small saturation because it still uses the constant values for the machine's parameters.

In [54], an adaptive self-tuning controller is presented. The MTPA control works with the adaptive parameter estimator. The algorithm loses some accuracy because the *d*-axis inductance is assumed to be constant.

In [55], the operating point on MTPA locus is tracked by current injection. A component of the input power with the signal injection is proportional to the differentiation of the torque with respect to the phase angle. Once the component is extracted and controlled as null, the MTPA operation can be guaranteed. The method is independent of motor's parameters.

In [56], the LUTs of the permanent-magnet flux-linkage, the *d*- and *q*-axis inductances are built to depict the nonlinearities of the IPM motor. The distortion of the MTPA, MTPV, and the voltage limit ellipse is analyzed, as shown in Fig. 2.4. A new optimal operating plane based on the LUTs is generated.

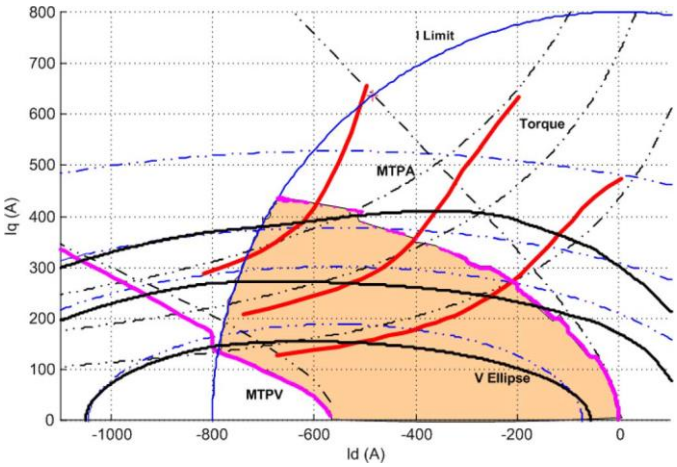

Fig. 2.4. Comparison of the optimal operating plane with or without motor parameter changes [56].

In [44], the extended MTPA control is proposed in the entire torque-speed range. Instead of figuring out the exact values for L_d, L_q, and Λ_{pm}, the method searches for the current reference that minimizes the copper loss within the current and voltage constraints based on the measured *d*- and *q*-axis flux-linkage profiles.

2.5 Summary

This chapter introduces the fundamental knowledge of the optimal current control of IPMSM. The conventional IPM model is described. MTPA, MTPV, and FW control strategies with constant parameters are presented. The optimization constraints are studied. The determination of the optimum current reference in the operating plane based

on different motor design is researched. The strategies of generating the optimal current reference with variable parameters are reviewed.

Chapter 3
Maximum Torque-Per-Ampere Fitting and Torque Estimation Technique Based on a New Flux-Linkage Model for Interior Permanent Magnet Synchronous Machines

3.1 Introduction

In [1], [12], [57] MTPA is well explained by using the conventional motor model. In [57], a linear torque control strategy based on MTPA is proposed. A second-order approximation is applied for high-order equation by assuming that all the parameters of the machine, such as the *d*-axis and *q*-axis inductances, are constants. However, the conventional IPM motor model with constant parameters is not appropriate for the real machines since the *d*-axis and *q*-axis flux-linkage profiles are nonlinear as shown in Fig. 2.3. In practical applications, the development of the MTPA and torque estimation should include the self- and cross-coupling effects on the inductances [30], [58], [59], which are obtained from either the finite element analysis (FEA) or experimental results [34], [43], [53], [56].

In [53], a mathematical model is proposed for MTPA control considering the nonlinearity of the inductances. The parameter estimation is obtained from the measurement of MTPA locus.

In [34], the FEA simulation results of the *d*-axis and *q*-axis flux-linkages are used to minimize the copper loss. The method is accurate enough to find the optimal current reference and identify the torque. Nevertheless, it cannot work if the machine's geometry and other information are unavailable for FEA simulation.

In [56], the look-up-tables (LUTs) are built to depict the behavior of the machine. The *d*- and *q*-axis inductances and the permanent-magnet flux-linkage are obtained by using the measured data to fit the flux profile. Although experiments can be done to quickly search for the optimal current reference on different current circles, the torque sensor might not be available on the test bench.

In [43], a model with respect to the current is proposed to identify the inductances by considering the saturation and cross-coupling influences. However, the model is too complicated to implement online.

In [49], the local linearization technique is proposed to fit the MTPA and torque. The *d*- and *q*-axis inductances, permanent-magnet flux-linkage and pole pair are calculated by using the data at the rated and demagnetization operating points. However, this algorithm can only be applied to the machines with small saturation.

The self-tuning control strategy based on the online estimation of the motor's parameters are studied in [54], [60], [61]; but, the algorithm involves the selection of the gains in the adaptation laws.

In [62], the difference between the reference power and output power is used to identify the inductances. However, the simulation results show the estimation errors may make MTPA fail.

The signal injection method is introduced in [55], [63]–[65]. A fuzzy-logic-based MTPA speed control strategy is illustrated in [66]. These types of control schemes are independent of the parameters. Nevertheless, it generates torque ripples and the searching convergence can be time-consuming.

In this chapter, a mathematical flux-linkage model is proposed to fit the nonlinear flux-linkage profiles of IPMSM. Both saturation and cross-coupling impacts are considered. With twelve constant coefficients, the model can easily capture the behavior of the machine by using the measured flux-linkage information at only nine scattered operating points. The MTPA and electromagnetic torque estimation can be fairly achieved by the implementation of some simple experiments instead of FEA simulation. The merit of the proposed algorithm lies in the feasibility without the machine's design information and the use of torque transducer. The simplicity of the proposed model enables the real-time implementation of the torque identification. The simulation and experimental validation have been done for the proposed algorithm.

3.2 MTPA Fitting and Torque Estimation Based on the Conventional IPMSM Model with Constant Parameters

Due to the nonlinearity of the flux-linkage profiles, the MTPA control for the practical use of IPMSM can be expressed in (3.1) [34].

Minimize

$$i_{do}^2 + i_{qo}^2 \tag{3.1}$$

Subject to

$$T_e - \frac{3}{2} P\left(\Lambda_d i_{qo} - \Lambda_q i_{do}\right) = 0;$$

$$i_{do}^2 + i_{qo}^2 \le I_{am}^2.$$

In simulation, FEA flux-linkage profiles of an IPM motor are imported and MATLAB optimization toolbox is adopted to solve the problem. The resultant MTPA locus is shown as a solid black curve in Fig. 3.1.

In order to obtain the optimal current reference in (3.1), the flux-linkage data throughout the operating map is needed. However, this method relies on the parameters of the machine. The knowledge of machines, such as the geometry and material, might be unavailable. On the other hand, a torque sensor might not be available for the experiments. In fact, a simpler way can be achievable by using the known IPMSM model. A set of constant parameters needs to be found so that the proposed model with the constants has the key traits as the real machine does. If the appropriate approximation is obtained, good MTPA control and fair torque estimation still can be realized without the design information of IPMSM known.

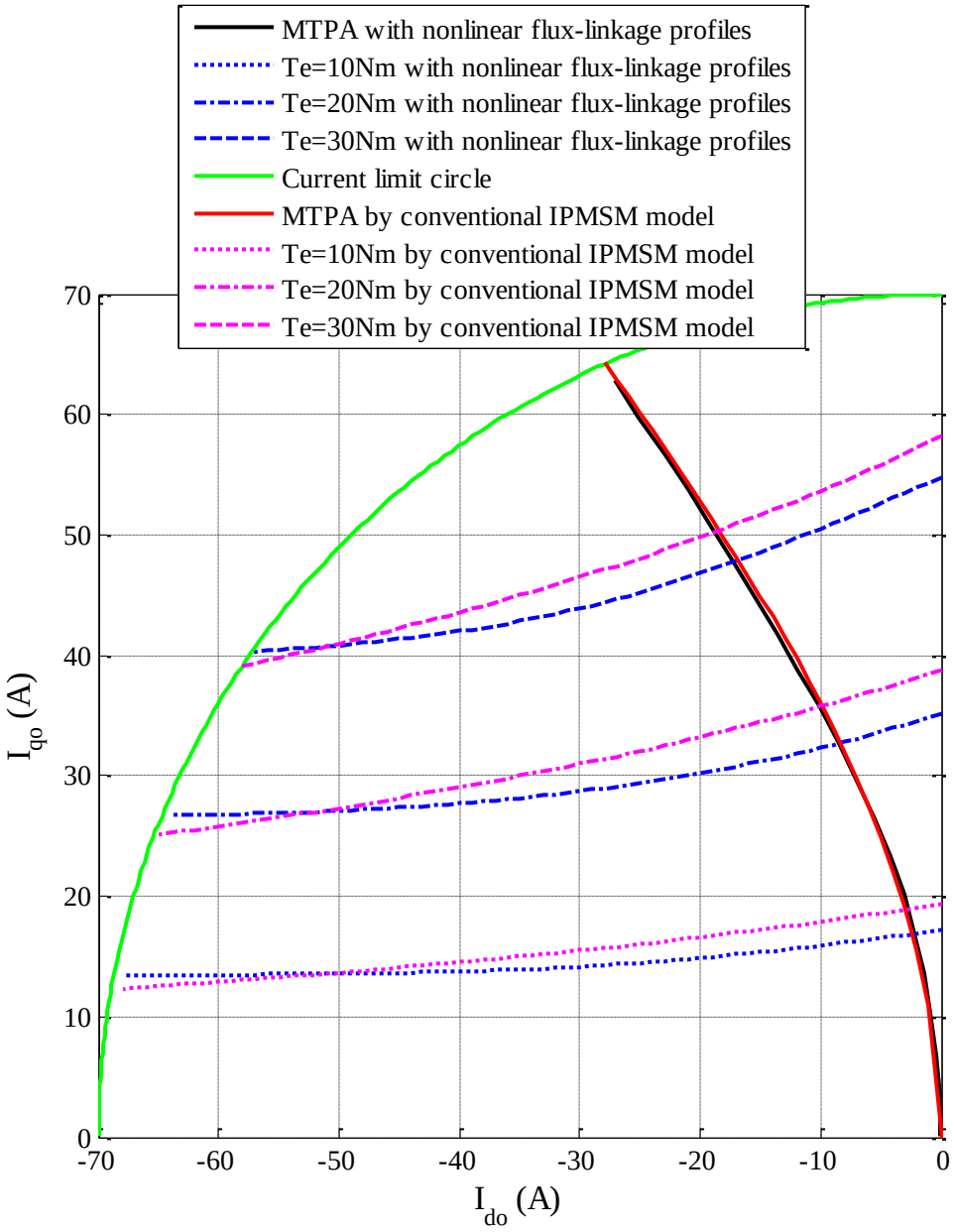

Fig. 3.1. Characteristic comparison between the conventional motor model and FEA data.

The optimization problem shown in (3.2) is established for such purpose by using the conventional IPM motor model.

Minimize

$$\left(\Lambda_{dr}-\Lambda_{drc}\right)^2+\left(\Lambda_{qr}-\Lambda_{qrc}\right)^2+\left(\Lambda_{dh}-\Lambda_{dhc}\right)^2+\left(\Lambda_{qh}-\Lambda_{qhc}\right)^2 \tag{3.2}$$

Subject to

$$\Lambda_{pm} i_{dr}+\left(L_q-L_d\right)\left(i_{qr}^2-i_{dr}^2\right)=0$$

where i_{dr}, i_{qr}, Λ_{dr}, Λ_{qr}, $\Lambda_{drc,}$ and Λ_{qrc} are the *d*-axis current, *q*-axis current, real *d*-axis flux-linkage and *q*-axis flux-linkage, and the calculated *d*- and *q*-axis flux-linkages at the rated operating point where MTPA control in (3.1) and the current limit circle meet, based on (2.1) with the fitted inductances; Λ_{dh}, Λ_{qh}, Λ_{dhc}, and Λ_{qhc} are the real *d*-axis flux-linkage and *q*-axis flux-linkage, and the calculated *d*- and *q*-axis flux-linkages based on the conventional motor model at the intersection of MTPA and the current circle whose amplitude is half of the current constraint.

In this method, only the data of two operating points are involved to solve (3.2). The goal is to minimize the total squared error between the actual and fitted flux-linkage. The optimization constraint is that the fitted MTPA locus must go through the rated operating point. A set of constant *d*-axis inductance, *q*-axis inductance, and the permanent-magnet flux-linkage can be found for this purpose. It should be noted that the MTPA locus in (2.8) actually is a hyperbola with the asymptote slope of -1 as shown in (3.3). If the curve of MTPA in (3.1) is distorted towards the direct axis by the nonlinearity of the machine, the fitted MTPA locus cannot go through the rated operating point because of its fixed slope.

$$\frac{\left[i_{do}-\frac{\Lambda_{pm}}{2\left(L_q-L_d\right)}\right]^2}{\frac{\Lambda_{pm}^2}{4\left(L_q-L_d\right)^2}}-\frac{i_{qo}^2}{\frac{\Lambda_{pm}^2}{4\left(L_q-L_d\right)^2}}=1 \tag{3.3}$$

The MTPA and torque identification generated by the conventional IPM motor model with the fitted constant parameters are plotted in Fig. 3.1. MTPA based on (3.1) and constant torque loci based on FEA data are drawn in the same figure. Even though the MTPA loci fit each other well, the mismatch between the estimated torque and the one based on the FEA data is still obvious.

Due to the saturation and cross-coupling effects of IPMSM, the conventional motor model with constant parameters is unable to adapt itself to the real machine, as shown in Fig. 3.2. It could work only if the parameters in (2.1) are considered as the functions of *d*- and *q*-axis current.

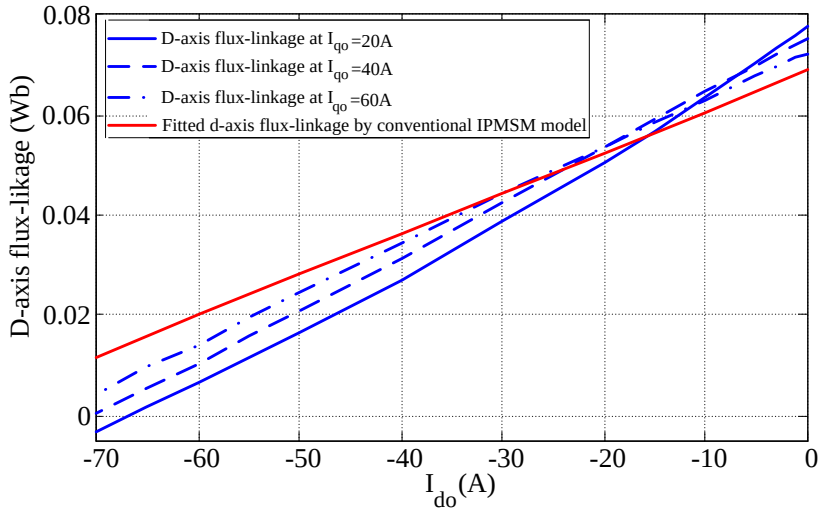

(a)

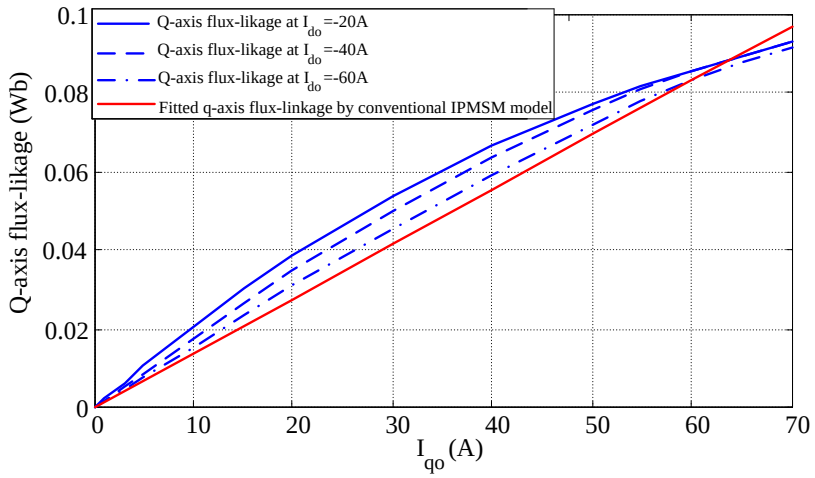

(b)

Fig. 3.2. Flux-linkage fittings with the conventional motor model. (a) *d*-axis flux-linkage. (b) *q*-axis flux-linkage.

3.3 MTPA Fitting and Torque Estimation Based on a Fitting Flux-Linkage Model with Constant Parameters

3.3.1 Proposed Fitting Model for Flux-Linkage

Considering the saturation and cross-coupling effects on the flux-linkage profiles of an IPM motor, a fitting model for the flux-linkage in a generalized form is proposed as shown in (3.4). Because the *d*-axis flux-linkage is the even function of the *q*-axis current and Λ_q is the odd function of i_{qo}, the absolute value is used and the sign of *q*-axis current indicates in which quadrant the IPMSM operates, hence equation (3.4) work both in the motoring mode and generating mode.

$$\begin{cases} \Lambda_d = k_d + l_d i_{do} + m_d \left| i_{qo} \right| + \mathbf{i}_{dqo}^{'} \mathbf{H}_d \mathbf{i}_{dqo} \\ \Lambda_q = \operatorname{sgn}\left(i_{qo} \right) \cdot \left(k_q + l_q \left| i_{qo} \right| + m_q i_{do} + \mathbf{i}_{dqo}^{'} \mathbf{H}_q \mathbf{i}_{dqo} \right) \end{cases} \tag{3.4}$$

where, $\mathbf{i}_{dqo} = \begin{bmatrix} i_{do} \\ i_{qo} \end{bmatrix}$, $\mathbf{H}_d = \begin{bmatrix} h_{d11} & h_{d12} \\ h_{d21} & h_{d22} \end{bmatrix}$, $\mathbf{H}_q = \begin{bmatrix} h_{q11} & h_{q12} \\ h_{q21} & h_{q22} \end{bmatrix}$. k_d, k_q, l_d, l_q, m_d, m_q, h_{d11}, h_{d12}, h_{d21}, h_{d22}, h_{q11}, h_{q12}, h_{q21}, and h_{q22} are constant coefficients.

Compared to the conventional flux-linkage model in (2.1), the proposed model in (3.4) has some additional components. k_d refers to the permanent-magnet flux-linkage. k_q is adopted to generalize the quadrant form of the model and compensate the offset for Λ_q. With a fitting-based technique to minimize the error between the real and estimated flux-linkage, k_q might not be zero. l_d and l_q correspond to the *d*- and *q*-axis self inductances.

The introduction of the coefficients m_d, m_q, h_{d11}, h_{d12}, h_{d21}, h_{d22}, h_{q11}, h_{q12}, h_{q21} and h_{q22} help further represent the saturation and cross-coupling effects. It should be noted that the proposed model is obtained based on fitting technique and only the approximated independent expression of the flux-linkage profile. The factors in (3.4) are not directly related to physical parameters of the studied motor so the proposed model cannot be used for computing inductance maps.

3.3.2 Determination of the Coefficients

Because the *q*-axis flux-linkage, the electromagnetic torque, and MTPA are symmetric with respect to the *d*-axis, the coefficients in the proposed model can be determined with the necessary information only in the motoring mode. The characteristics of the machine can be obtained by flipping over along the *d*-axis from quadrant II into quadrant III. As shown in Fig. 3.3, the flux-linkage data at points from '1' to '9' are selected, which are marked as '+'. Point '1' is located on the current circle with the amplitude of 1/3 of I_{am}. Point '2' is on the direct axis. Points '4' and '6' are on the current circle whose radius is 2/3 of the maximum phase current. Points '3', '5', '7', '8' and '9' are on the current constraint.

The determination of the coordinates is processed below:

1) Plot three current circles with amplitudes of 1/3, 2/3 and 1 of the maximum phase current, respectively.

2) Plot a straight line ‘a’ across the origin and make the angle between the line and the direct axis be 45°. It intersects three current circles at points ‘1’, ‘F’ and ‘3’.

3) At point ‘F’ draw two lines, ‘d’ and ‘e’, which are perpendicular to the d- and q-axis, respectively. They meet the d-axis and the current limit at points ‘2’, ‘8’ and ‘9’.

4) At point ‘1’ draw two lines, ‘c’ and ‘b’, which are parallel with the d- and q-axis, respectively. They meet the bigger two circles at points ‘4’, ‘5’, ‘6’ and ‘7’.

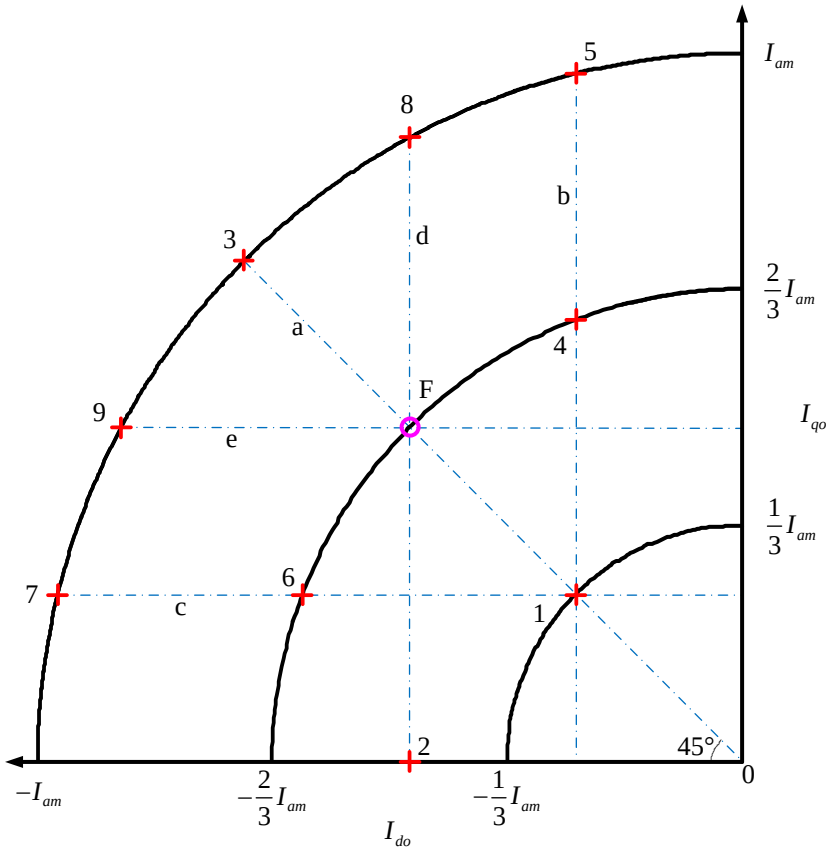

Fig. 3.3. Selection of operating points for coefficients’ fitting.

The limited selections are responsible for the flux-linkage mapping. Points ‘1’, ‘2’, ‘3’, ‘4’, ‘5’, ‘7’, ‘8’ and ‘9’ help determine the envelopes of the flux-linkage profiles. Point

'6' is picked to post more weight in the flux-weakening region. Point '4' and '6' are also beneficial to decide the curvature in the middle of the flux-linkage surface. The amount of the selected operating points is decided by trial and error. Nine points are the minimum quantity that can achieve good fitting.

With the help of the flux-linkage data at scattered points in Fig. 3.3, the coefficients in (3.4) can be determined by solving the optimization problem as shown in (3.5).

Minimize

$$\sum_{i=1}^{9}\left(\Lambda_{dfi}-\Lambda_{dmi}\right)^2+\sum_{i=1}^{9}\left(\Lambda_{qfi}-\Lambda_{qmi}\right)^2 \tag{3.5}$$

where Λ_{dfi} and Λ_{qfi} are the fitted *d*-axis and *q*-axis flux-linkages in the proposed model at nine operating points; Λ_{dmi} and Λ_{qmi} are the measured flux-linkages accordingly. 'fmincon' in Matlab optimization toolbox is adopted to solve the problem.

3.3.3 Derivation of Torque Equation and MTPA Condition Based on the Proposed Model

The corresponding torque expression can be obtained by substituting the *d*- and *q*-axis flux-linkages in (3.4) into the torque equation in (2.3).

$$T_e=\frac{3}{2}P\cdot\mathrm{sgn}\left(i_{qo}\right)\cdot\begin{bmatrix}-q_1 i_{do}^3+\left(d_1-q_2\right)i_{do}^2\left|i_{qo}\right|-m_q i_{do}^2\\ -k_q i_{do}+\left(l_d-l_q\right)i_{do}\left|i_{qo}\right|+\left(d_2-q_3\right)i_{do}i_{qo}^2\\ +k_d\left|i_{qo}\right|+m_d i_{qo}^2+d_3\left|i_{qo}^3\right|\end{bmatrix} \tag{3.6}$$

where, $d_1 = h_{d11} + h_{d12}$, $d_2 = h_{d21}$, $d_3 = h_{d22}$, $q_1 = h_{q11} + h_{q12}$, $q_2 = h_{q21}$ and $q_3 = h_{q22}$. This torque expression is valid only for average torque calculation.

Substituting $i_d = -I_a \cdot sin\beta$ and $i_q = I_a \cdot cos\beta$ into (3.6), make the derivative of the resultant expression of (3.6) with respect to the excitation angle β be zero. Then substituting the *d*- and *q*-axis currents back into MTPA condition, the copper-loss minimization control can be obtained as shown in (3.7). It should be noted that although there are fourteen coefficients in the proposed flux-linkage model in (3.4), for MTPA control and torque estimation only the sum of h_{d11}, h_{d12}, and h_{q11}, h_{q12} matters in (3.6) and (3.7). In other words, there are twelve constant factors to be determined in section 3.3.2 instead of fourteen, which are k_d, k_q, l_d, l_q, m_d, m_q, d_1, d_2, d_3, q_1, q_2, and q_3.

$$\begin{aligned}&(d_1-q_2)i_{do}^3+\left[3q_1\left|i_{qo}\right|-2(q_3-d_2)\left|i_{qo}\right|+l_d-l_q\right]i_{do}^2\\&+\left[2(q_2-d_1)i_{qo}^2+3d_3i_{qo}^2+2(m_d+m_q)\left|i_{qo}\right|+k_d\right]i_{do}\\&+(q_3-d_2)\left|i_{qo}^3\right|+(l_q-l_d)i_{qo}^2+k_q\left|i_{qo}\right|=0\end{aligned} \tag{3.7}$$

The solutions to this cubic equation [67] for the optimal *d*-axis current reference are derived in (3.8).

$$
\begin{aligned}
i_{do1} &= -\frac{1}{3a}\left(b + S + \frac{Z}{S}\right) \\
i_{do2} &= -\frac{1}{3a}\left[b + \frac{-1+i\sqrt{3}}{2}S + \frac{Z}{\frac{-1+i\sqrt{3}}{2}S}\right] \\
i_{do3} &= -\frac{1}{3a}\left[b + \frac{-1-i\sqrt{3}}{2}S + \frac{Z}{\frac{-1-i\sqrt{3}}{2}S}\right]
\end{aligned}
\tag{3.8}
$$

where,

$$S = \sqrt[3]{\frac{O + \sqrt{O^2 - 4Z^3}}{2}};$$

$$Z = b^2 - 3ac;$$

$$O = 2b^3 - 9abc + 27a^2 d;$$

$$a = d_1 - q_2;$$

$$b = 3q_1\left|i_{qo}\right| - 2\left(q_3 - d_2\right)\left|i_{qo}\right| + l_d - l_q;$$

$$c = 2\left(q_2 - d_1\right)i_{qo}^2 + 3d_3 i_{qo}^2 + 2\left(m_d + m_q\right)\left|i_{qo}\right| + k_d;$$

$$d = \left(q_3 - d_2\right)\left|i_{qo}^3\right| + \left(l_q - l_d\right)i_{qo}^2 + k_q\left|i_{qo}\right|.$$

Apparently, different combinations of the coefficients lead to different roots. Even with the same factors, three roots results in three different loci. It is necessary to distinguish which one is the desired current reference. A simple way is to substitute i_{qo} = 0A into i_{do1},

i_{do2}, and i_{do3} listed in (3.8). In this case, the *d*-axis current reference is supposed to be zero in accordance with the principle of MTPA control. For example, substitute a set of fitted factors into (3.8) when *q*-axis current is zero. Zero ampere is obtained in the second root. Then, the optimal *d*-axis current can always be derived by substituting different *q*-axis currents into the root i_{do2} according to the applied constants.

3.3.4 Implementation of MTPA Fitting and Torque Estimation Based on the Proposed Model

The application of the proposed algorithm should be followed in several steps:

1) Monitor the *d*- and *q*-axis voltage references at nine specific operating points under a certain speed. Higher speed is preferred because the stator resistor is less influential on results. But the speed needs to be lower than the base speed since some of the points are on the current limit circle.

2) Calculate the flux-linkages for each spot by using the equations (3.9) and (3.10).

$$\Lambda_d = \frac{v_q - R_s i_{qo}}{\omega_e} \tag{3.9}$$

$$\Lambda_q = \frac{R_s i_{do} - v_d}{\omega_e} \tag{3.10}$$

3) Substitute the measured data into (3.5) in order to find the appropriate coefficients. The curve-fitting tool can be used to set the initial values of the twelve coefficients in the optimization problem.

4) Substitute the fitted factors into (3.8) with zero *q*-axis current. Figure out which root can result in zero *d*-axis current and use that root to obtain MTPA locus.

5) Equation (3.6) can be applied for real-time torque estimation. If the speed control loop is adopted in the control system, (3.8) can be directly used to determine the optimal current reference. In order to reduce the online computational complexity, a second-order polynomial can be used to depict MTPA instead of using (3.8), after the relationship between *d*- and *q*-axis currents based on the experimental data is built.

3.4 Simulation and Experimental Results

In order to validate the proposed algorithms in a comprehensive manner, two electric machines, including one 2004 Prius IPMSM and one motor prototype, are used.

Table 3.1. Coefficient fitting results for PRIUS 2004 IPMSM.

Coefficient	Value	Unit
k_d	0.1725	Wb
k_q	0.0302	Wb
l_d	0.0015	H
l_q	0.0034	H
m_d	-6.91×10^{-5}	H
m_q	1.02×10^{-4}	H
d_1	2.86×10^{-7}	H/A
d_2	-2.48×10^{-6}	H/A
d_3	-5.07×10^{-7}	H/A
q_1	-1.83×10^{-7}	H/A
q_2	2.82×10^{-7}	H/A
q_3	-8.78×10^{-6}	H/A

The fitting result of the coefficients for 2004 Prius IPMSM is listed in Table 3.1. The estimated and the actual flux-linkage profiles are shown in Fig. 3.4. The torque estimation error map is plotted in Fig. 3.5. The algorithms are proposed for IPMSM commissioning without the torque sensor in the system. Thus, in this section, the torque estimation error is defined as the full-scale error, $\frac{T_{estimate}-T_{measured}}{T_{\max}}\times100\%$. These results show that the torque estimation is significantly improved by the proposed algorithm compared to the conventional torque estimation method as shown in Fig. 3.6. The values of the *d*- and *q*-

axis inductances and permanent-magnet flux-linkage in Table 3.1 are used in the conventional method. Due to the mismatch of the flux-linkage, the conventional torque estimation method leads up to 75% estimation error; however, the largest torque estimation error based on the proposed method is only 5%.

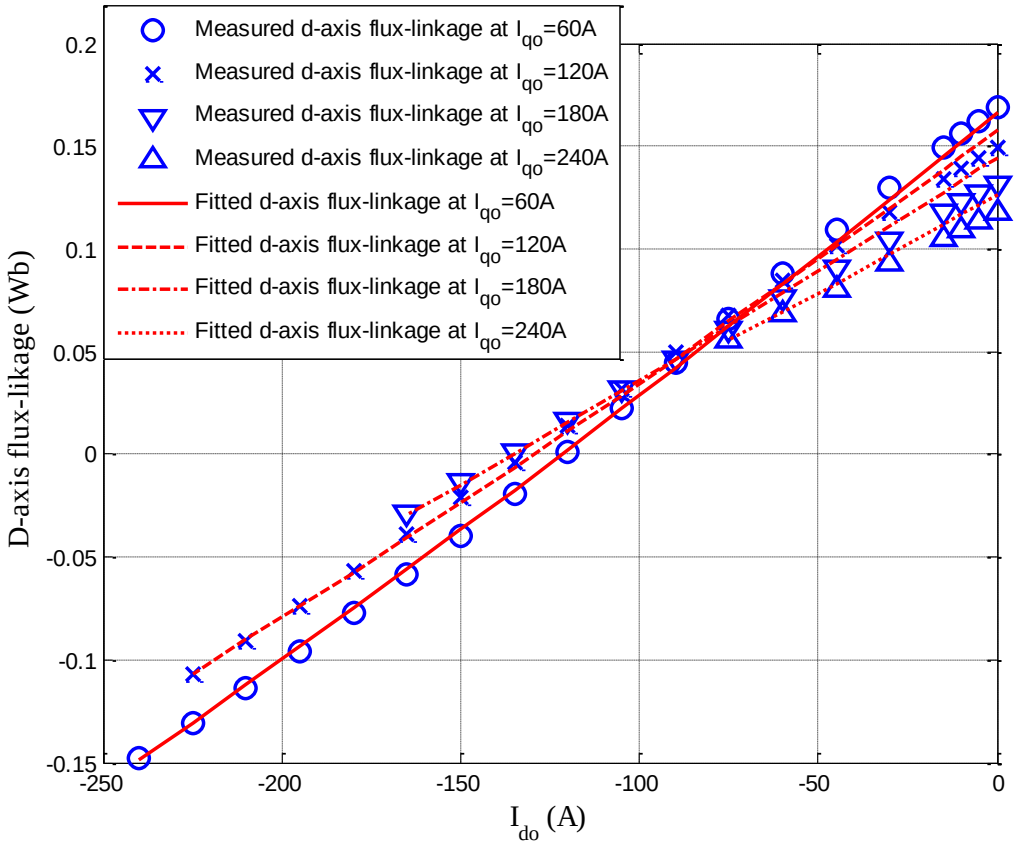

(a)

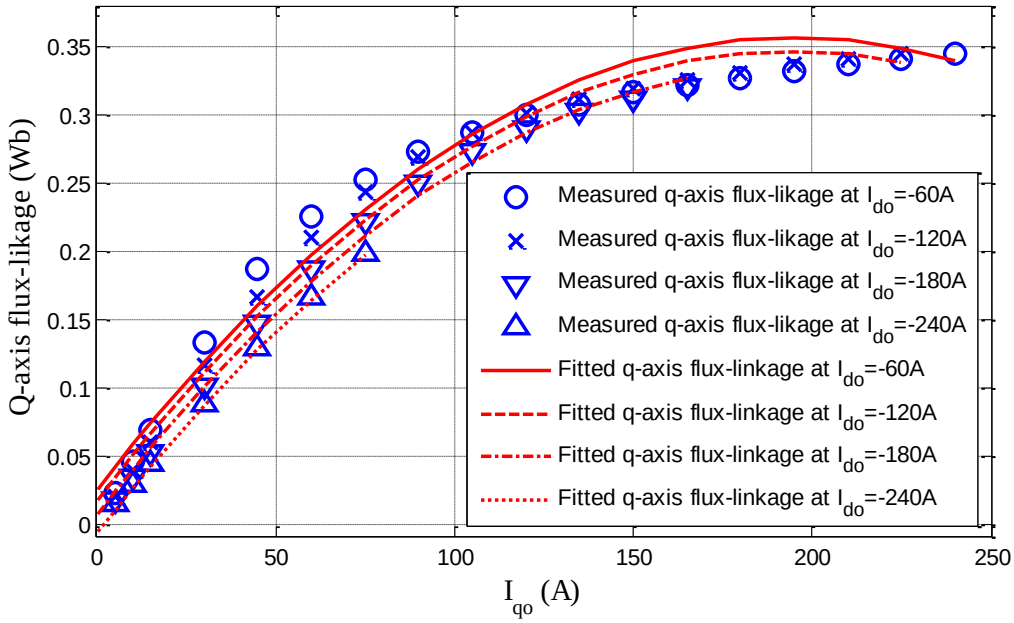

(b)

Fig. 3.4. Flux-linkage comparison between the proposed model and Prius 2004 IPM motor: (a) Λ_d. (b) Λ_q.

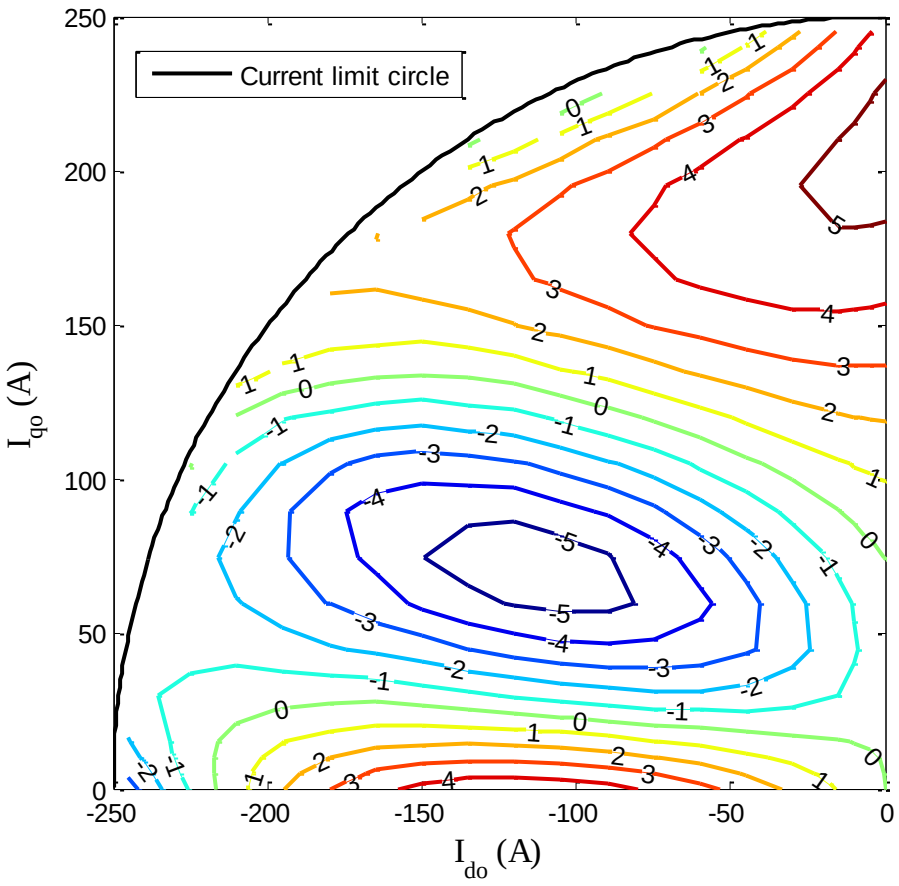

Fig. 3.5. Torque estimation error (%) of Prius 2004 IPMSM based on the proposed model.

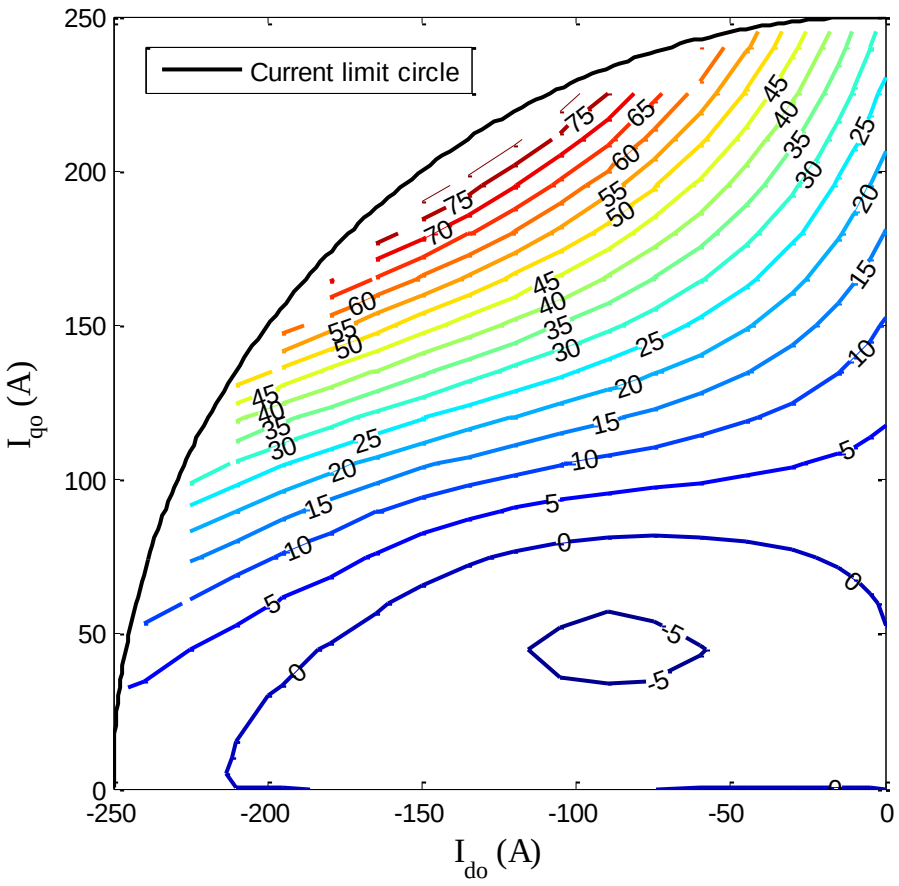

Fig. 3.6. Torque estimation error (%) of Prius 2004 IPMSM based on the conventional model.

The algorithm also has been adopted to characterize a real IPM motor. The experiment kits are shown in Fig. 3.7. An NEMA induction machine is used as the dyno motor. YASKAWA A1000 is applied to drive the induction machine. The IPM motor under test has ten poles. Its maximum output power is 12kW and the peak phase current is 70A. The stator resistance is 0.1Ω. Infineon HybridPACK^{TM}2 is used to drive the IPMSM. The controller of IPMSM drive is designed based on TI DSP 28335. A resolver is applied as

the source of the position feedback. An A/D conversion chip with 12-bit resolution is connected to the outputs of the current sensors. In order to validate the torque estimation and MTPA fitting a torque transducer is installed between the dyno machine and the IPM motor, whose full-scale measurement error is ±0.5%.

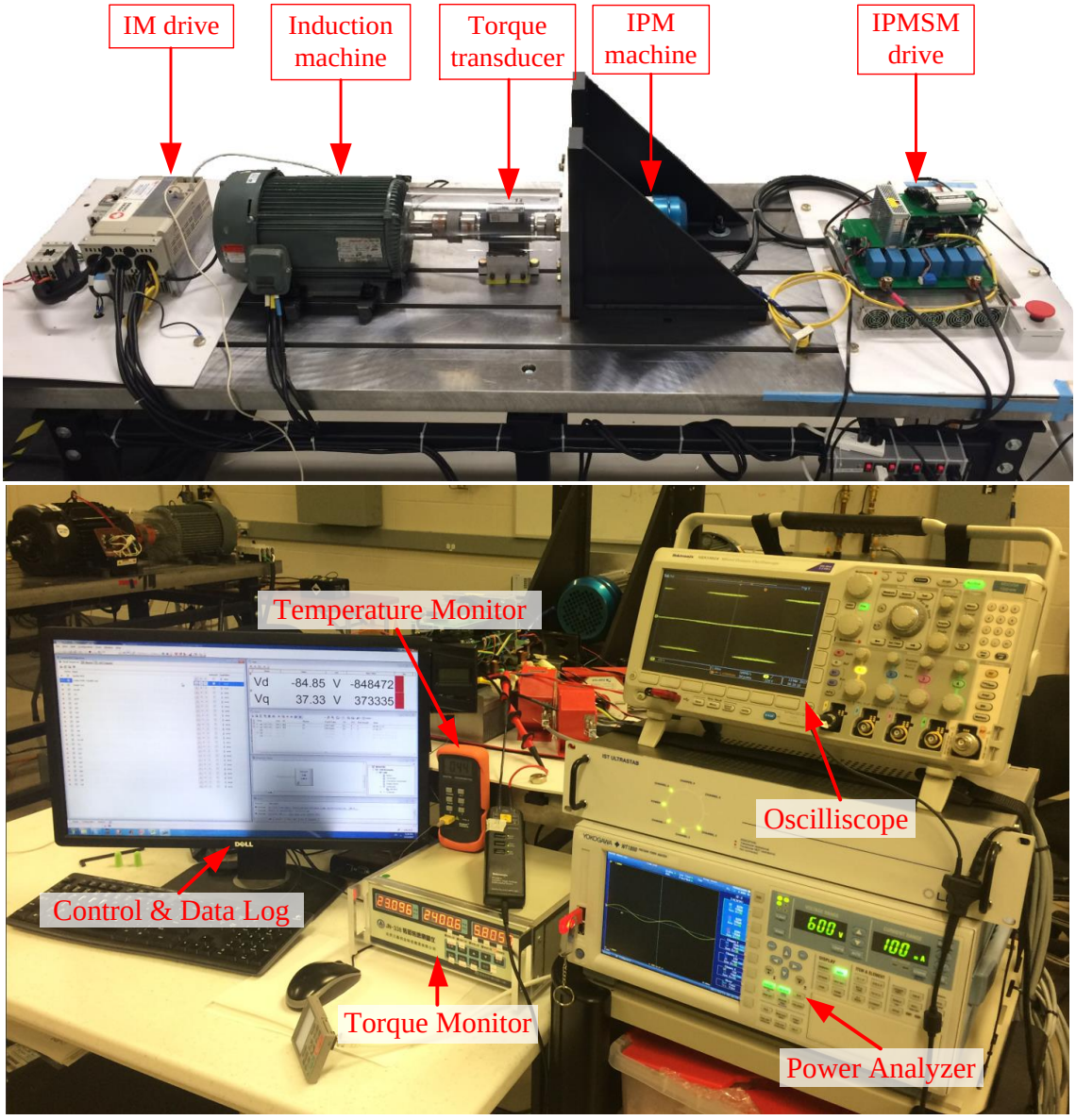

Fig. 3.7. Test bench.

Due to the impact of the voltage estimation on the estimation of the flux-linkage profiles, several methods are applied to decrease the error between the actual voltage and the voltage reference. Firstly, the time delay between the voltage command and the output voltage is taken into account. Secondly, the voltage references are sampled and filtered by the low-pass filter (LPF) in steady-state. Thirdly, the inverter's nonlinearity is compensated. Fig. 3.8 shows the estimated voltage, measured line-to-line voltage and its fundamental component when -16.5A and 16.5A are injected into the *d*- and *q*-axis at 2400rpm. Fig. 3.9 shows the comparison between the voltage measurements and references at nine selected operating points.

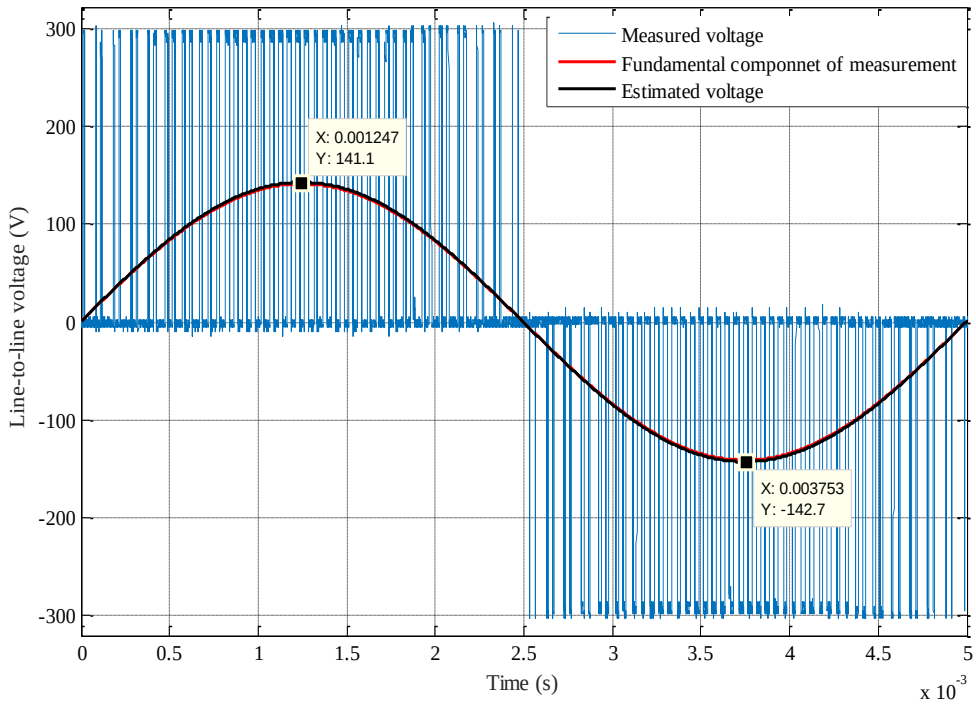

Fig. 3.8. Voltage measurement and estimation at operating point 1.

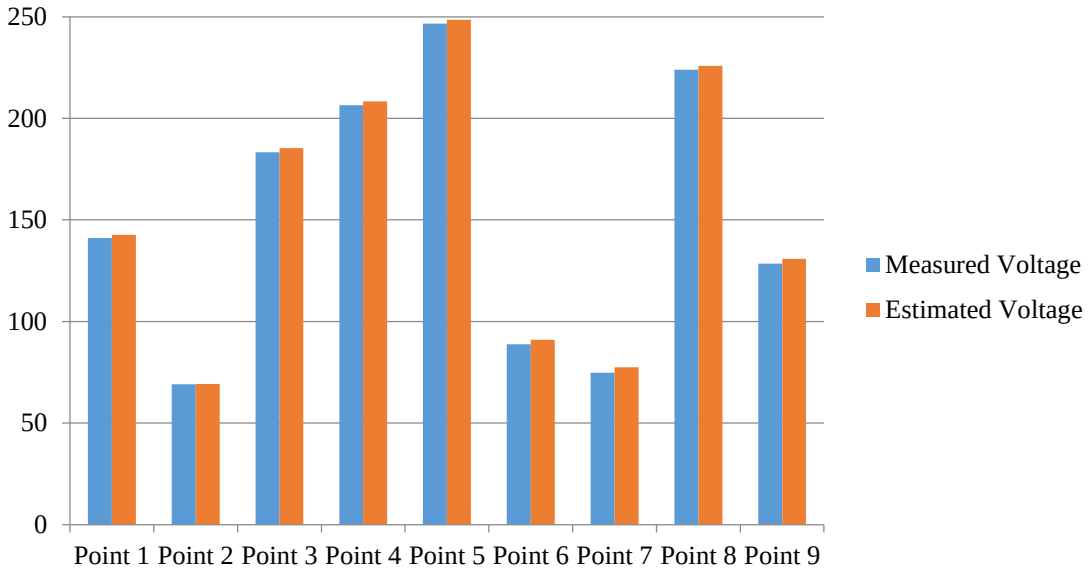

Fig. 3.9. Voltage comparison at the selected operating points.

Tests have been done to examine the variation of the data. Fig. 3.10 shows the flux-linkages calculated by substituting the measurements into (3.9) and (3.10) at nine operating points in 30 Monte Carlo runs. In Fig. 3.11, the variances at each operating point are plotted. The variation of the measurements is negligible. Substitute a random set of the flux-linkage data into (3.5) and twelve coefficients can be obtained by using fmincon in Matlab. The factors' fitting results are listed in Table 3.2.

Table 3.2. Coefficient fitting results for IPMSM under test.

Coefficient	Value	Unit
k_d	0.0725	Wb
k_q	0.0039	Wb
l_d	0.0014	H
l_q	0.002	H
m_d	7.36×10^{-5}	H
m_q	-6.90×10^{-5}	H
d_1	2.68×10^{-6}	H/A
d_2	-4.40×10^{-6}	H/A
d_3	-8.75×10^{-7}	H/A
q_1	-2.0×10^{-6}	H/A
q_2	-7.89×10^{-9}	H/A
q_3	-9.66×10^{-6}	H/A

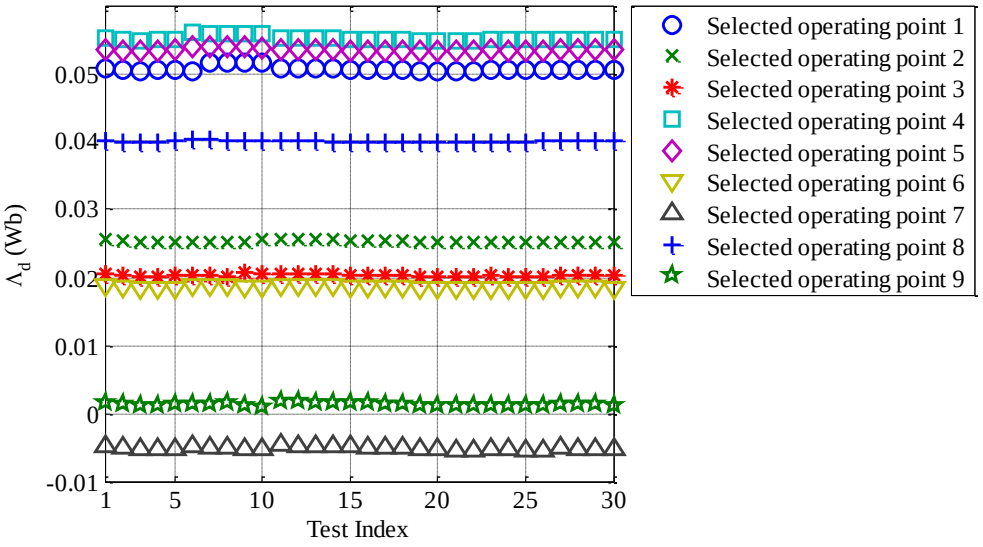

(a)

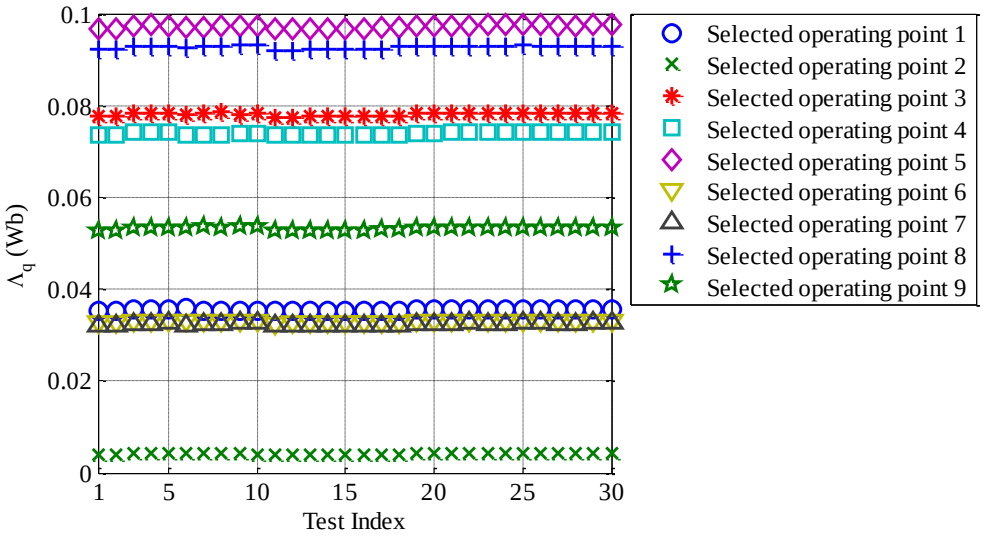

(b)

Fig. 3.10. Measured flux-linkage at the selected operating points: (a) Λ_d. (b) Λ_q.

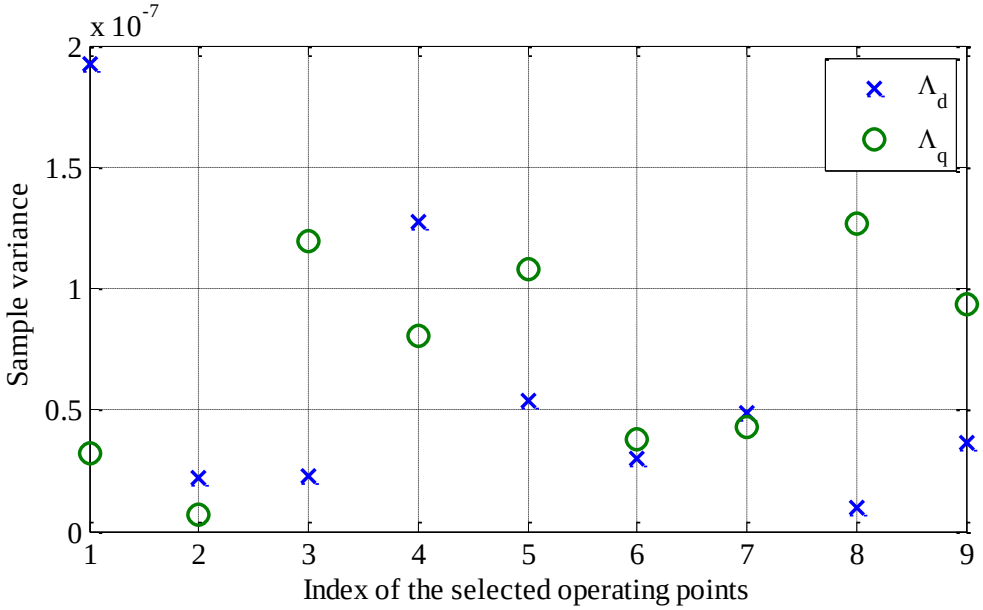

Fig. 3.11. Sample variances.

Fig. 3.12 shows the flux-linkage comparison between the proposed model and the motor under test in both motoring mode and generating mode. In the figure, the black curves are the *d*-axis and *q*-axis flux-linkages calculated by the proposed model with the parameters listed in Table 3.2. The blue and red symbols are the measured flux-linkages. They generally match each other.

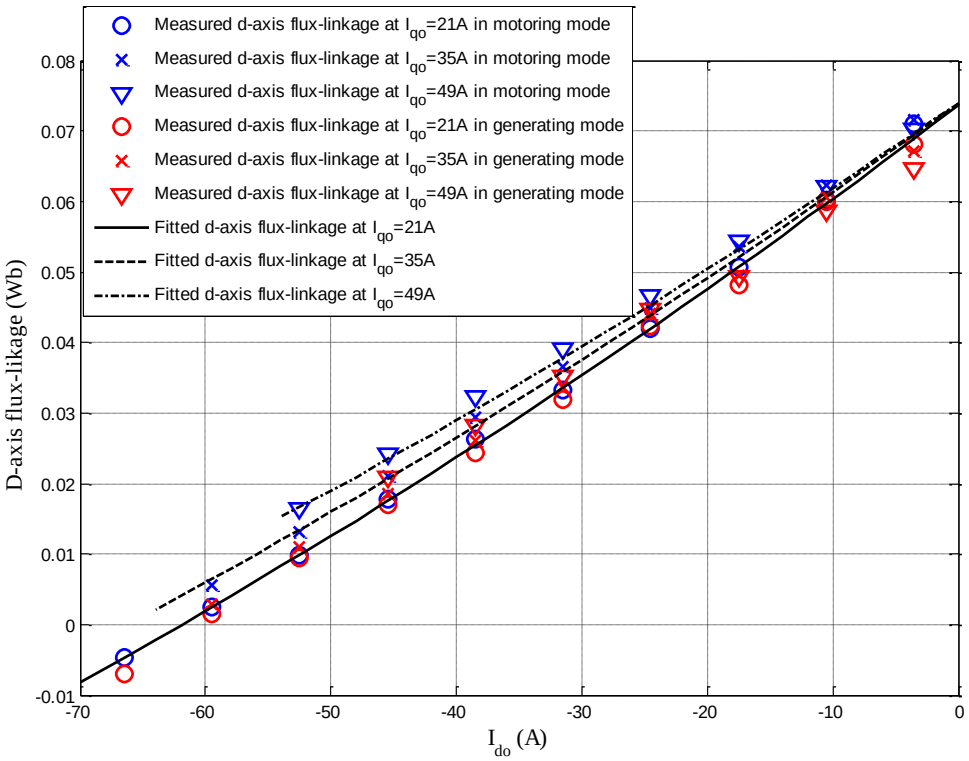
Measured d-axis flux-linkage at I_{qo}=21A in motoring mode
Measured d-axis flux-linkage at I_{qo}=35A in motoring mode
Measured d-axis flux-linkage at I_{qo}=49A in motoring mode
Measured d-axis flux-linkage at I_{qo}=21A in generating mode
Measured d-axis flux-linkage at I_{qo}=35A in generating mode
Measured d-axis flux-linkage at I_{qo}=49A in generating mode
Fitted d-axis flux-linkage at I_{qo}=21A
Fitted d-axis flux-linkage at I_{qo}=35A
Fitted d-axis flux-linkage at I_{qo}=49A
D-axis flux-likage (Wb)
I_{do} (A)
0.08
0.07
0.06
0.05
0.04
0.03
0.02
0.01
0
-0.01
-70
-60
-50
-40
-30
-20
-10
0

(a)

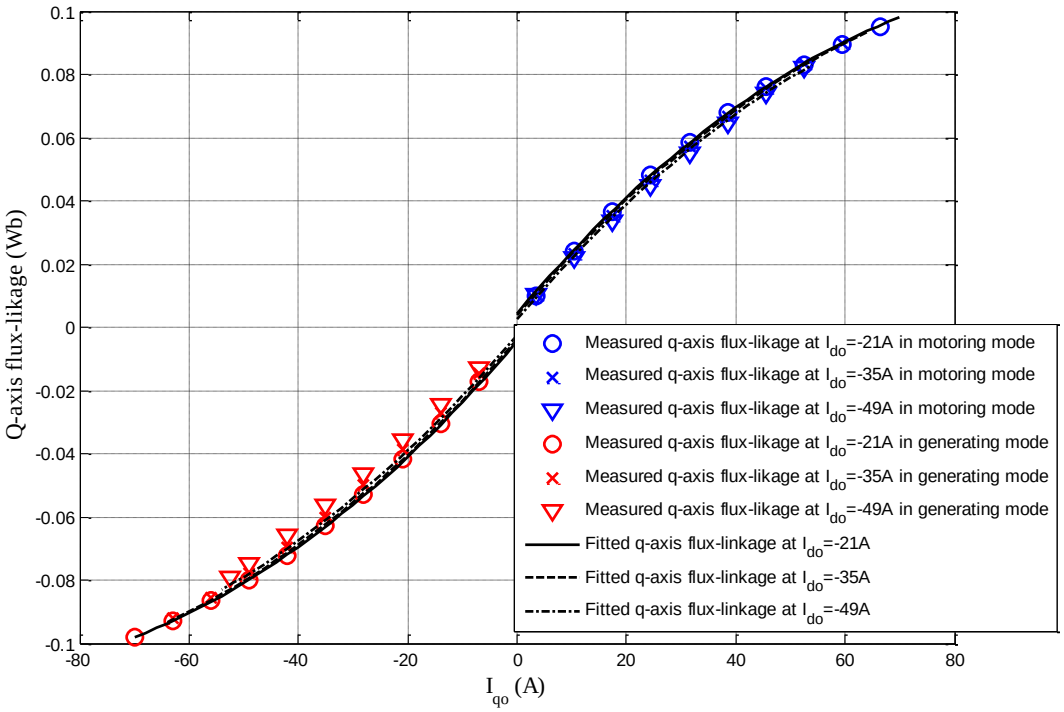

(b)

Fig. 3.12. Flux-linkage comparison between the proposed model and the real IPM machine: (a) Λ_d. (b) Λ_q.

Since the saliency ratio of the IPM machine under test is not very high, different current vectors with the same amplitude might generate the same torque. This phenomenon is well explained in Fig. 3.13. It shows that the different phase angles do not bring big torque differences at the same phase current. MTPA can be obtained by substituting the coefficients in Table 3.2 into (3.8). The fitted MTPA locus is covered by the measured points where the maximum torque is generated. In spite of a little deviation

at the phase currents of 50A and 65A, it only brings torque reduction of 0.1Nm. Thus, the desired copper-loss minimization control can be accomplished by the proposed model.

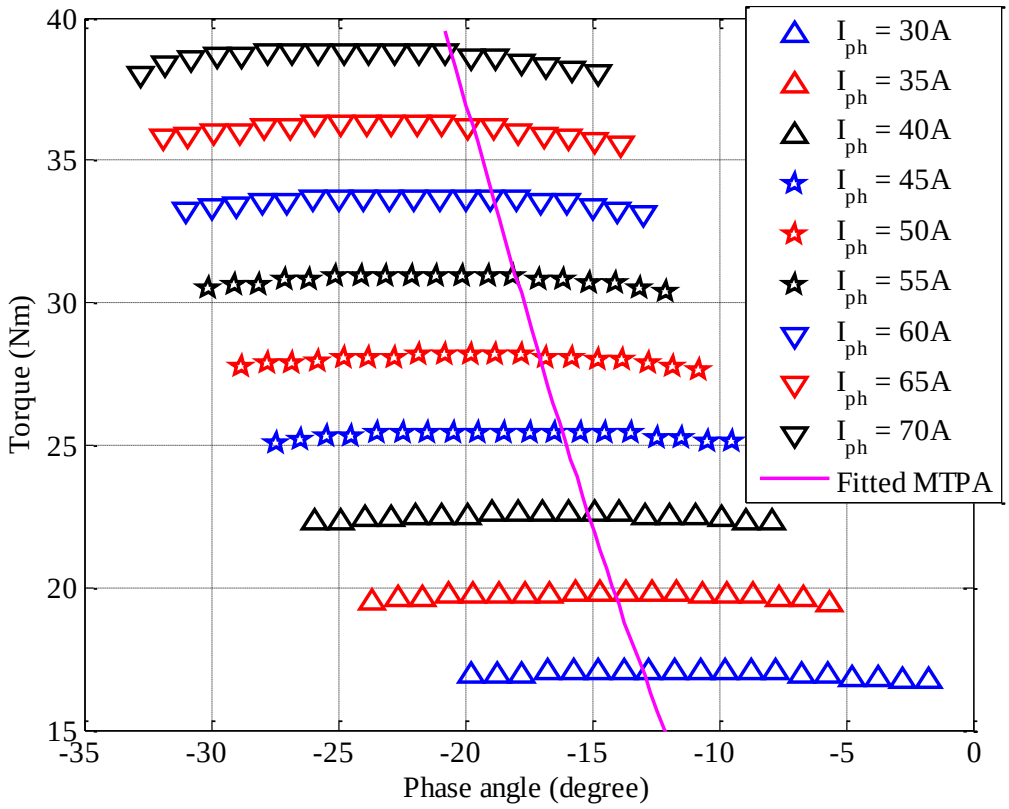

Fig. 3.13. Phase angle vs. measured torque.

If the values of k_d, l_d, and l_q in Table 3.2 are adopted as the permanent-magnet flux-linkage, *d*- and *q*-axis self-inductances, the conventional IPM motor model could be constructed by using (2.1) - (2.3). The corresponding torque identification error is shown in Fig. 3.14. In the flux-weakening region, the estimation error is up to 20%. Due to the mismatch with the real flux-linkage, the model doesn't successfully depict the characteristic of the electromagnetic torque with respect to current.

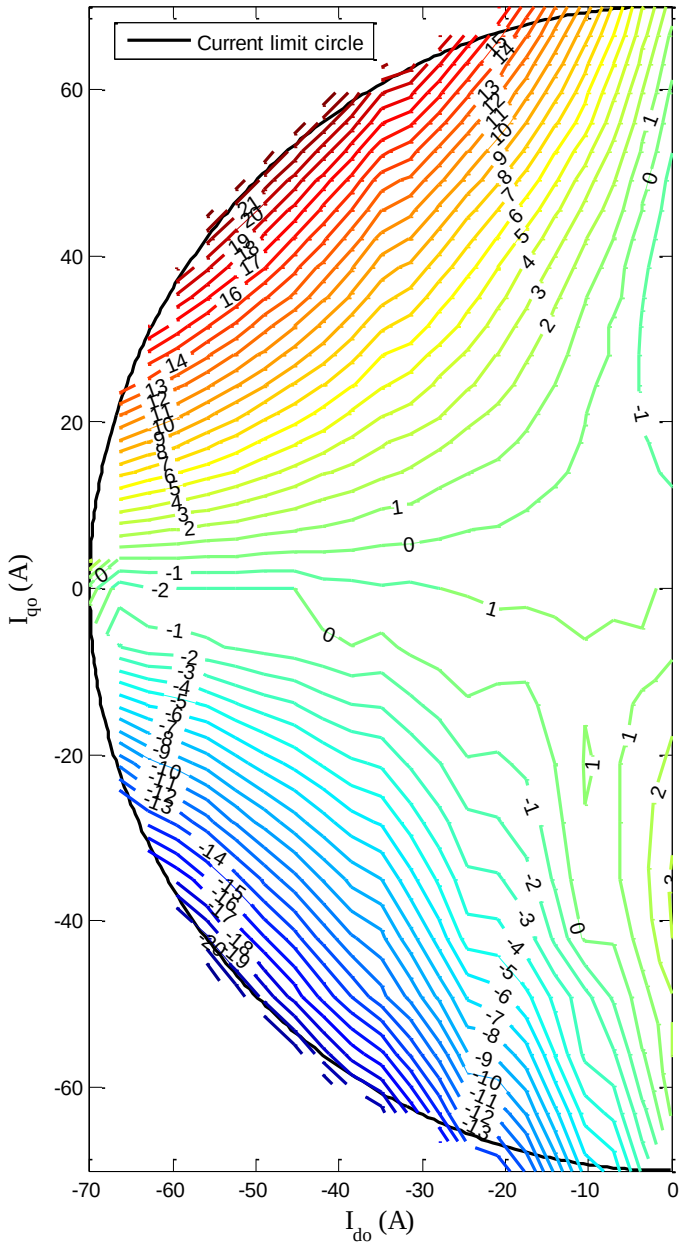

Fig. 3.14. Torque estimation error (%) of IPMSM under test based on the conventional flux-linkage model.

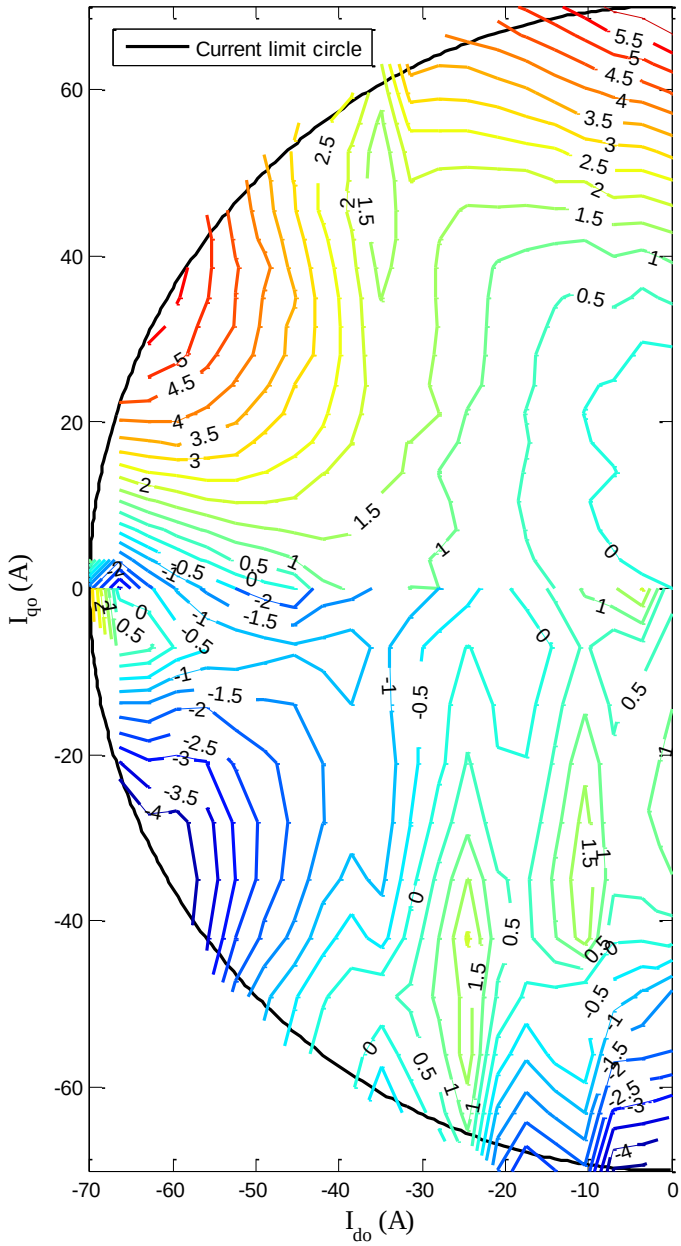

Fig. 3.15. Torque estimation error (%) of IPMSM under test based on the proposed flux-linkage model.

Substitute the coefficients in Table 3.2 into (3.6) then the torque identification based on the proposed flux-linkage model can be accomplished. The estimation accuracy map is shown in Fig. 3.15. The maximum error of torque identification is only 5% in both motoring and generating regions. The torque estimation accuracy is enormously enhanced compared to the conventional IPMSM model.

3.5 Conclusions

A virtual flux-linkage model for IPMSM with constant coefficients is proposed with the aim to fit MTPA control and estimate the torque. By using the flux-linkage data at nine specific operating points, the factors in the model can be determined. During the process, only a few simple experiments are involved. In other words, the flux-linkage nonlinearity of an IPM motor directly bought from the manufacturer can be characterized without FEA analysis because the model is independent of the detailed information of the machine. Compared to the conventional IPM motor model with constant parameters, the proposed flux-linkage model can offer much better torque estimation in both motoring and generating modes by considering the saturation and cross-coupling effects in the machine. The simplicity of the flux-linkage model enables the real-time torque estimation. According to the experimental results, the fitted MTPA locus can offer the maximum torque at certain phase current. The torque estimation error of the tested IPM motor is significantly reduced from 20% by using the conventional IPMSM model to 5% by adopting the proposed model. Except for the applications, in which high-accuracy

torque control, such as automotive, is required, the proposed algorithm can be used for online torque identification with fair precision.

Chapter 4
Loss Minimization Control Based on Proposed Model for Interior Permanent Magnet Synchronous Machine Drives with Constant Parameters

4.1 Introduction

High efficiency is always the pursuit of the researchers and engineers. Even though the permanent magnet synchronous machine is famous for its high power density and high power factor, when it is used for continuous long-time operation, the efficiency becomes an important target in the system design.

Loss minimization control (LMC) aims at minimizing the electrical loss in IPMSM drives. It can be classified into two categories: the search-based and loss-model-based algorithms. In both methods, the total electrical loss of IPMSM is selected as the optimization objective and then optimal current references are selected by solving this optimization problem. In the search-based algorithm, the optimal current references are selected by searching the operating plane in a certain manner, which is independent of the loss model and doesn't require the motor parameters [17]–[19], [29], [68]–[71]. However, it suffers from poor computational efficiency, sensitivity to disturbances and poorer torque ripples [15]. Compared to the search based algorithm, the loss-model-based

algorithm is much more time-efficient, but it is difficult to obtain the analytical solution to the optimization problem [25]–[29], [72]–[74].

The control of IPMSM drives should be based on the accurate model. In order to improve the accuracy of the IPMSM models, the core losses are represented as an equivalent core-loss resistor connected to the flux-linkage in parallel in the *dq* equivalent circuit models in [32], [36], [43], [45], [46], [75]–[79]. In addition, the loss and the voltage drop of the inverter should also be considered for accurate modeling of IPMSM drives.

In this chapter, a novel model of IPMSM drive with all the losses considered, including the copper loss, iron losses, and inverter loss, is proposed. Based on the model, the loss minimization control and the optimization constraints are studied. Firstly, the analytical solution to the optimal current in the flux-linkage branches for given torque and speed is provided. Secondly, the optimization problem with respect to the winding current is formulated within the operating constraints. The strategy to prove the optimality is presented. Thirdly, the influence of the stator-winding, inverter-loss and core-loss resistance on the current and voltage limits with respect to i_{dq} and i_{dqo} is analyzed, respectively. Lastly, simulation results are provided to validate the proposed algorithms.

4.2 Proposed Model for IPMSM Drives

4.2.1 Losses in IPMSM Drive System

The power flow of IPMSM drives is shown in Fig. 4.1. The electrical input power is consumed by the inverter and IPMSM as loss power before it is transformed into the mechanical output power.

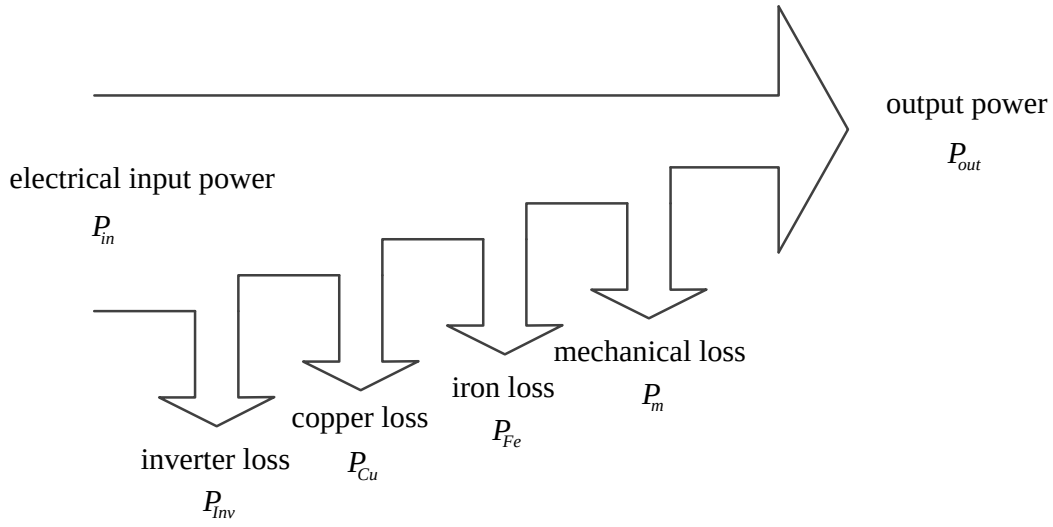

Fig. 4.1. Power flow of IPMSM drive system.

IPMSM has high power density because it has the reluctance torque and no rotor copper loss. The losses of the IPM machine can be categorized into electrical loss and mechanical loss P_m. The electrical loss includes the copper loss P_{Cu} and iron loss P_{Fe}. The stray loss of IPMSM is generated by the non-uniform current distribution and magnetic flux distribution [33], [80]. Generally, it only accounts for 3-5% of the total loss of the machine [80] and thus the stray loss is ignored for modeling.

4.2.2 Proposed Steady-State Equivalent Circuit Model of IPMSM Drives

Based on the power flow, the equivalent circuit for IPMSM drives in steady-state is shown in Fig. 4.2.

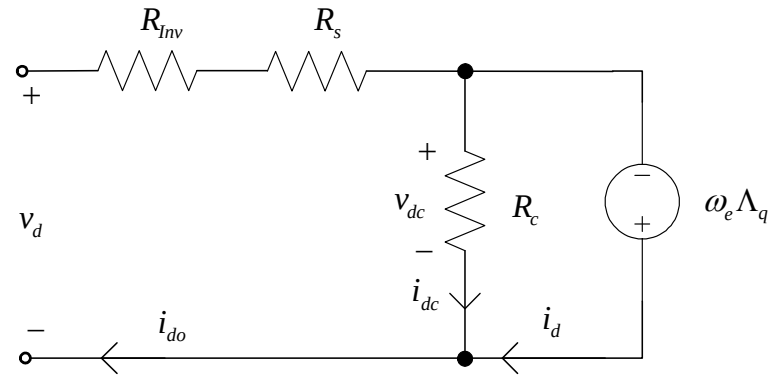

(a)

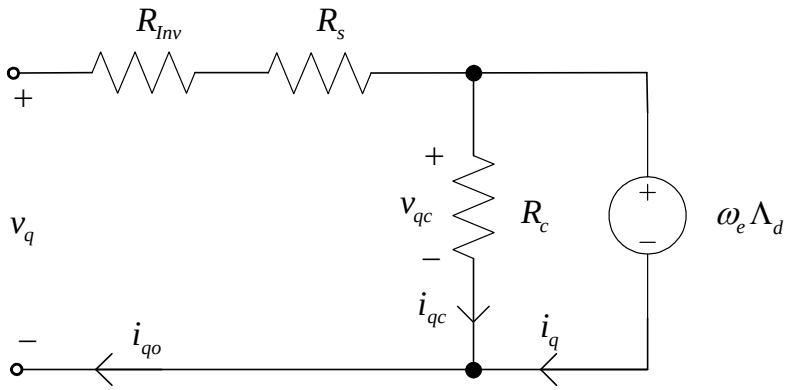

(b)

Fig. 4.2. The proposed equivalent circuit of IPMSM drives. (a) *d*-axis. (b) *q*-axis.

In the circuits, v_d and v_q are the voltage inputs of the inverter. R_{Inv} is the equivalent inverter-loss resistance. Because the core loss is generated by the rotating flux-linkage, the equivalent resistance R_c is placed across the flux-linkage branch in parallel. The flux-linkage expression is written in (4.1). Compared to (2.1), i_{dq} is used in the equation. The steady-state voltage equation is listed in (4.2).

$$\begin{bmatrix} \Lambda_d \\ \Lambda_q \end{bmatrix} = \begin{bmatrix} L_d & 0 \\ 0 & L_q \end{bmatrix} \begin{bmatrix} i_d \\ i_q \end{bmatrix} + \begin{bmatrix} \Lambda_{pm} \\ 0 \end{bmatrix} \tag{4.1}$$

$$\begin{bmatrix} v_d \\ v_q \end{bmatrix} = \left(R_s + R_{Inv} \right) \begin{bmatrix} i_{do} \\ i_{qo} \end{bmatrix} + \omega_e \begin{bmatrix} -\Lambda_q \\ \Lambda_d \end{bmatrix} \tag{4.2}$$

where, i_d an i_q are the d- and q-axis current contributing to flux-linkage generation. They flow in the flux-linkage branches as shown in Fig. 4.2.

The power flow in IPMSM drive system is expressed by (4.3).

$$P_{in} = P_{Inv} + P_{Cu} + P_{Fe} + P_m + P_{out} \tag{4.3}$$

where,

$$P_{in} = \frac{3}{2}\left(v_d i_{do} + v_q i_{qo} \right); \tag{4.4}$$

$$\begin{aligned} P_{Inv} &= 6\left(P_{IGBT\_conduction} + P_{diode\_conduction} \right) + 6\left(P_{IGBT\_switching} + P_{diode\_switching} \right) \\ &= \frac{3}{2} R_{Inv} \left(i_{do}^2 + i_{qo}^2 \right); \end{aligned} \tag{4.5}$$

$$P_{Cu} = \frac{3}{2} R_s \left(i_{do}^2 + i_{qo}^2 \right); \tag{4.6}$$

$$P_{Fe} = \frac{3}{2}\frac{\omega_e^2\left(\Lambda_d^2 + \Lambda_q^2\right)}{R_c}; \tag{4.7}$$

$$P_m = T_{fric}\omega_m; \tag{4.8}$$

$$P_{out} = T_o\omega_m. \tag{4.9}$$

Where $P_{IGBT\_conduction}$, $P_{diode\_conduction}$, $P_{IGBT\_switching}$, $P_{diode\_switching}$ are the conduction losses and switching losses of IGBT and diode, respectively; P_{in} is the electrical input power; P_{Inv} is the inverter loss; T_{fric} and T_o are the friction torque and mechanical output torque, respectively.

The resultant torque on the shaft can be calculated as shown in (4.10).

$$T_o = \frac{3}{2}P\left(\Lambda_d i_q - \Lambda_q i_d\right) - T_{fric} \tag{4.10}$$

where,

$$i_d = i_{do} + \frac{\omega_e\Lambda_q}{R_c}; \tag{4.11}$$

$$i_q = i_{qo} - \frac{\omega_e\Lambda_d}{R_c}. \tag{4.12}$$

It should be noted that all the parameters in the proposed IPMSM drive model, such as R_{Inv}, R_c, L_d, L_q, and Λ_{pm}, in this chapter are considered as constants.

4.3 Loss Minimization Control with Respect to the Current in the Flux-Linkage Branch

4.3.1 Unconstrained Loss Minimization Control

In order to achieve high efficiency, for the given torque and speed, the power loss should be minimized. In the proposed the loss minimization control algorithm, the total electrical loss of the IPMSM drives is selected as the optimization objective.

According to the equivalent circuit shown in Fig. 4.2, the analytical expression of the optimal current that contributes to the flux-linkage generation can be derived. First of all, the total electrical loss P_E is defined by (4.13).

$$P_E = P_{Inv} + P_{Cu} + P_{Fe} \tag{4.13}$$

Substitute (4.6), (4.7), (4.11) and (4.12) into (4.13), the total electrical loss with respect to i_{dq} can be obtained as shown in (4.14).

$$P_E = \frac{3}{2}\left\{\begin{array}{l}\left(R_s + R_{Inv}\right)\left[\left(i_d - \dfrac{\omega_e L_q i_q}{R_c}\right)^2 + \left(i_q + \dfrac{\omega_e\left(\Lambda_{pm} + L_d i_d\right)}{R_c}\right)^2\right] \\ + \dfrac{\left(\omega_e L_q i_q\right)^2}{R_c} + \dfrac{\omega_e^2\left(\Lambda_{pm} + L_d i_d\right)^2}{R_c}\end{array}\right\} \tag{4.14}$$

In steady-state, the machine's torque and speed are constant. The torque equation (4.10) can be transformed as shown in (4.15).

$$i_q = \frac{2T_e}{3P\left[\Lambda_{pm} + \left(L_d - L_q\right) i_d\right]} \tag{4.15}$$

where, $T_e = T_e^* + T_{fric}$. T_e^* is the torque command.

Substitute (4.15) into (4.14), then the total electrical loss becomes a function of i_d. If $\frac{\partial P_E}{\partial i_d} = 0$ is taken as the loss minimization condition, the optimal *d*-axis current can be obtained by solving the equation (4.16) as shown below.

$$a i_d^4 + b i_d^3 + c i_d^2 + d i_d + e = 0 \tag{4.16}$$

where,

$$a = 18P^2 R_c \left(L_d - L_q\right)^3 \left[\left(R_s + R_{Inv}\right) R_c + \omega_e^2 L_d^2\right];$$

$$b = 18P^2 \Lambda_{pm} \left(L_d - L_q\right)^2 \cdot \left[3\left(R_s + R_{Inv}\right) R_c^2 + 3\omega_e^2 \left(R_s + R_{Inv} + R_c\right) L_d^2 + \omega_e^2 L_d \left(R_s + R_{Inv} + R_c\right)\left(L_d - L_q\right)\right];$$

$$c = 54P^2 \Lambda_{pm}^2 \left(L_d - L_q\right) \cdot \left[\left(R_s + R_{Inv}\right) R_c^2 + \omega_e^2 \left(R_s + R_{Inv} + R_c\right) L_d^2 + \omega_e^2 L_d \left(R_s + R_{Inv} + R_c\right)\left(L_d - L_q\right)\right];$$

$$d = 18P^2 \Lambda_{pm}^3 \cdot \left[\left(R_s + R_{Inv}\right) R_c^2 + \omega_e^2 \left(R_s + R_{Inv} + R_c\right) L_d^2 + 3\omega_e^2 L_d \left(R_s + R_{Inv} + R_c\right)\left(L_d - L_q\right)\right];$$

$$e = 18P^2 \omega_e^2 L_d \Lambda_{pm}^4 \left(R_s + R_{Inv} + R_c\right) - 8T_e^2 \left(L_d - L_q\right)\left[\left(R_s + R_{Inv}\right) R_c^2 + \omega_e^2 \left(R_s + R_{Inv} + R_c\right) L_q^2\right].$$

By changing the variables the quartic equation can be factorized into two quadratic equations [81]. The optimal *d*-axis current reference can be written as a function of the torque and speed.

$$\begin{cases} i_{d_{1,2}}^{*} = -\dfrac{b}{4a} - S \pm \dfrac{1}{2}\sqrt{-4S^2 - 2\sigma + \dfrac{\gamma}{S}} \\ i_{d_{3,4}}^{*} = -\dfrac{b}{4a} + S \pm \dfrac{1}{2}\sqrt{-4S^2 - 2\sigma - \dfrac{\gamma}{S}} \end{cases} \tag{4.17}$$

where,

$$\sigma = \frac{8ac - 3b^2}{8a^2};$$

$$\gamma = \frac{b^3 - 4abc + 8a^2 d}{8a^3};$$

$$S = \frac{1}{2}\sqrt{-\frac{2}{3}\sigma + \frac{1}{3a}\left(Q + \frac{\tau_0}{Q}\right)};$$

$$Q = \sqrt[3]{\frac{\tau_1 + \sqrt{\tau_1^2 - 4\tau_0^3}}{2}};$$

$$\tau_0 = c^2 - 3bd + 12ae;$$

$$\tau_1 = 2c^3 - 9bcd + 27b^2 e + 27ad^2 - 72ace.$$

Specific judgment should be done to select the proper *d*-axis current references from four roots, which is supposed to be negative real. Once the parameters are defined, which root is the appropriate solution is determined. The corresponding optimum *q*-axis current reference can be obtained from equation (4.15).

4.3.2 Optimization Constraints

With the equivalent inverter-loss and core-loss resistance introduced into the equivalent circuit, the current and voltage limits in (2.4) and (2.5) are transformed into (4.18) and (4.19), respectively.

$$\begin{aligned}&\left(i_d-\frac{\omega_e L_q i_q}{R_c}\right)^2+\left(i_q+\frac{\omega_e L_d i_d+\omega_e \Lambda_{pm}}{R_c}\right)^2=I_{a\mathrm{m}}^2\\&\Rightarrow Ai_d^2+Bi_d i_q+Ci_q^2+Di_d+Ei_q+F=0\end{aligned}\tag{4.18}$$

where,

$$A=1+\frac{\omega_e^2 L_d^2}{R_c^2};$$

$$B=\frac{2\omega_e}{R_c}\left(L_d-L_q\right);$$

$$C=1+\frac{\omega_e^2 L_q^2}{R_c^2};$$

$$D=\frac{2\omega_e^2 L_d \Lambda_{pm}}{R_c^2};$$

$$E=\frac{2\omega_e \Lambda_{pm}}{R_c};$$

$$F=\frac{\omega_e^2 \Lambda_{pm}^2}{R_c^2}-I_{am}^2.$$

$$\begin{aligned}
&\left[\left(R_s+R_{Inv}\right)i_d-\left(1+\frac{R_s+R_{Inv}}{R_c}\right)\omega_e L_q i_q\right]^2 \\
&+\left[\left(R_s+R_{Inv}\right)i_q+\omega_e\left(1+\frac{R_s+R_{Inv}}{R_c}\right)L_d i_d+\omega_e\Lambda_{pm}\left(1+\frac{R_s+R_{Inv}}{R_c}\right)\right]^2=V_{am}^2 \\
&\Rightarrow Ai_d^2+Bi_d i_q+Ci_q^2+Di_d+Ei_q+F=0
\end{aligned} \tag{4.19}$$

where,

$$A=\left(R_s+R_{Inv}\right)^2+\omega_e^2 L_d^2\left(1+\frac{R_s+R_{Inv}}{R_c}\right)^2;$$

$$B=2\omega_e\left(R_s+R_{Inv}\right)\left(L_d-L_q\right)\left(1+\frac{R_s+R_{Inv}}{R_c}\right);$$

$$C=\left(R_s+R_{Inv}\right)^2+\omega_e^2 L_q^2\left(1+\frac{R_s+R_{Inv}}{R_c}\right)^2;$$

$$D=2\omega_e^2 L_d\Lambda_{pm}\left(1+\frac{R_s+R_{Inv}}{R_c}\right)^2;$$

$$E=2\omega_e\Lambda_{pm}\left(R_s+R_{Inv}\right)\left(1+\frac{R_s+R_{Inv}}{R_c}\right);$$

$$F=\omega_e^2\Lambda_{pm}^2\left(1+\frac{R_s+R_{Inv}}{R_c}\right)^2-V_{am}^2.$$

Both current and voltage constraints become the distorted ellipses. The shifted center, rotation angle, major axis, and the minor axis of the constraints are listed in (4.20)-(4.23), respectively.

$$\left(\frac{EB-2CD}{4AC-B^2},\frac{BD-2AE}{4AC-B^2}\right) \tag{4.20}$$

$$\frac{1}{2}\arctan\left(\frac{B}{A-C}\right) \tag{4.21}$$

$$\sqrt{\frac{2\left(AE^2+CD^2+B^2F-BDE-4ACF\right)}{\left(B^2-4AC\right)\left[\sqrt{\left(A-C\right)^2+B^2}-\left(A+C\right)\right]}} \tag{4.22}$$

$$\sqrt{\frac{2\left(AE^2+CD^2+B^2F-BDE-4ACF\right)}{\left(B^2-4AC\right)\left[-\sqrt{\left(A-C\right)^2+B^2}-\left(A+C\right)\right]}} \tag{4.23}$$

4.3.3 Simulation Results

The proposed LMC algorithm is validated in simulation. The parameters of the IPMSM are listed in Table 4.1.

In Fig. 4.3 the top figure shows the electrical losses versus i_d at different electrical angular speed under 100Nm constant torque. The MTPA, MTPV, and LMC loci at different speeds are plotted at the bottom in Figure 4.3. The 100Nm torque curve has four intersections with the LMC loci. The '*****' points mark the minimum electrical losses at certain speed. They correspond to the intersections '+' of the constant torque locus and the LMC loci. It indicates that the current references decided by the proposed LMC algorithm produce the minimum electrical loss of the machine. It should be noted that the voltage limit is not considered in Fig. 4.3.

Table 4.1. IPMSM parameters.

Parameter	Value	Unit
Pole pair	3	N/A
R_s	0.0236	Ω
R_{Inv}	0.0059	Ω
Λ_{pm}	0.07	Wb
L_d	0.375	mH
L_q	0.835	mH
R_c	24	Ω
I_{am}	379	A
V_{dc}	300	V

Different values for the core-loss resistance have been applied. When the resistance is larger, the LMC locus stands closer to MTPA curve due to less core loss and the copper loss accounts for the larger proportion of the total electrical losses. Thus, the optimum current reference is close to the one optimized by MTPA control. On the contrary, when the equivalent core-loss resistance is smaller, the LMC locus moves farther away from MTPA curve.

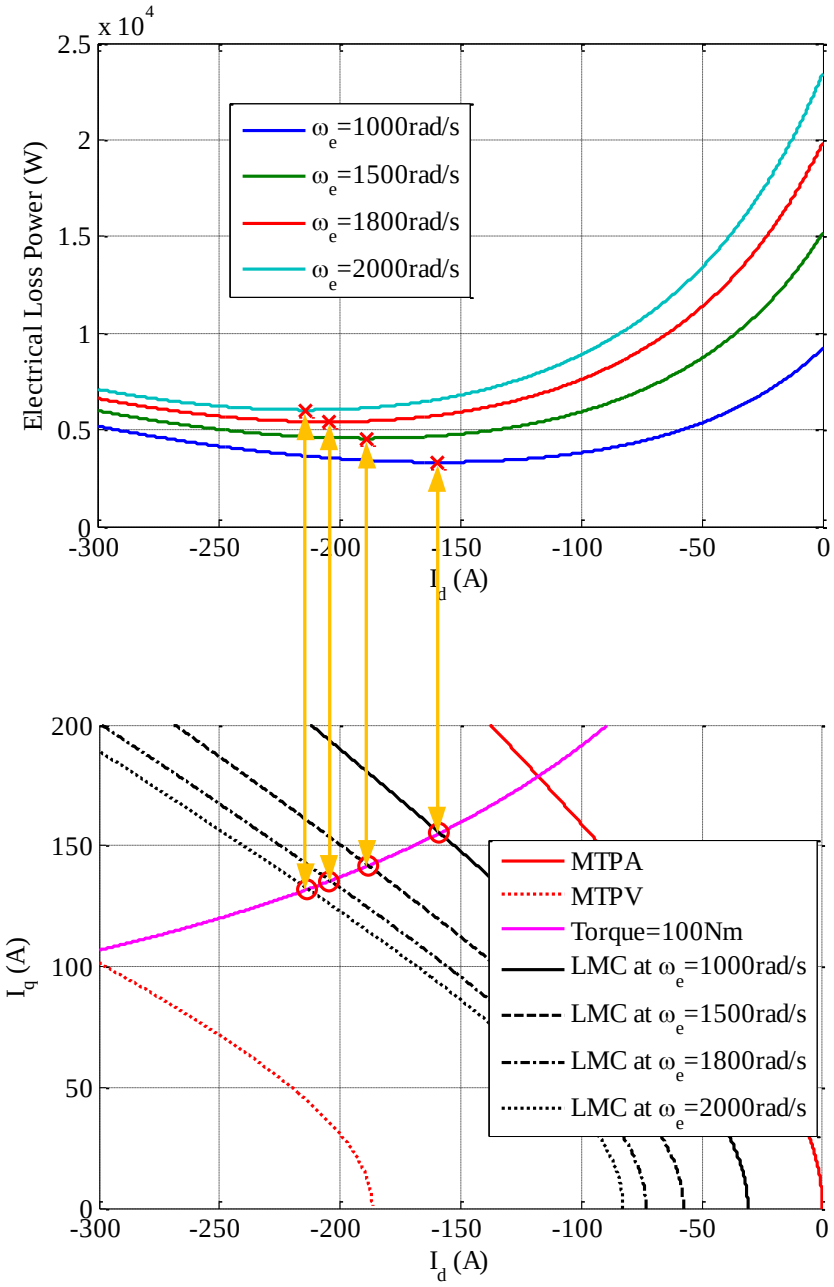

Fig. 4.3. Electrical loss power vs. *d*-axis current at 100Nm and the optimal current reference map.

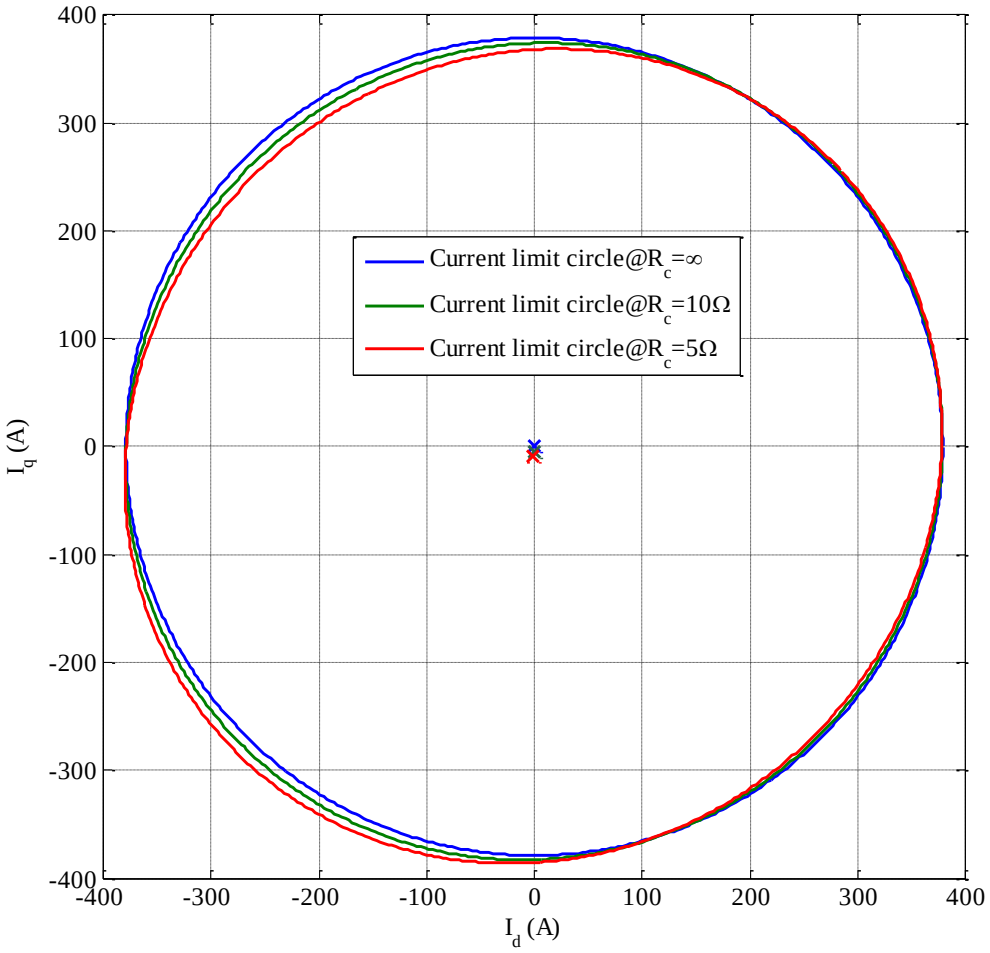

Fig. 4.4. Current limit with different the iron-loss resistances considered.

In Fig. 4.4 it shows the influence of R_c on the current constraint. The blue curve depicts the current limit without the existence of core loss in the IPM machine. In this case, $i_d = i_{do}$ and $i_q = i_{qo}$, and the current constraint is a regular circle as described in (2.4). The core-loss resistor draws current from the stator winding as shown in Fig. 4.2. In Fig. 4.4 the green and red curves indicate that the current constraint is shifted and rotated because of

the core-loss resistor. When the core loss is larger, the equivalent core-loss resistance is smaller and the more distortion of the current constraint can be detected.

Fig. 4.5 shows the influence of the parameters on the voltage constraint. The effect of the variation of the stator-winding and inverter-loss resistance on the voltage limit ellipse is shown in Fig. 4.5(a). In the figure, R_c is set to infinity. In this case, $i_d = i_{do}$ and $i_q = i_{qo}$. The blue curve represents the voltage constraint, whose center is located on the *d*-axis, neglecting the voltage drop across the resistors and the core loss. When R_s and R_{Inv} are taken into account, the ellipse rotates counterclockwise and its center is shifted into the third quadrant. When the resistance increases, the voltage limit ellipse rotates more and shrinks. This occurs because the resistors are connected in series in the equivalent circuit. The voltage drop across the resistor grows as the resistance increases. It is easier to reach the voltage limit in the motoring mode and more difficult in generating mode. In Fig. 4.5(b) $R_s + R_{Inv} = 0.0295\Omega$. The blue curve shows the voltage constraint considering only the resistors in series. The green and red ellipses are drawn with the core loss included. It can be seen that when the core loss is considered, the voltage limit ellipse rotates counterclockwise; when the equivalent resistance becomes smaller, the ellipse shrinks.

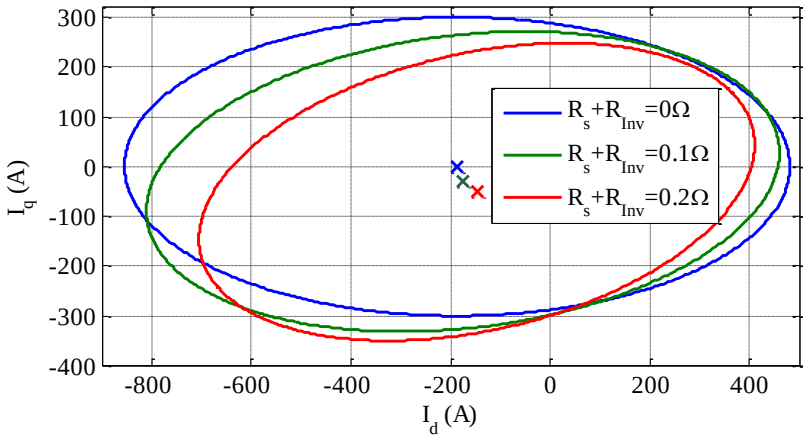

(a)

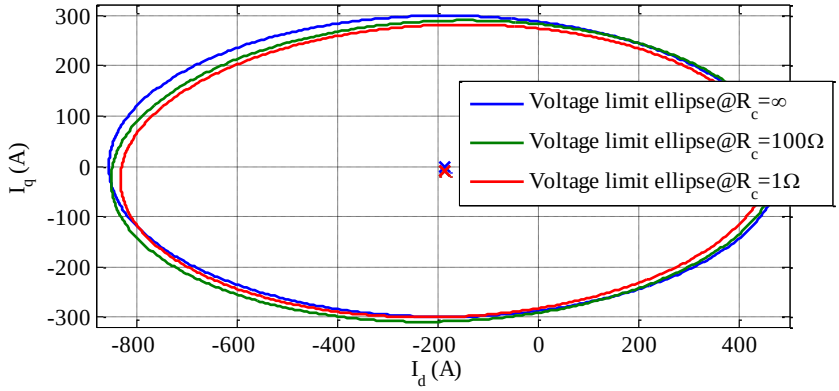

(b)

Fig. 4.5. Influence of the parameters on the voltage constraint in i_{dq} coordinates. (a) The stator-winding and inverter-loss resistance. (b) The core-loss resistance.

The efficiency comparison between MTPA control and the proposed LMC algorithm is shown in Fig. 4.6 and Fig. 4.7. The efficiency calculation is based on $\eta = \frac{P_{out}}{P_{out} + P_E} \times 100\%$, where the mechanical loss is not included. It should be noted that the contours in both figures are not the torque-speed envelopes for the IPM machine. Instead, they cover the region where MTPA/LMC can be applied. When the core loss considered, more *d*-axis current is injected for demagnetization. It is why LMC can be adopted at higher speed. In this case, the iron loss decreases as the *d*-axis flux-linkage decreases. Compared to MTPA, LMC promises to be more efficient since it considers all the electrical losses in the IPMSM drive system.

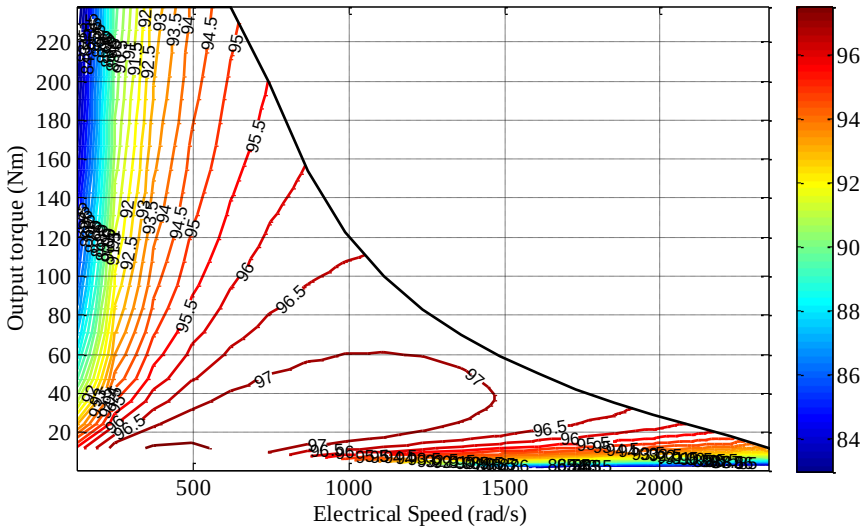

Fig. 4.6. Efficiency map of MTPA control.

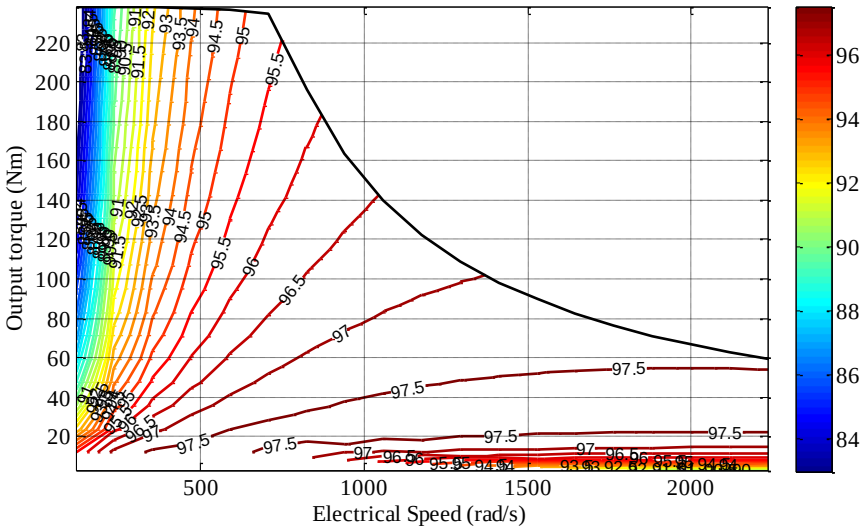

Fig. 4.7. Efficiency map of proposed LMC.

4.4 Loss Minimization Control with Respect to the Stator-Winding Current

The loss minimization control and the operating constraints are presented previously, with respect to i_{dq}. It is beneficial to provide the interior picture of the IPMSM drives. Besides, i_{dq} contributes to the flux-linkage generation, and directly affects the torque production. However, the physically controllable current is the stator-winding current. The optimal phase current can be obtained by substituting (4.17) and (4.15) into (4.11) and (4.12). In order to comprehensively analyze the problem, in this section, the optimization problem is studied in i_{dqo} coordinates within full-speed range, based on the proposed IPMSM drive model in section 4.2.2.

4.4.1 Analysis of the Optimization Problem

The optimization plane is shown in Fig. 4.8, in which $T_1 > T_2$ and $\omega_1 < \omega_2$. The optimization is limited by the current circle and voltage ellipse. The proposed LMC curves are plotted in yellow; MTPV is drawn in green; the constant torque loci are in red; the current limit circle is in black; and the voltage limit ellipses are in blue.

Below base speed and within the current limit circle, it is an equality-constrained optimization problem: the optimal current reference will be found to minimize the total electrical loss at the given torque. The maximum output torque is limited by the power of the IPMSM itself. It means that the optimum current command at point A is determined by the machine's peak current, where the constant torque locus tangentially intersects the current limit circle. The voltage limit ellipse at ω_1 defines the base speed, $\omega_b = \omega_1$. The optimal operating point is located at the intersection of LMC and constant torque locus, like point G.

In the flux-weakening region, both the current and voltage constraints limit the range of the feasible operating point. In this case, it becomes a mixed-constraints optimization problem. For example, for given torque T_2 at ω_2, the optimal operating point is point E, where the voltage limit ellipse at ω_2 and constant torque locus intersect, instead of the intersection of LMC@ω_2 and T_2, which is located outside of the voltage limit ellipse and cannot be achieved.

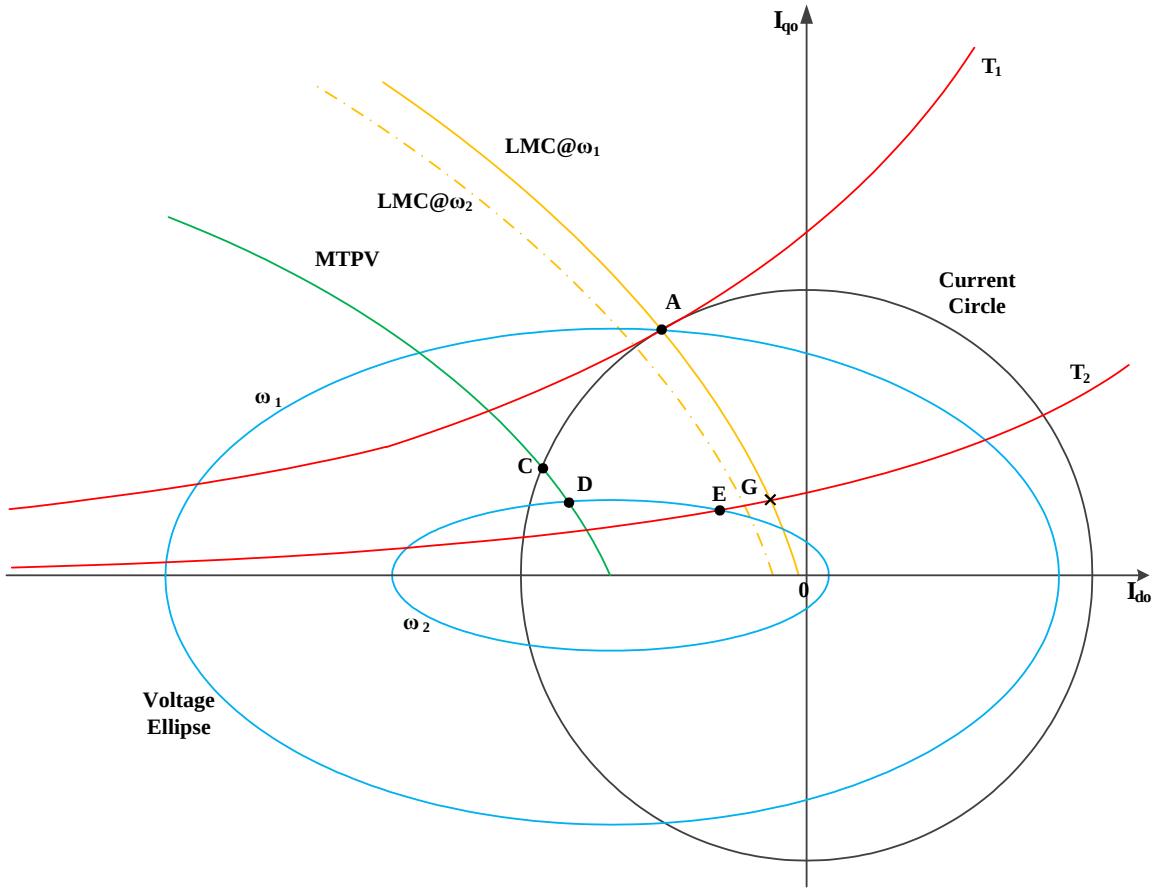

Fig. 4.8. Selection of optimal current vector based on proposed IPMSM drive model.

MTPV can be formulated as the maximization of the electromagnetic torque along the voltage limit ellipse, which is also an equality-constrained optimization problem.

The current limit circle is a round circle and its center is located at the origin, as described in (2.4). Compared to the voltage constraint in (2.6), the voltage limit ellipse formulated by using the proposed IPMSM drive model is shifted, rotated and distorted.

4.4.2 Loss Minimization Control within Operating Constraint

The analytical model of the loss minimization control for a given torque T_o^* below base speed can be formulated as shown in (4.24).

Minimize

$$\begin{aligned} f_e\left(i_{do}, i_{qo}\right) &= P_{Cu} + P_{Inv} + P_{Fe} \\ &= \frac{3}{2}\left(R_s + R_{Inv}\right)\left(i_{do}^2 + i_{qo}^2\right) + \frac{3\omega_e^2}{2R_c}\left(\Lambda_d^2 + \Lambda_q^2\right) \end{aligned} \tag{4.24}$$

Subject to

$$\begin{aligned} h\left(i_{do}, i_{qo}\right) &= \frac{3}{2}P\left(\Lambda_d i_q - \Lambda_q i_d\right) - \left(T_{fric} + T_o^*\right) \\ &= a i_{do}^2 + b i_{qo}^2 + c i_{do} i_{qo} + d i_{do} + e i_{qo} + f \end{aligned}$$

where,

$$i_d = m_d i_{do} + n_d i_{qo} + k_d;$$

$$i_q = m_q i_{do} + n_q i_{qo} + k_q;$$

$$m_d = \frac{R_c^2}{R_c^2 + \omega_e^2 L_d L_q} = n_q;$$

$$n_d = \frac{R_c \omega_e L_q}{R_c^2 + \omega_e^2 L_d L_q};$$

$$k_d = -\frac{\omega_e^2 L_q \Lambda_{pm}}{R_c^2 + \omega_e^2 L_d L_q};$$

$$m_q = -\frac{R_c \omega_e L_d}{R_c^2 + \omega_e^2 L_d L_q};$$

$$k_q = -\frac{R_c \omega_e \Lambda_{pm}}{R_c^2 + \omega_e^2 L_d L_q};$$

$$a = \frac{3}{2} P\left(L_d - L_q\right) m_d m_q;$$

$$b = \frac{3}{2} P\left(L_d - L_q\right) n_d n_q;$$

$$c = \frac{3}{2} P\left(L_d - L_q\right)\left(m_d n_q + n_d m_q\right);$$

$$d = \frac{3}{2} P\left[\Lambda_{pm} m_q + \left(L_d - L_q\right)\left(m_d k_q + k_d m_q\right)\right];$$

$$e = \frac{3}{2} P\left[\Lambda_{pm} n_q + \left(L_d - L_q\right)\left(n_d k_q + k_d n_q\right)\right];$$

$$f = \frac{3}{2} P\left[\Lambda_{pm} k_q + \left(L_d - L_q\right) k_d k_q\right] - \left(T_{fric} + T_o^*\right).$$

According to the optimization theory, the constrained optimization problem can be transformed into the unconstrained one [82]–[86]. Adding the multiplier μ_e to (4.24), the Lagrange function can be built as shown in (4.25).

$$L_e\left(i_{do}, i_{qo}, \mu_e\right) = f_e\left(i_{do}, i_{qo}\right) + \mu_e \cdot h\left(i_{do}, i_{qo}\right) \tag{4.25}$$

Next step is to substitute the parameters and find the critical point (i_{doe}^*, i_{qoe}^*, μ_e^*), which must satisfy (4.26)-(4.28).

$$\left.\frac{\partial L_e\left(i_{do},i_{qo},\mu_e\right)}{\partial i_{do}}\right|_{i_{doe}^*,i_{qoe}^*,\mu_e^*} = d_{de}i_{doe}^* + e_{de}i_{qoe}^* + f_{de} + \mu_e^*\left(2ai_{doe}^* + ci_{qoe}^* + d\right) = 0 \tag{4.26}$$

$$\left.\frac{\partial L_e\left(i_{do},i_{qo},\mu_e\right)}{\partial i_{qo}}\right|_{i_{doe}^*,i_{qoe}^*,\mu_e^*} = d_{qe}i_{doe}^* + e_{qe}i_{qoe}^* + f_{qe} + \mu_e^*\left(2bi_{qoe}^* + ci_{doe}^* + e\right) = 0 \tag{4.27}$$

$$\left.\frac{\partial L_e\left(i_{do},i_{qo},\mu_e\right)}{\partial \mu_e}\right|_{i_{doe}^*,i_{qoe}^*,\mu_e^*} = h\left(i_{doe}^*,i_{qoe}^*\right) = 0 \tag{4.28}$$

where,

$$d_{de} = 3\left(R_s + R_{Inv}\right) + \frac{3\omega_e^2}{R_c}\left(L_d^2 m_d^2 + L_q^2 m_q^2\right);$$

$$e_{de} = \frac{3\omega_e^2}{R_c}\left(L_d^2 m_d n_d + L_q^2 m_q n_q\right);$$

$$f_{de} = \frac{3\omega_e^2}{R_c}\left[\left(L_d k_d + \Lambda_{pm}\right)L_d m_d + L_q^2 k_q m_q\right];$$

$$d_{qe} = \frac{3\omega_e^2}{R_c}\left(L_d^2 m_d n_d + L_q^2 m_q n_q\right);$$

$$e_{qe} = 3\left(R_s + R_{Inv}\right) + \frac{3\omega_e^2}{R_c}\left(L_d^2 n_d^2 + L_q^2 n_q^2\right);$$

$$f_{qe} = \frac{3\omega_e^2}{R_c}\left[\left(L_d k_d + \Lambda_{pm}\right)L_d n_d + L_q^2 k_q n_q\right].$$

The critical point can be the maximum, minimum, or saddle point. Thus, the optimality should be examined. It can be implemented by checking the sign of the determinant of the

bordered Hessian matrix [82] is positive (maximum), negative (minimum) or no sign (saddle point).

$$\left|\begin{array}{ccc} 0 & \dfrac{\partial h\left(i_{do},i_{qo}\right)}{\partial i_{do}} & \dfrac{\partial h\left(i_{do},i_{qo}\right)}{\partial i_{qo}} \\ \dfrac{\partial h\left(i_{do},i_{qo}\right)}{\partial i_{do}} & \dfrac{\partial^2 L_e\left(i_{do},i_{qo},\mu_e\right)}{\partial i_{do}^2} & \dfrac{\partial^2 L_e\left(i_{do},i_{qo},\mu_e\right)}{\partial i_{do}\partial i_{qo}} \\ \dfrac{\partial h\left(i_{do},i_{qo}\right)}{\partial i_{qo}} & \dfrac{\partial^2 L_e\left(i_{do},i_{qo},\mu_e\right)}{\partial i_{qo}\partial i_{do}} & \dfrac{\partial^2 L_e\left(i_{do},i_{qo},\mu_e\right)}{\partial i_{qo}^2} \end{array}\right|_{i_{doe}^*,i_{qoe}^*,\mu_e^*} \tag{4.29}$$

where,

$$\left.\frac{\partial^2 L_e\left(i_{do},i_{qo},\mu_e\right)}{\partial i_{do}^2}\right|_{i_{doe}^*,i_{qoe}^*,\mu_e^*} = d_{de} + 2a\mu_e^*;$$

$$\left.\frac{\partial^2 L_e\left(i_{do},i_{qo},\mu_e\right)}{\partial i_{qo}^2}\right|_{i_{doe}^*,i_{qoe}^*,\mu_e^*} = e_{qe} + 2b\mu_e^*;$$

$$\left.\frac{\partial^2 L_e\left(i_{do},i_{qo},\mu_e\right)}{\partial i_{do}\partial i_{qo}}\right|_{i_{doe}^*,i_{qoe}^*,\mu_e^*} = \left.\frac{\partial^2 L_e\left(i_{do},i_{qo},\mu_e\right)}{\partial i_{qo}\partial i_{do}}\right|_{i_{doe}^*,i_{qoe}^*,\mu_e^*} = e_{de} + c\mu_e^*;$$

$$\left.\frac{\partial h\left(i_{do},i_{qo}\right)}{\partial i_{do}}\right|_{i_{doe}^*,i_{qoe}^*} = 2ai_{doe}^* + ci_{qoe}^* + d;$$

$$\left.\frac{\partial h\left(i_{do},i_{qo}\right)}{\partial i_{qo}}\right|_{i_{doe}^*,i_{qoe}^*} = 2bi_{qoe}^* + ci_{doe}^* + e.$$

4.4.3 Loss Minimization Control in the Flux-Weakening Region

In the flux-weakening region, the current vector can reach the voltage limit boundary. If the optimal operating point is located in the voltage limit ellipse, the optimal current reference can be obtained as illustrated in section 4.4.2. The voltage limit ellipse shrinks as the speed increases. Thus, in FW region the current reference minimizing the losses of IPMSM drives can appear at the intersection of the voltage constraint and the constant torque locus. The analytical optimization model of LMC in FW region is formulated in (4.30).

Minimize

$$\begin{aligned} f_e\left(i_{do}, i_{qo}\right) &= P_{Cu} + P_{Inv} + P_{Fe} \\ &= \frac{3}{2}\left(R_s + R_{Inv}\right)\left(i_{do}^2 + i_{qo}^2\right) + \frac{3\omega_e^2}{2R_c}\left(\Lambda_d^2 + \Lambda_q^2\right) \end{aligned} \tag{4.30}$$

Subject to

$$\begin{cases} g\left(i_{do}, i_{qo}\right) = v_d^2 + v_q^2 - V_{am}^2 \\ \qquad = \left[\left(R_s + R_{Inv}\right) i_{do} - \omega_e \Lambda_q\right]^2 + \left[\left(R_s + R_{Inv}\right) i_{qo} + \omega_e \Lambda_d\right]^2 - V_{am}^2 \\ \qquad = a_g i_{do}^2 + b_g i_{qo}^2 + c_g i_{do} i_{qo} + d_g i_{do} + e_g i_{qo} + f_g \le 0 \\ h\left(i_{do}, i_{qo}\right) = \frac{3}{2} P\left(\Lambda_d i_q - \Lambda_q i_d\right) - \left(T_{fric} + T_o^*\right) = 0 \end{cases}$$

where,

$$a_g = \left(R_s + R_{Inv} - \omega_e L_q m_q\right)^2 + \omega_e^2 L_d^2 m_d^2;$$

$$b_g = \left(R_s + R_{Inv} + \omega_e L_d n_d\right)^2 + \omega_e^2 L_q^2 n_q^2;$$

$$c_g = 2\omega_e\left[\left(R_s + R_{Inv}\right)\left(L_d m_d - L_q n_q\right) + \omega_e\left(m_d n_d L_d^2 + m_q n_q L_q^2\right)\right];$$

$$d_g = 2\omega_e\left[\omega_e L_d m_d\left(L_d k_d + \Lambda_{pm}\right) - L_q k_q\left(R_s + R_{Inv} - \omega_e L_q m_q\right)\right];$$

$$e_g = 2\omega_e\left[\omega_e L_q^2 k_q n_q + \left(L_d k_d + \Lambda_{pm}\right)\left(R_s + R_{Inv} + \omega_e L_d n_d\right)\right];$$

$$f_g = \omega_e^2\left[L_q^2 k_q^2 + \left(L_d k_d + \Lambda_{pm}\right)^2\right] - V_{am}^2.$$

The Lagrange function can be built by adding the multipliers μ_{fw} and λ_{fw} into (4.30), as shown in (4.31).

$$L_{fw}\left(i_{do}, i_{qo}, \lambda, \mu\right) = f_e\left(i_{do}, i_{qo}\right) + \lambda_{fw} \cdot g\left(i_{do}, i_{qo}\right) + \mu_{fw} \cdot h\left(i_{do}, i_{qo}\right) \tag{4.31}$$

At the critical point (i_{dofw}^*, i_{qofw}^*, μ_{fw}^*, λ_{fw}^*), the first-order condition (4.32)-(4.37) must be satisfied.

$$\left.\frac{\partial L_{fw}\left(i_{do}, i_{qo}, \mu_{fw}, \lambda_{fw}\right)}{\partial i_{do}}\right|_{i_{dofw}^*, i_{qofw}^*, \mu_{fw}^*, \lambda_{fw}^*} = d_{de} i_{dofw}^* + e_{de} i_{qofw}^* + f_{de} + \lambda_{fw}^*\left(2a_g i_{dofw}^* + c_g i_{qofw}^* + d_g\right) + \mu_{fw}^*\left(2a i_{dofw}^* + c i_{qofw}^* + d\right) = 0 \tag{4.32}$$

$$\left.\frac{\partial L_{fw}\left(i_{do}, i_{qo}, \mu_{fw}, \lambda_{fw}\right)}{\partial i_{qo}}\right|_{i_{dofw}^*, i_{qofw}^*, \mu_{fw}^*, \lambda_{fw}^*} = d_{qe} i_{dofw}^* + e_{qe} i_{qofw}^* + f_{qe} + \lambda_{fw}^*\left(2b_g i_{qofw}^* + c_g i_{dofw}^* + e_g\right) + \mu_{fw}^*\left(2b i_{qofw}^* + c i_{dofw}^* + e\right) = 0 \tag{4.33}$$

$$\left.\frac{L_{fw}\left(i_{do}, i_{qo}, \mu_{fw}, \lambda_{fw}\right)}{\partial \mu_{fw}}\right|_{i^*_{dofw}, i^*_{qofw}, \mu^*_{fw}, \lambda^*_{fw}} = h\left(i^*_{dofw}, i^*_{qofw}\right) = 0 \tag{4.34}$$

$$\lambda^*_{fw} \cdot g\left(i^*_{dofw}, i^*_{qofw}\right) = 0 \tag{4.35}$$

$$\lambda^*_{fw} \geq 0 \tag{4.36}$$

$$g\left(i^*_{dofw}, i^*_{qofw}\right) \leq 0 \tag{4.37}$$

According to the complimentary slackness in (4.35), either $\lambda_{fw} = 0$ or $g(i_{do}, i_{qo}) = 0$ at the critical point. When $\lambda_{fw} = 0$, the optimal solution is located within the inequality constraint, then the mixed-constraints optimization problem in (4.30) turns into the equality-constrained optimization problem in (4.24). The optimum current reference can be found by adopting the proposed LMC algorithm in section 4.4.2.

When $\lambda_{fw} \neq 0$, $g(i_{do}, i_{qo})$ must be zero. It indicates that the critical point must be located on both equality constraint in (4.34) and $g(i_{dofw}^*, i_{qofw}^*) = 0$. In other words, the optimum current reference vector is on the optimization constraint, where the voltage limit ellipse and the constant torque locus intersect. In this case, (4.32)-(4.34), (4.36), and $g(i_{dofw}^*, i_{qofw}^*) = 0$ must be satisfied at $(i_{dofw}^*, i_{qofw}^*, \mu_{fw}^*, \lambda_{fw}^*)$. Because Kuhn-Tucker first-order condition is only a necessary condition, the optimality needs to be further examined. However, there are two states, i_{do} and i_{qo}, and two equality constraints in this case. The determinant of the bordered Hessian matrix cannot be used to identify if the critical point is a strict local minimum or maximum anymore. The optimality can be checked by the characteristic of IPMSM drives. Firstly, once the speed and torque are set, there are only

two intersections, where the voltage limit ellipse and the constant torque locus meet. These two critical points must be located on both sides of MTPV. Apparently, the one on the right side of MTPV is the appropriate one. Secondly, the total electrical loss can be calculated by using the cost function in (4.30). The optimal operating point can be determined through the loss comparison between these two current references.

4.4.4 Maximum Torque-Per-Voltage Control

MTPV appears at the intersection where the voltage limit ellipse and the constant torque tangentially intersect, aiming at the maximization of the output torque within the voltage constraint at high speed. The optimization model of Maximum-Torque-Per-Voltage control at certain speed is formulated in (4.38).

Maximize

$$f_v\left(i_{do}, i_{qo}\right) = \frac{3}{2} P\left(\Lambda_d i_q - \Lambda_q i_d\right) - T_{fric} \tag{4.38}$$

Subject to

$$\begin{aligned} h_v\left(i_{do}, i_{qo}\right) &= v_d^2 + v_q^2 - V_{am}^2 \\ &= \left[\left(R_s + R_{Inv}\right) i_{do} - \omega_e \Lambda_q\right]^2 + \left[\left(R_s + R_{Inv}\right) i_{qo} + \omega_e \Lambda_d\right]^2 - V_{am}^2 \end{aligned}$$

The corresponding Lagrange function is shown in (4.39).

$$L_v\left(i_{do}, i_{qo}, \mu_v\right) = f_v\left(i_{do}, i_{qo}\right) + \mu_v \cdot h_v\left(i_{do}, i_{qo}\right) \tag{4.39}$$

At the critical point (i_{dov}^*, i_{qov}^*, μ_v^*) (4.40)-(4.42) must be satisfied.

$$\left.\frac{\partial L_v\left(i_{do},i_{qo},\mu_v\right)}{\partial i_{do}}\right|_{i_{dov}^*,i_{qov}^*,\mu_v^*} = 2ai_{dov}^* + ci_{qov}^* + d + \mu_v^*\left(2a_g i_{dov}^* + c_g i_{qov}^* + d_g\right) = 0 \tag{4.40}$$

$$\left.\frac{\partial L_v\left(i_{do},i_{qo},\mu_v\right)}{\partial i_{qo}}\right|_{i_{dov}^*,i_{qov}^*,\mu_v^*} = ci_{dov}^* + 2bi_{qov}^* + e + \mu_v^*\left(2b_g i_{qov}^* + c_g i_{dov}^* + e_g\right) = 0 \tag{4.41}$$

$$\left.\frac{\partial L_v\left(i_{do},i_{qo},\mu_v\right)}{\partial \mu_v}\right|_{i_{dov}^*,i_{qov}^*,\mu_v^*} = h_v\left(i_{dov}^*,i_{qov}^*\right) = 0 \tag{4.42}$$

Again, the determinant of the bordered Hessian matrix at the critical point should be calculated to examine whether the critical point is a local maximum.

$$\left\|\begin{array}{ccc} 0 & \dfrac{\partial h_v\left(i_{do},i_{qo}\right)}{\partial i_{do}} & \dfrac{\partial h_v\left(i_{do},i_{qo}\right)}{\partial i_{qo}} \\ \dfrac{\partial h_v\left(i_{do},i_{qo}\right)}{\partial i_{do}} & \dfrac{\partial^2 L_v\left(i_{do},i_{qo},\mu_v\right)}{\partial i_{do}^2} & \dfrac{\partial^2 L_v\left(i_{do},i_{qo},\mu_v\right)}{\partial i_{do}\partial i_{qo}} \\ \dfrac{\partial h_v\left(i_{do},i_{qo}\right)}{\partial i_{qo}} & \dfrac{\partial^2 L_v\left(i_{do},i_{qo},\mu_v\right)}{\partial i_{qo}\partial i_{do}} & \dfrac{\partial^2 L_v\left(i_{do},i_{qo},\mu_v\right)}{\partial i_{qo}^2} \end{array}\right\|_{i_{dov}^*,i_{qov}^*,\mu_v^*} \tag{4.43}$$

where,

$$\left.\frac{\partial^2 L_v\left(i_{do},i_{qo},\mu_v\right)}{\partial i_{do}^2}\right|_{i_{dov}^*,i_{qov}^*,\mu_v^*} = 2a + 2a_g\mu_v^*;$$

$$\left.\frac{\partial^2 L_v\left(i_{do},i_{qo},\mu_v\right)}{\partial i_{qo}^2}\right|_{i_{dov}^*,i_{qov}^*,\mu_v^*} = 2b + 2b_g\mu_v^*;$$

$$\left.\frac{\partial^2 L_v\left(i_{do},i_{qo},\mu_v\right)}{\partial i_{do}\partial i_{qo}}\right|_{i_{dov}^*,i_{qov}^*,\mu_v^*} = \left.\frac{\partial^2 L_v\left(i_{do},i_{qo},\mu_v\right)}{\partial i_{qo}\partial i_{do}}\right|_{i_{dov}^*,i_{qov}^*,\mu_v^*} = c + c_g\mu_v^*;$$

$$\left.\frac{\partial h_v\left(i_{do},i_{qo}\right)}{\partial i_{do}}\right|_{i_{dov}^*,i_{qov}^*} = 2a_g i_{dov}^* + c_g i_{qov}^* + d_g;$$

$$\left.\frac{\partial h_v\left(i_{do},i_{qo}\right)}{\partial i_{qo}}\right|_{i_{dov}^*,i_{qov}^*} = 2b_g i_{qov}^* + c_g i_{dov}^* + e_g.$$

If the determinant of the bordered Hessian matrix is positive, the critical point (i_{dov}^*, i_{qov}^*, μ_v^*) is a local maximum. MTPV is achieved.

4.4.5 Voltage Limit Ellipse

In i_{dq0} coordinates, the current limit expression in (2.4) always takes effect. The voltage constraint based on the proposed IPMSM drive model with respect to the winding current is expressed in (4.44).

$$\begin{aligned}&\left[\left(R_s+R_{Inv}\right)i_{do}-\omega_e\Lambda_q\right]^2+\left[\left(R_s+R_{Inv}\right)i_{qo}+\omega_e\Lambda_d\right]^2=V_{am}^2\\&\Rightarrow a_g i_{do}^2+c_g i_{do}i_{qo}+b_g i_{qo}^2+d_g i_{do}+e_g i_{qo}+f_g=0\end{aligned} \tag{4.44}$$

The shifted center, rotation angle, major axis, and the minor axis of the distorted voltage limit ellipse are listed in (4.45)-(4.48), respectively.

$$\left(\frac{e_g c_g - 2b_g d_g}{4a_g b_g - c_g^2}, \frac{c_g d_g - 2a_g e_g}{4a_g b_g - c_g^2} \right) \tag{4.45}$$

$$\frac{1}{2}\arctan\left(\frac{c_g}{a_g - b_g} \right) \tag{4.46}$$

$$\sqrt{\frac{2\left(a_g e_g^2 + b_g d_g^2 + c_g^2 f_g - c_g d_g e_g - 4a_g b_g f_g\right)}{\left(c_g^2 - 4a_g b_g\right)\left[\sqrt{\left(a_g - b_g\right)^2 + c_g^2} - \left(a_g + b_g\right)\right]}} \tag{4.47}$$

$$\sqrt{\frac{2\left(a_g e_g^2 + b_g d_g^2 + c_g^2 f_g - c_g d_g e_g - 4a_g b_g f_g\right)}{\left(c_g^2 - 4a_g b_g\right)\left[-\sqrt{\left(a_g - b_g\right)^2 + c_g^2} - \left(a_g + b_g\right)\right]}} \tag{4.48}$$

4.4.6 Simulation Results

The parameters in Table 4.1 are used for simulation.

First of all, the proposed LMC algorithm below base speed is validated. For given torque T_e^* = 200Nm and speed ω_m = 1000rpm, substitute the parameters into (4.26)-(4.28), then the critical point and the Lagrangian multiplier can be obtained at (-214.7545A, 265.2914A, -34.4629). In order to examine the optimality, substitute (i_{doe}^*, i_{qoe}^*, μ_e^*) into (4.29). The determinant of the bordered Hessian matrix is -0.1392. It indicates that the critical point is a local minimum. In Fig. 4.9, the total electrical loss of the IPMSM drive under simulation along the constant torque (200Nm) locus is plotted. The critical point obtained by the first condition of the proposed optimization algorithm

does generate the minimum total electrical loss. The inverter loss, copper loss, and core loss are also drawn in the figure. It can be seen that below base speed, the copper loss is dominant. The core loss decreases as more negative *d*-axis current is injected.

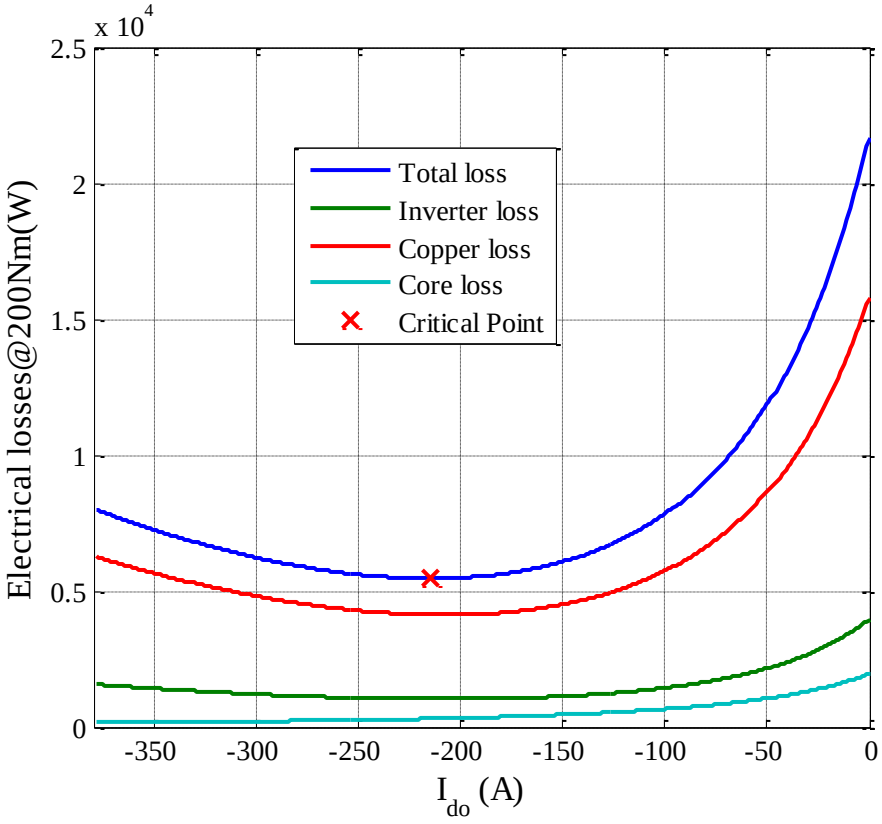

Fig. 4.9. Validation of the proposed LMC algorithm below base speed.

Secondly, the proposed LMC algorithm in the flux-weakening region is tested. At T_e^* = 90Nm and ω_m = 5000rpm, substitute the parameters of the simulated IPMSM drive, such as R_s, R_{Inv}, R_c, Λ_{pm}, L_d, and L_q, into (4.32)-(4.37). As shown in Fig. 4.10(a), two critical points are obtained. The critical points (i_{dofw}^*, i_{qofw}^*, λ_{fw}^*, μ_{fw}^*) are (-195.4252A, 127.5995A, 0.0136, -65.0617) and (-416.929A, 71.4185A, -0.3544, 66.5111). The critical

point 1 shown in Fig. 4.10(a) indicates the optimal current vector. The latter solution can be excluded easily. Firstly, it lies on the left side of MTPV. Secondly, it is located outside of the current limit circle. Thirdly, from the loss-power contours, it can be seen that the total electrical loss at critical point 2 is much bigger than the loss at point 1. Fourthly, the latter solution doesn't satisfy the condition in (4.36) because the Lagrange multiplier of the inequality constraint is negative. It should be noticed that the total loss decreases when smaller *d*-axis current is applied along the constant torque locus@90Nm. It makes sense that the optimal current reference is on the voltage limit ellipse because the current vector cannot be applied outside the constraint. In Fig. 4.10(b), the electrical losses at 5000rpm along constant torque curve@90Nm are shown. Apparently, the core loss takes more proportion at high speed, especially when the negative *d*-axis current is small. The optimum operating point is located on the left of the operating point where the minimum total electrical loss is produced due to the voltage constraint.

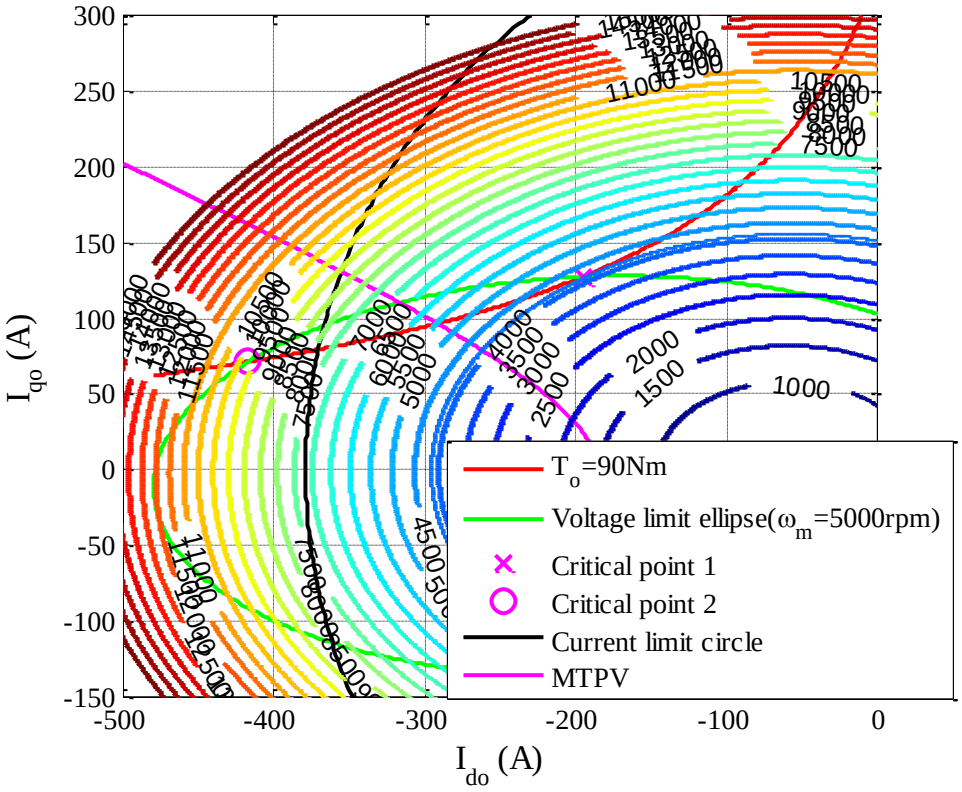
300
250
200
150
100
50
0
-50
-100
-150
-500
-400
-300
-200
-100
0
I_{qo} (A)
I_{do} (A)
T_o=90Nm
Voltage limit ellipse(ω_m=5000rpm)
Critical point 1
Critical point 2
Current limit circle
MTPV

(a)

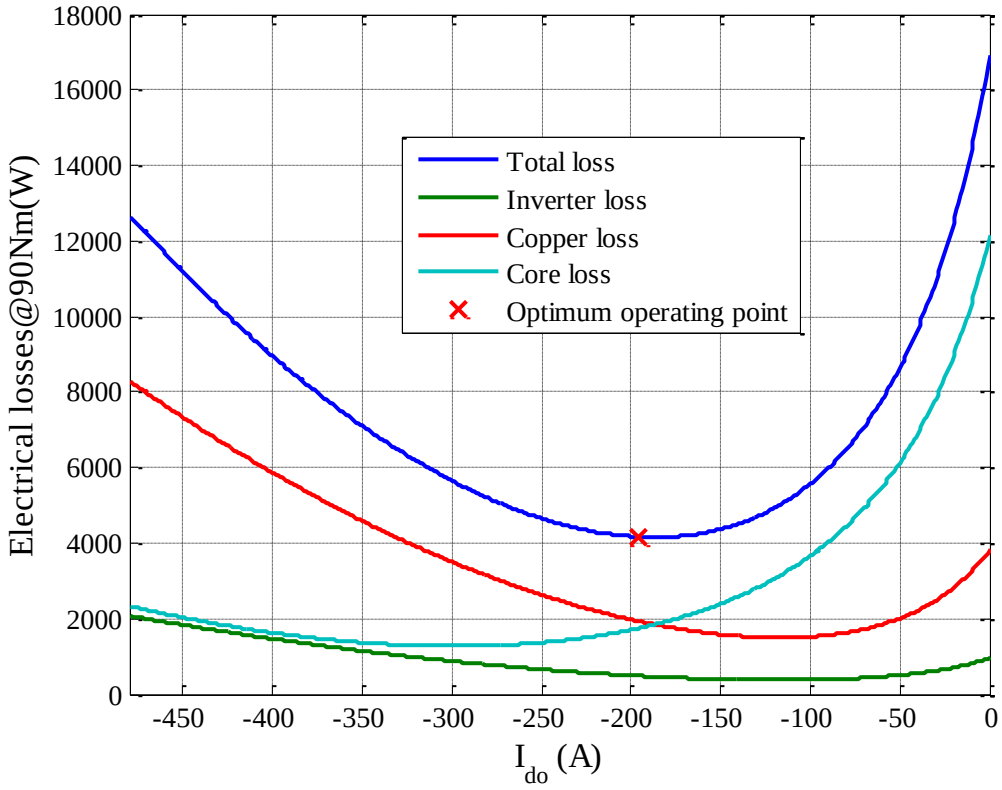

(b)

Fig. 4.10. Validation of the proposed LMC algorithm in FW region. (a) Total loss power contours@5000rpm. (b) Electrical losses along constant torque locus@90Nm.

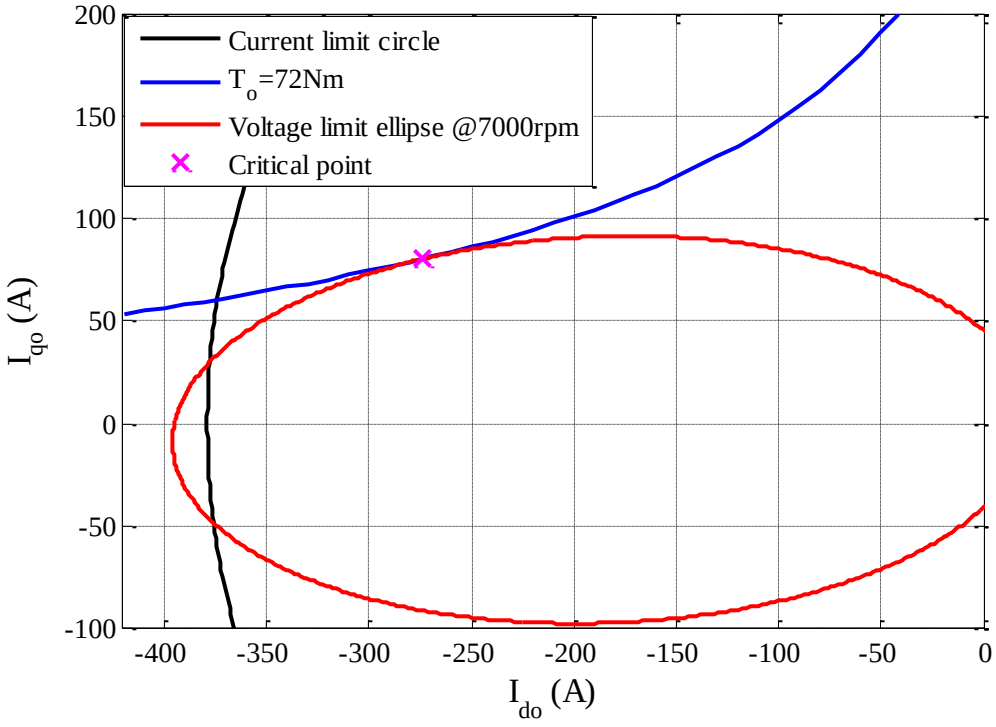

Fig. 4.11. Validation of the proposed MTPV.

Thirdly, the MTPV control based on the proposed IPMSM drive model is validated. At T_o = 72Nm and ω_m = 7000rpm, substitute the parameters into (4.40)-(4.42), then the current reference and the Lagrangian multiplier can be obtained at (-274.2382, 80.3217A, -0.0015). The optimality can be examined by substituting (i_{dov}^*, i_{qov}^*, μ_v^*) into (4.43). The determinant of the bordered Hessian matrix is 1096.6. It indicates the critical point is a local maximum. In other words, along the voltage limit ellipse, the current vector that can generate the maximum torque has been found. As shown in Fig. 4.11 the critical point is located at the intersection, where the constant torque locus (72Nm) and voltage limit ellipse at 7000rpm tangentially intersect.

Fourthly, the influence of the resistance on the voltage limit ellipse is analyzed in the coordinates representing the *d*- and *q*-axis stator-winding current. The influence of the stator-winding and equivalent inverter-loss resistance on the voltage constraint is same with Fig. 4.5(a). As R_s and R_{Inv} increase, the ellipse rotates counterclockwise and shrinks. In Fig. 4.12 it shows the impact of the variation of the core-loss resistance on the voltage limit ellipse. The stator and inverter-loss resistance are set to zero ohm. According to the proposed equivalent circuit, the core-loss resistance decreases the current in the flux-linkage branch. As shown in the flux-linkage equation (4.1), the *d*-axis flux-linkage increases and the *q*-axis flux-linkage decreases as i_{dq} become smaller. The voltage limit ellipse rotates counterclockwise as the core-loss resistance decreases, as shown in Fig. 4.12.

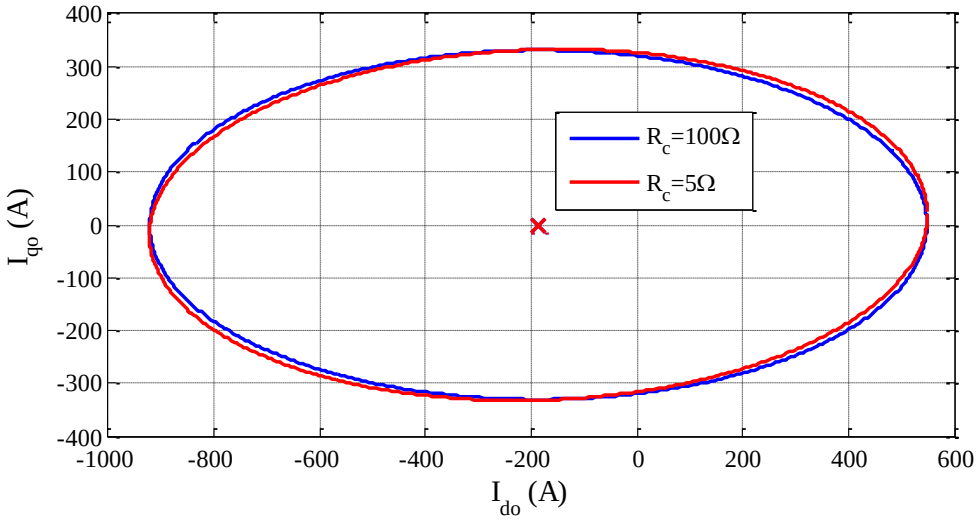

Fig. 4.12. Influence of the core-loss resistance on the voltage constraint in i_{dqo} coordinates.

4.5 Conclusions

In this chapter, a novel model for the IPMSM drives, including the inverter loss, copper loss, and core loss, is proposed. Based on the model, firstly, the analytical solution to the proposed loss-minimization problem is developed with respect to the current contributing to the flux-linkage generation. Compared to MTPA, the proposed LMC is more efficient by considering all the losses in the IPMSM drive system. Secondly, the optimization problem with respect to the winding current is formulated. The loss minimization control algorithm below and above the base speed, and MTPV control based on the proposed model are presented. The influences of the stator-winding, inverter-loss, and core-loss resistance on both of the current limit circle and the voltage limit ellipse are explicitly analyzed in different coordinates. Simulation is implemented to validate the proposed algorithms. However, all the parameters are assumed as constants; all the optimization algorithms and the corresponding analysis can only be used for the IPMSM drives with small nonlinearity, or be applied in the local region.

Chapter 5
High-Accuracy Torque Control with Loss Minimization Considering Nonlinearities in Full-Speed Range

5.1 Introduction

Control accuracy of IPMSM drives is critical to achieving the high performance of the whole system. For example, for automotive applications, such as hybrid EV, the total torque needs to be precisely distributed between the internal combustion engine (ICE) and the electric motors. The torque control error is typically required to be within a few percentages. As a result, automotive companies have been making great efforts in characterizing the motors and calibrate the controllers to meet such stringent requirements. In addition, the high efficiency of the IPMSM drive system is highly desired.

The IPMSM drive model in chapter 4 provides an insight of the accurate modeling. However, this model does not include the nonlinearity of motor parameters, limiting its practical significance in the high-performance IPMSM drive system. On one hand, the feasible operating region can be distorted when the parameters vary within a large range. In this case, the optimized current commands with constant parameters can be located

outside of the actual voltage constraint, and thus the feedback regulator can be saturated. On the other hand, the parameters' nonlinearities lead to inaccurate torque control.

First of all, the saturation and cross-coupling effects [30], [58], [59] on the flux-linkage profiles should be considered. In [87] the *d*- and *q*-axis inductances are built as the function of *d*- and *q*-axis currents. The permanent flux-linkage is regarded as the function of *q*-axis current. In [88], [89] the inductances are fitted with polynomial approximations. However, these methods are not the direct ways to study the machine because from the measured data only the flux-linkage profiles can be obtained, not the inductances.

Moreover, the inverter loss is not considered [19], [26]–[28], [75], [79], [89]–[93] when the flux-linkage is studied. The voltage applied to IPMSM is lower than the desired output voltage due to the voltage drop on the inverter. Thus, the estimated flux-linkage profiles are inaccurate. In this case, due to the dependency of the flux-linkage, the estimated torque and operating constraint may not be precise.

In [19], [26]–[28], [90], [91], the iron loss is taken into account. However, only a constant value for the equivalent core-loss resistance is applied in the proposed control schemes. The flux generated by both current and permanent-magnet flux-linkage affects the formation of the iron loss. The core loss is considered as the function of the current and the speed [36]–[43], [79], [94]. In [25], [36]–[38], [78], [79], [94]–[96], the core loss is formulated as a polynomial of the flux density/flux-linkage with the fundamental frequency. In [39], [40], [42], [43], not only the harmonics but also the parameters of the machine itself, such as the permeability, the material mass density and the thickness of the laminations, are considered to estimate the iron loss.

In order to develop the most efficient control scheme for IPMSM drive system, lots of studies have been done by the researchers. In [25]–[28], [96], the loss model of the machine is adopted and the optimal current references are calculated based on the model. However, the variation of the parameters is neglected, which is limiting the accuracy of the optimal current reference. For example, when the saturation effect is regarded, the MTPA locus runs towards the *d*-axis [97]; the voltage ellipse is shifted and rotated when the stator resistance is included [68]; MTPV curve would be influenced as well because both the constant torque locus and the voltage constraint are distorted.

Thus, if the parameters' profiles with respect to current and speed can be obtained in advance, the model-based algorithm can offer the optimal command under the given torque and speed with high accuracy. Preliminary research work was conducted to include part of parameter nonlinearity in the models. In [56], the authors considered saturation effect of the inductance, but ignored the iron loss. In [88], [98], the core loss is included in the algorithm, but simply fitted by some constant coefficients. In [43], all the nonlinearities of IPMSM are considered, but the FEA results cannot precisely describe the machine's behavior, especially the core loss.

In this chapter, a comprehensive investigation on the nonlinearities in the IPMSM drive system is conducted, including the flux-linkage profiles, inverter loss and core loss at different current and speed. The detailed procedure to characterize the parameters is proposed. The back-fitting based method to accurately estimate the output torque without manufacturing the dummy rotor is presented. The influence of the nonlinearities of the motor drive on the voltage constraint is analyzed. The torque control scheme is designed,

aiming at high-accuracy torque control, fast dynamic response, and high-efficiency performance. The proposed methodologies are validated by the experimental results.

5.2 Conventional IPMSM Modeling Based on the Nonlinear Flux-Linkage Profiles

5.2.1 Flux-Linkage Characterization

Due to saturation and cross-coupling effects on the IPMSMs' flux-linkage profiles shown in Fig. 2.3, inductances L_d, L_q, and Λ_{pm} in equation (2.1) are functions of the *d*- and *q*-axis current.

The flux-linkage information can be obtained from FEA simulation. However, the real machine's characteristics might not be the same as the designed due to the deviation between the manufacture and the machine design. The flux-linkage can be calculated by using the voltage information through experiment, as shown in (3.9) and (3.10). The experiments are supposed to be implemented below the base speed so that all the operating points within the current limit circle can be contained. The *d*- and *q*-axis current and voltage signals should be collected when the motor runs in steady-state.

5.2.2 Torque Estimation with No-load Torque Compensation

Based on the conventional IPMSM modeling, one way to estimate the output torque is using the nonlinear flux-linkage profiles identified below base speed and the no-load torque [44]. Compared to the electromagnetic torque equation in (2.3), the no-load torque is compensated in (5.1) for estimation.

$$T_{est} = \frac{3}{2} P\left(\Lambda_d i_{qo} - \Lambda_q i_{do}\right) - T_{no-load} \tag{5.1}$$

The no-load torque can be measured at different speeds. Furthermore, the curve-fitting technique can be used to characterize the trend of the torque vs. mechanical speed. The measured no-load torque of the IPMSM drive system under test and the fitted curve are plotted in Fig. 5.1. A simple second-order polynomial is good enough for characterization.

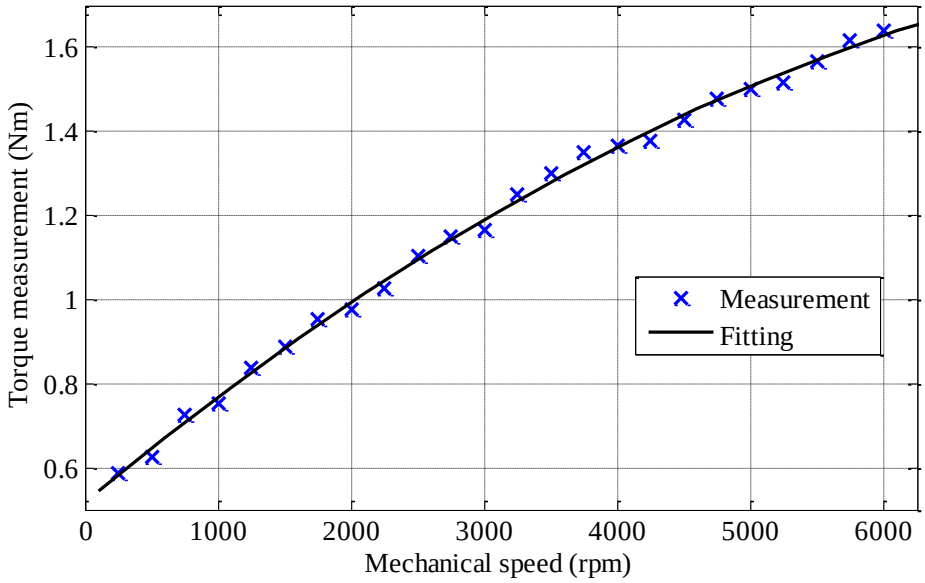

Fig. 5.1. No-load torque measurement of the IPMSM drive system under test.

In this way, the saturation and cross-coupling effects on the flux-linkage profiles are considered and the compensation to the friction on the output torque is made. However, the no-load torque cannot be considered as only the friction torque. The flux-linkage produced by the permanent magnet still generates iron loss in the motor's stator without current injection. The mechanical loss should be separated from the iron loss by measuring the torque with an unmagnetized dummy rotor, which has the same dimension as the IPM machine's rotor does. Furthermore, the no-load torque is only a constant at fixed speed. Thus, it cannot depict the influence of the core loss with different current injections on the output torque.

5.3 Proposed IPMSM Drive Modeling with All Nonlinearities Considered

5.3.1 Nonlinearities of the Losses

The windings in the stator lead to the copper loss. In this research, the stator resistance is considered as a constant. The AC loss due to the eddy current in the coils and the impact of the temperature on the copper loss are not included. In an IPMSM drive system, the temperature sensors are not a common option because of the high cost and difficulty of installation. Thus, the copper loss is assumed to be the function of the RMS current in the windings.

The core loss of an IPMSM consists of hysteresis loss, eddy current loss and excessive loss [32]–[35], [99]. In general, the iron loss is the function of speed and flux-linkage [39], [100]. Because of the existence of the harmonics, the iron loss can be expressed as shown in (5.2) [34].

$$P_{Fe} = \sum_{i=1,3,4,\ldots}^{\infty} \left(k_h i \Lambda_{mi}^2 \omega_e + k_e i^{1.5} \Lambda_{mi}^{1.5} \omega_e^{1.5} + k_c i^2 \Lambda_{mi}^2 \omega_e^2 \right) \tag{5.2}$$

where, k_h, k_e and k_c are the coefficients of the hysteresis loss, excessive loss, and eddy current loss, respectively. i is the order of the harmonics.

The inverter loss P_{Inv} has two components, which are conduction loss and switching loss [101]–[103]. The resistances of the semiconductors are not ideal 0Ω, causing the conduction loss in the inverter [104]. The transient non-zero voltage and current result in the turn-on and turn-off energy losses [105]. The conduction loss and switching loss of the IGBT and diode are shown in the general form in (5.3)-(5.6).

$$P_{IGBT\_conduction} = \frac{1}{T} \int_0^T v_{ce}(t) \cdot i_c(t) dt \tag{5.3}$$

$$P_{diode\_conduction} = \frac{1}{T} \int_0^T v_f(t) \cdot i_f(t) dt \tag{5.4}$$

$$P_{IGBT\_switching} = \frac{1}{T} \sum_{i=1}^{Tf_{sw}} \left[E_{onQ}(t_{ri}) + E_{offQ}(t_{fi}) \right] \tag{5.5}$$

$$P_{diode\_switching} = \frac{1}{T} \sum_{i=1}^{Tf_{sw}} E_{onD}(t_{rri}) \tag{5.6}$$

where, $v_{ce}(t)$, $v_f(t)$, $i_c(t)$, and $i_f(t)$ are the conduction voltages and currents of IGBT and diode, respectively; T is the period of the modulation waveform; f_{sw} is the switching frequency; $E_{onQ}(t_{ri})$ and $E_{offQ}(t_{fi})$ are the IGBT's turn-on and turn-off losses at the current rise-time t_{ri} and fall-time t_{fi}, respectively; $E_{onD}(t_{rri})$ is the diode's turn-on loss at reverse recovery time t_{rri}; the switch-off loss in the diode is normally neglected ($E_{offD} \approx 0$). In summary, the inverter loss is a function of current, voltage, switching frequency, power factor, and modulation index.

The mechanical loss results from the friction and windage. The researchers usually formulate the loss as the function of mechanical speed, such as a second-order or third-order polynomial. It cannot be controlled by electrical signals.

5.3.2 Parameter Characterization

Because of the nonlinearities in the IPMSM drive system, the parameters in the proposed equivalent circuit in Fig. 4.2 should be characterized. Under certain DC bus voltage, the flux-linkage profiles, the equivalent inverter-loss, and core-loss resistance are the nonlinear functions of the rotating speed, the *d*- and *q*-axis current of the IPMSM. Thus, the parameters' characterization is to build the relationship between the arguments and dependent variables.

The inverter loss can be obtained by estimation or use of the power analyzer, which is the difference between the electrical input power and the inverter's output power. The loss profile can be used for the compensation to the flux-linkage calculation. In the

experiment, once the voltage and current commands are recorded at a certain speed, the *d*- and *q*-axis flux-linkage can be identified.

It is complicated to acquire the core loss in the IPMSM drive system. First of all, the mathematical model in (5.2) is not accurate. In FEA simulation the IPMSM is injected with pure sinusoidal waveform, but the IPMSMs are usually driven by VSI in practice. Besides, there must be some difference between the permanent magnet used in FEA software and the one used in the tested prototype. The FEA result of the core loss of a 12kW IPM motor is shown in Fig. 5.2(a). Fig. 5.2(b) shows the measurement of the sum of the core loss and mechanical loss of the IPM machine at 2400rpm. When the machine's rotating speed is fixed, the mechanical loss is invariant. The trend of the measured losses can be regarded as the variation of the iron loss with respect to the current. Compared to the core loss simulated in Fig. 5.2(a), the trend and the magnitude of the measured one in Fig. 5.2(b) are obviously different.

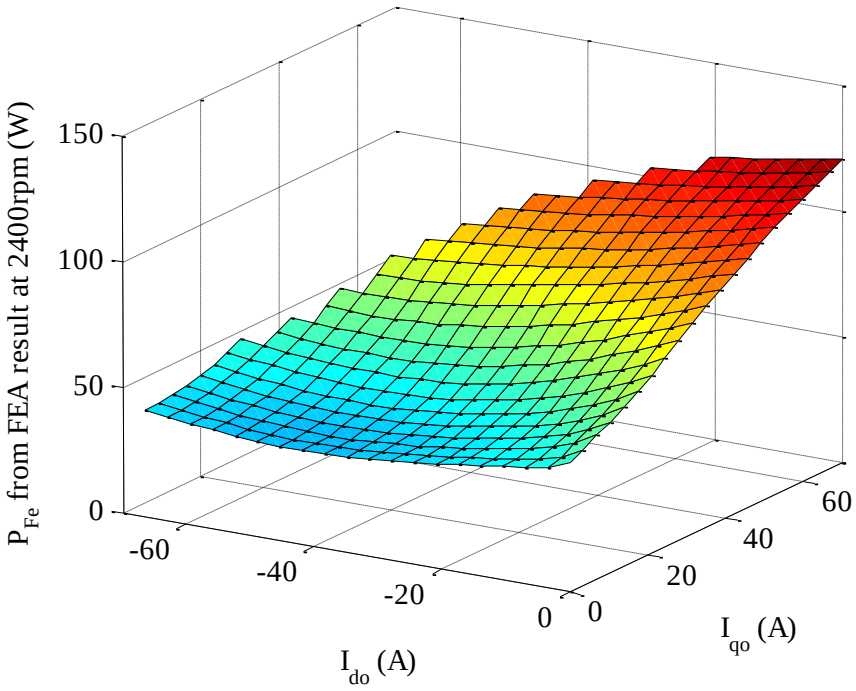
150
100
50
0
P_{Fe} from FEA result at 2400rpm (W)
-60
-40
-20
0
I_{do} (A)
0
20
40
60
I_{qo} (A)

(a)

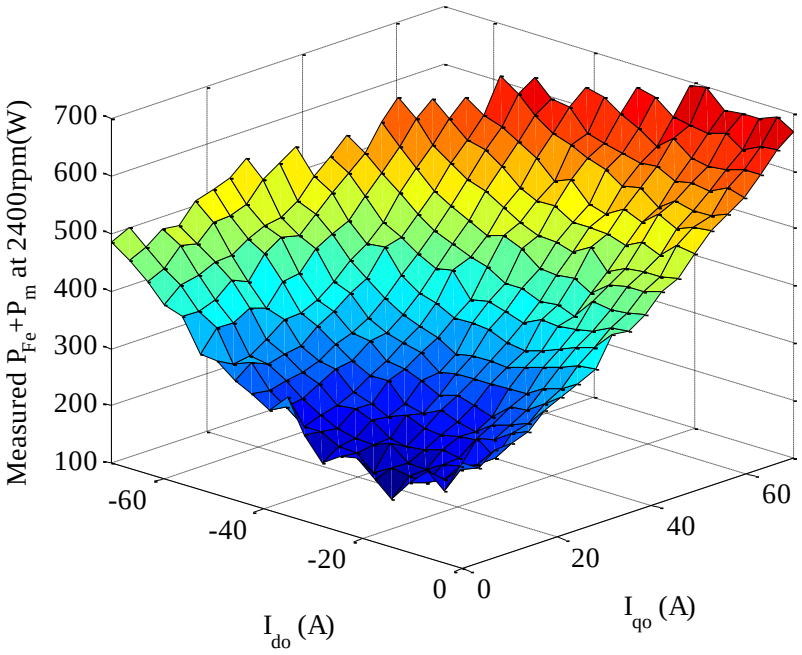

(b)

Fig. 5.2. Losses of an IPMSM at 2400rpm. (a) FEA simulation result of core loss. (b) The sum of the core loss and mechanical loss.

Secondly, it is difficult to separate the core loss from the mechanical loss. The core loss of the IPMSMs mainly exists in the stator because of the rotating flux field. If the negative *d*-axis current is applied, the *d*-axis flux-linkage decreases. At a fixed speed without any load, if no *q*-axis current is applied and the *d*-axis flux-linkage is adjusted to be zero, the loss on the shaft is only the friction loss [45], [46]. However, this doesn't work unless only the fundamental component of the flux-linkage exists in the machine. Due to the geometry of the machine, harmonics can be generated when *d*-axis current is

applied. They produce extra iron loss. As a result, the measured loss is always larger than the mechanical loss when 0A *q*-axis current and negative *d*-axis current are applied.

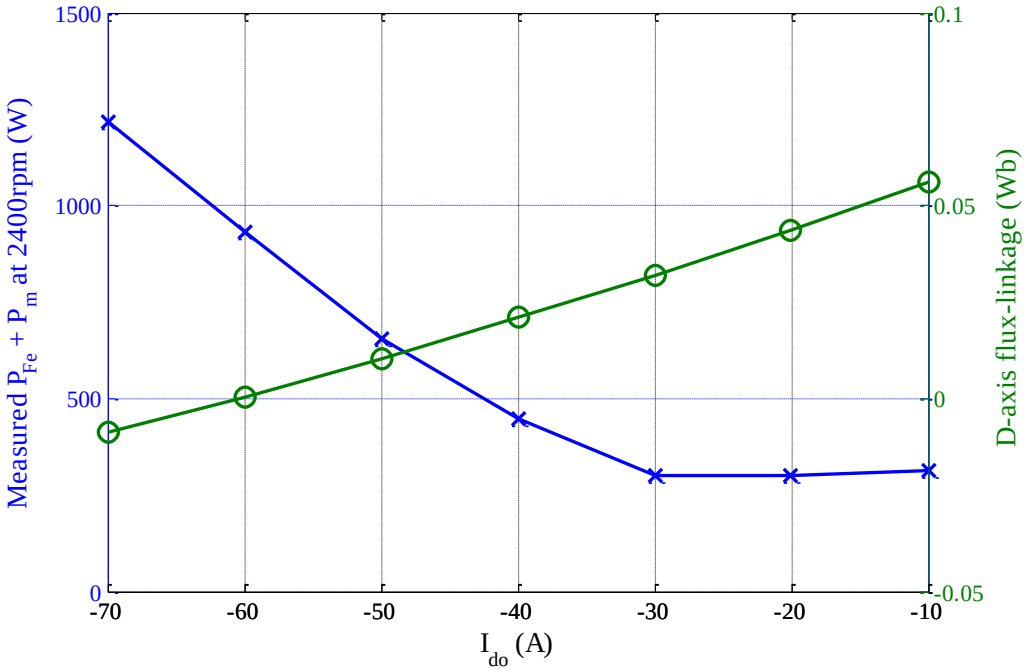

Fig. 5.3. Measured P_{Fe} + P_m and *d*-axis flux-linkage@2400rpm vs. *d*-axis current.

In Fig. 5.3 this phenomenon is well explained. In the figure, it shows at 2400rpm the measured core loss plus mechanical loss of the IPMSM under test with respect to the *d*-axis current. The *q*-axis current is controlled at zero ampere. The *d*-axis flux-linkage is also plotted. Because under certain speed the mechanical loss is invariant, the trend of the sum of the losses can be regarded as the variation of the iron loss with respect to the current. Apparently, the loss is not minimum when the *d*-axis flux-linkage is zero. The

injected *d*-axis current generates lots of harmonics especially when the amplitude of the current is high. The harmonics bring more core loss to the machine. Thus, the mechanical loss cannot be separated from the core loss by setting the flux-linkage to be zero. This is because at that point the core loss still exists.

The most convincing way to obtain the mechanical loss is to make a dummy rotor for the IPMSM. Then the iron loss is obtained by using the inverter output power subtracting the sum of the copper loss, friction loss, and mechanical output power.

Here is the process of the parameters' characterization for an IPMSM at a certain operating point.

1) Calculate the inverter loss. The inverter loss can be obtained by using a power analyzer and it can be calculated as shown in (5.7). The inverter loss also can be estimated according to current, voltage, modulation index, power factor, and switching frequency [106].

$$P_{Inv} = \frac{3}{2}\left(v_d i_{do} + v_q i_{qo}\right) - P_{inv-output-measured} \tag{5.7}$$

where, $P_{inv\text{-}output\text{-}measured}$ is the measured inverter output power.

2) Calculate the equivalent inverter-loss resistance in the proposed equivalent circuit in Fig. 4.2.

$$R_{Inv} = \frac{2P_{Inv}}{3\left(i_{do}^2 + i_{qo}^2\right)} \tag{5.8}$$

3) The flux-linkage profiles can be established upon the voltage command and the current reference.

$$\Lambda_d = \frac{v_q - \left(R_s + R_{Inv}\right) i_{qo}}{\omega_e} \tag{5.9}$$

$$\Lambda_q = \frac{\left(R_s + R_{Inv}\right) i_{do} - v_d}{\omega_e} \tag{5.10}$$

4) Calculate core loss.

$$P_{Fe} = P_{inv-output-measured} - \frac{3}{2} R_s \left(i_{do}^2 + i_{qo}^2\right) - P_m - T_o \omega_m \tag{5.11}$$

5) Calculate the equivalent core-loss resistance.

$$R_c = \frac{3\omega_e^2 \left(\Lambda_d^2 + \Lambda_q^2\right)}{2P_{Fe}} \tag{5.12}$$

5.3.3 Back-Fitting Based Torque Estimation Technique

As stated previously, all the information of the nonlinear parameters of the machine is required during the process of modeling, including the flux-linkage profiles, the mechanical loss, the equivalent inverter-loss and core-loss resistance. Each of them can be obtained through experiments, which involve both electrical and mechanical operations. Equation (4.10) can be used to calculate the torque on the shaft with the separation of the core loss and mechanical loss. Under fixed speed the friction and windage loss power is invariant. Thus, if the iron loss and mechanical loss can be

regarded as a whole when the motor spins continually, it is not necessary to manufacture the dummy rotor. Here is the proposed algorithm to calculate the output torque.

The characterization of the equivalent inverter-loss resistance and the flux-linkage profiles is the same as illustrated in section 5.3.2. It is irrelevant to R_c according to the structure of the equivalent circuit shown in Fig. 4.2. The core loss and mechanical loss are considered as one variable. As consequence the torque equation in (4.10) can be rewritten and a new torque formula is derived as shown below.

$$\begin{aligned} T_o^* &= \frac{3}{2}P\left(\Lambda_d i_q - \Lambda_q i_d\right) - T_{fric} \\ &= \frac{3}{2}P\left[\Lambda_d\left(i_{qo} - \frac{\omega_e \Lambda_d}{R_c}\right) - \Lambda_q\left(i_{do} + \frac{\omega_e \Lambda_q}{R_c}\right)\right] - T_{fric} \\ &= \frac{3}{2}P\left(\Lambda_d i_{qo} - \Lambda_q i_{do}\right) - \frac{\frac{3}{2}\cdot\frac{\omega_e^2\left(\Lambda_d^2 + \Lambda_q^2\right)}{R_c} + T_{fric}\omega_m}{\omega_m} \\ &= \frac{3}{2}P\left[\left(\Lambda_d i_{q0} - \Lambda_q i_{d0}\right)\right] - T_{Fe+fric} \end{aligned} \tag{5.13}$$

where,

$$T_{Fe+fric} = \frac{P_{inv-output-measured} - \frac{3}{2}R_s\left(i_{do}^2 + i_{qo}^2\right) - T_o\omega_m}{\omega_m} \tag{5.14}$$

$T_{Fe+fric}$ represents the loss torque caused by both of the iron loss and the mechanical loss. It is the function of the *d*- and *q*-axis currents, and the motor's speed. $T_{Fe+fric}$ is proportional to the difference between the inverter output power and the summation of

the copper loss and the mechanical output power at certain speed. Torque equation (5.13) is independent of the separation between the core loss and mechanical loss, thus enabling the torque to be estimated without manufacturing the dummy rotor.

5.4 IPMSM Drive Modeling Based on Proposed Model with Speed-Independent Parameters

5.4.1 Experiment-Based Method for Parameter Characterization

In this section, the inverter loss, the core loss, and the flux-linkage profiles are assumed to be invariant at different speeds. Here proposes an experiment-based method to build the LUTs for the nonlinearities. 3D LUTs for the parameters can be established. Their inputs are the *d*- and *q*-axis current.

The experiments can be implemented at one fixed speed. In order to cover the entire operating plane within the current limit circle, the operating speed should be chosen below base speed. The diagram of the experimental setup is shown in Fig. 5.4. The IPM machine under test is coupled with the dynamometer (dyno). The logged data includes the *d*- and *q*-axis voltage and current commands, DC voltage, DC current, the inverter output power, the torque on the shaft, and the mechanical speed. If the power analyzer is not available, the calculation of R_{Inv} can be implemented by using the estimated inverter loss.

The no-load torque is measured and compensated as the friction torque at different speeds.

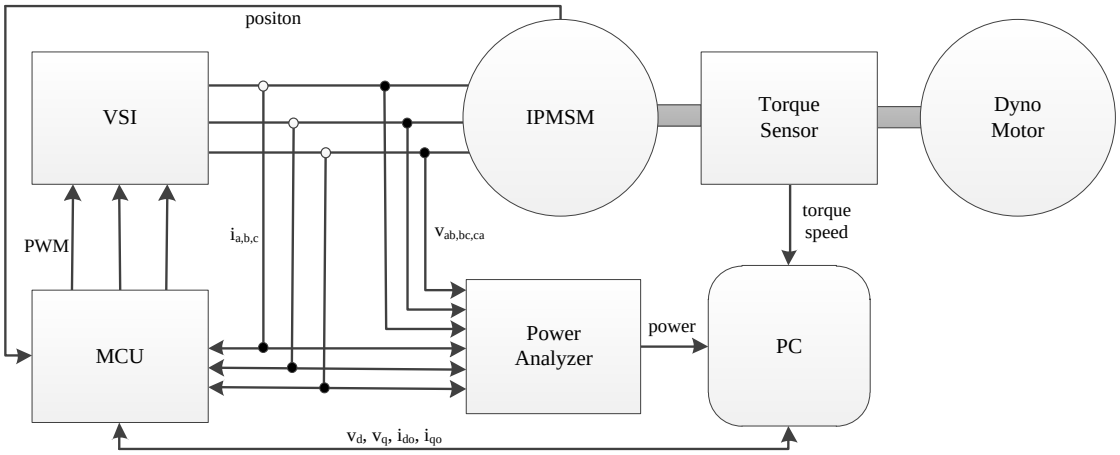

Fig. 5.4. Diagram of the experimental system.

The accuracy of the voltage estimation affects the precision of the estimation of the flux-linkage profiles. In order to decrease the error between the actual voltage and the voltage reference, the voltage references are sampled and filtered by the low-pass filters (LPF). The timing of sampling the current and updating PWM is different. Thus, the time delay between the voltage command and the output voltage should be taken into account. The actual applied voltage can be obtained by rotating the voltage reference as shown in (5.15).

$$\begin{bmatrix} v_d \\ v_q \end{bmatrix} = \begin{bmatrix} \cos\theta_d & \sin\theta_d \\ -\sin\theta_d & \cos\theta_d \end{bmatrix} \begin{bmatrix} v_d^{'} \\ v_q^{'} \end{bmatrix} \tag{5.15}$$

where, $v_d^{'}$ and $v_q^{'}$ are the *d*- and *q*-axis filtered voltage commands; v_d and v_q are the *d*- and *q*-axis voltage output of the controller with phase-shift compensation; θ_d is the rotation angle and its value is ω_e / f_{sw}.

The characterized parameters of the device under test (DUT) at 2400rpm are shown in Fig. 5.5. It can be seen that the equivalent inverter-loss resistance decreases as the current increases. The saturation and cross-coupling effects on the flux-linkage profiles are reflected in Fig. 5.5(b) and Fig. 5.5(c). In Fig. 5.5(d) it shows the variation of the loss torque with respect to the current. More *q*-axis current generates bigger *q*-axis flux-linkage, which generates more loss. The increasing loss torque can be observed with increasing *q*-axis current in the figure. The negative *d*-axis current injection is supposed to decrease the *d*-axis flux-linkage. In fact, the loss is decreased when the negative *d*-axis current is small. However, the loss increases as the *d*-axis current increases due to the harmonics. Thus, $T_{Fe+fric}$ firstly decreases then increases, as the negative *d*-axis current increases.

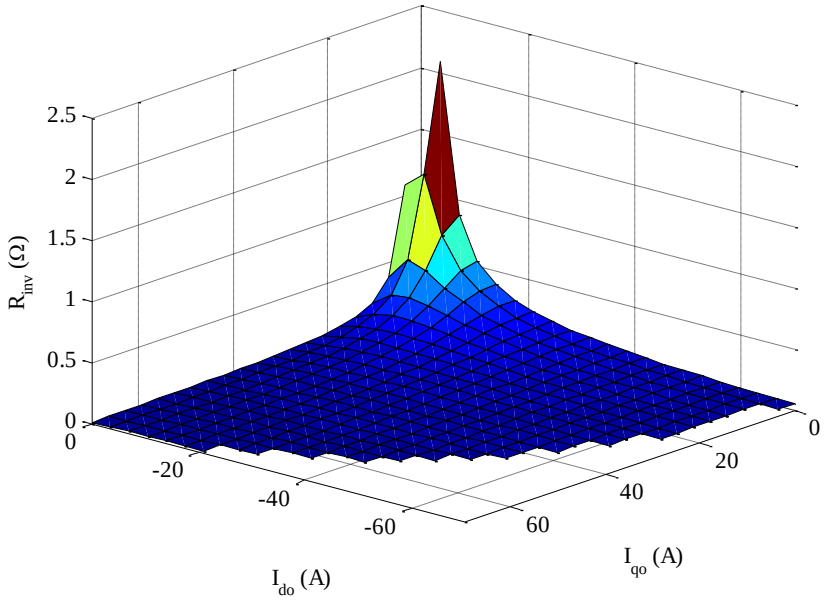
2.5
2
1.5
1
0.5
0
R_{inv} (Ω)
0
-20
-40
-60
I_{do} (A)
0
20
40
60
I_{qo} (A)

(a)

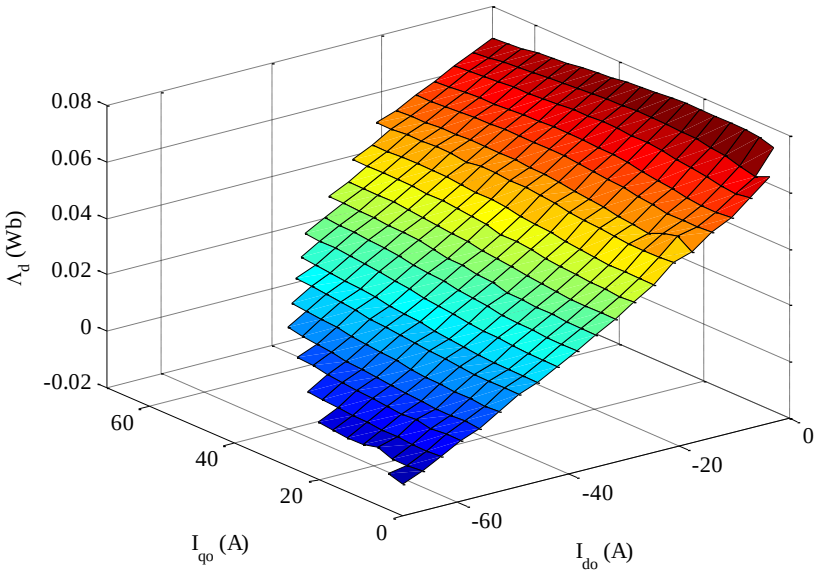
0.08
0.06
0.04
0.02
0
-0.02
Λ_d (Wb)
60
40
20
0
I_{qo} (A)
0
-20
-40
-60
I_{do} (A)

(b)

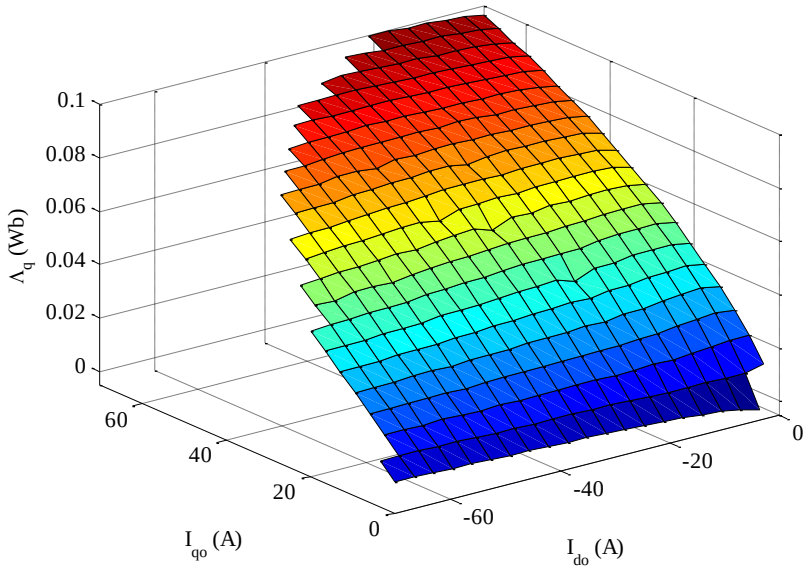

(c)

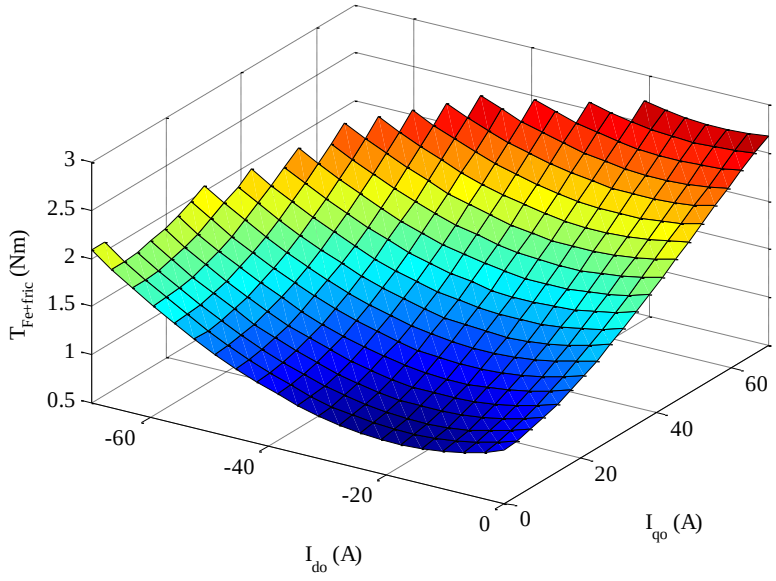

(d)

Fig. 5.5. Parameters' characterization of the IPMSM drive under test @2400rpm. (a) Equivalent inverter-loss resistance. (b) *d*-axis flux-linkage. (c) *q*-axis flux-linkage. (d) Loss torque $T_{Fe+fric}$.

5.4.2 Comparison of Voltage Constraint and Constant Torque locus Based on Different Models

The voltage limit ellipse encircles the operating area where the IPM machine can run at high speed. It is important to know where the limitation is. Based on the conventional IPMSM model, the voltage constraint can be obtained by substituting the flux-linkage

information into equation (2.2). The estimated voltage limit ellipses are plotted in black in Fig. 5.6.

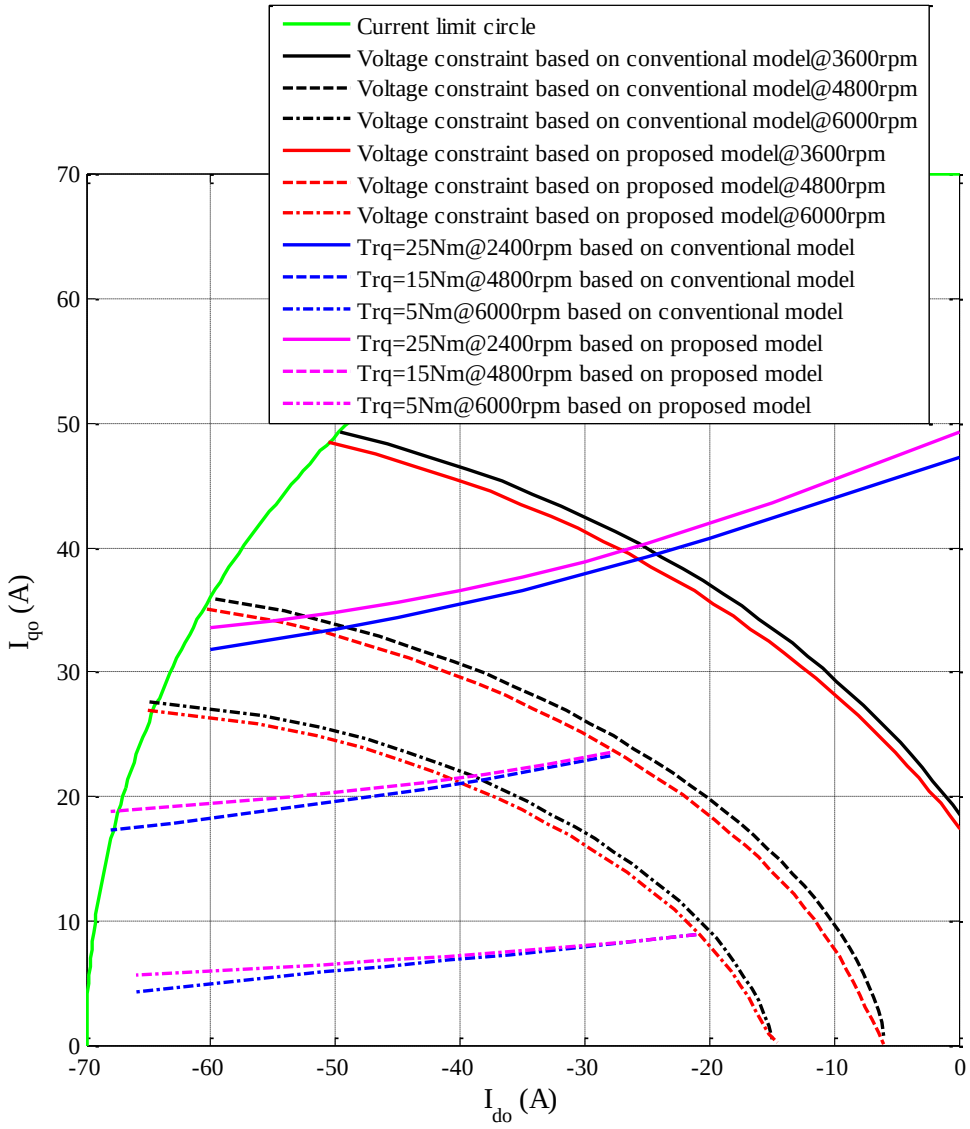

Fig. 5.6. Voltage constraints and constant torque loci based on different IPMSM models.

However, the voltage drop across the inverter is not included in the conventional model. With the mapping of the inverter-loss resistance in (5.8), the estimated voltage

limit ellipses based on the proposed model in (4.2) are plotted in red in Fig. 5.6. It can be seen that when the inverter loss is taken into account the voltage constraint shrinks. The EMF voltage accounts for more proportion in the voltage equation at higher speed. Thus, the gap between the red curves and the black ones decreases as the speed increases. It is not appropriate that a larger operating region is exploited. For given DC bus voltage and speed, the current reference outside the actual voltage limit ellipse can be generated based on the conventional model. The controller regulates the output to eliminate the error between the command and the feedback signal, but the operating point cannot be reached in this case. Thus, the oscillation of the control can occur in transient mode, and the current feedback controller can be saturated. In other words, the current is out of control.

The blue curves are the constant torque loci based on the conventional IPMSM model in Fig. 5.6. The constant torque curves based on the proposed model are plotted in pink. Compared to (5.1), torque equation (5.13) includes the core loss. Thus, in order to generate the same output torque, the current reference based on the proposed model is bigger than the one based on the conventional model. The gap between two kinds of constant torque loci based on different models is dependent on the core loss. It increases as the *d*- and *q*-axis current increase.

5.5 Torque Control System Design with Loss Minimization Based on Speed-Dependent Parameters

5.5.1 Speed-Dependent Parameters

In the previous section, the parameters are characterized at only one fixed speed. However, the nonlinear losses are dependent on both the current and speed. For example, when the motor operates at certain DC bus voltage, switching frequency, and load, the inverter loss is related to the modulation index and power factor. In other words, with the same *d*- and *q*-axis current injection, the equivalent inverter-loss resistance varies at different operating speeds. For another example, the core loss increases as the electrical frequency increases.

In Fig. 5.7, the characterized equivalent inverter-loss resistance and the loss torque are plotted at different speeds. It can be seen that R_{Inv} can increase or decrease with the same current when the speed increases. The loss torque grows larger as the mechanical speed increases.

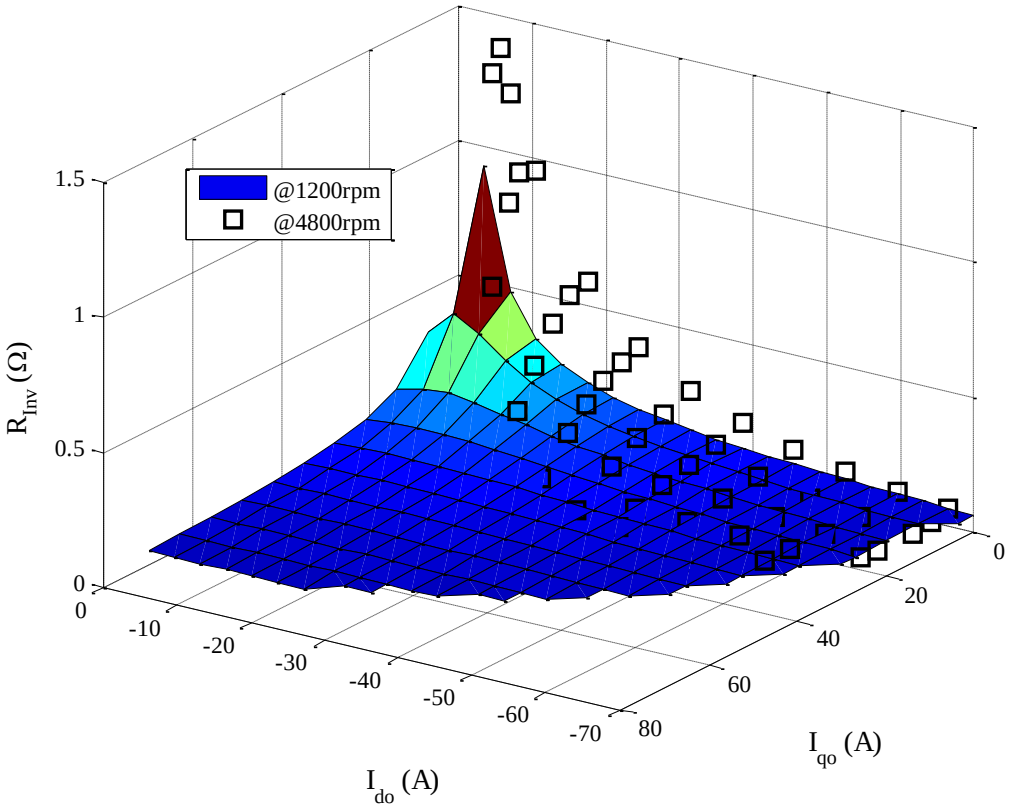
@1200rpm
@4800rpm
1.5
1
0.5
0
R_{Inv} (Ω)
0
-10
-20
-30
-40
-50
-60
-70
I_{do} (A)
0
20
40
60
80
I_{qo} (A)

(a)

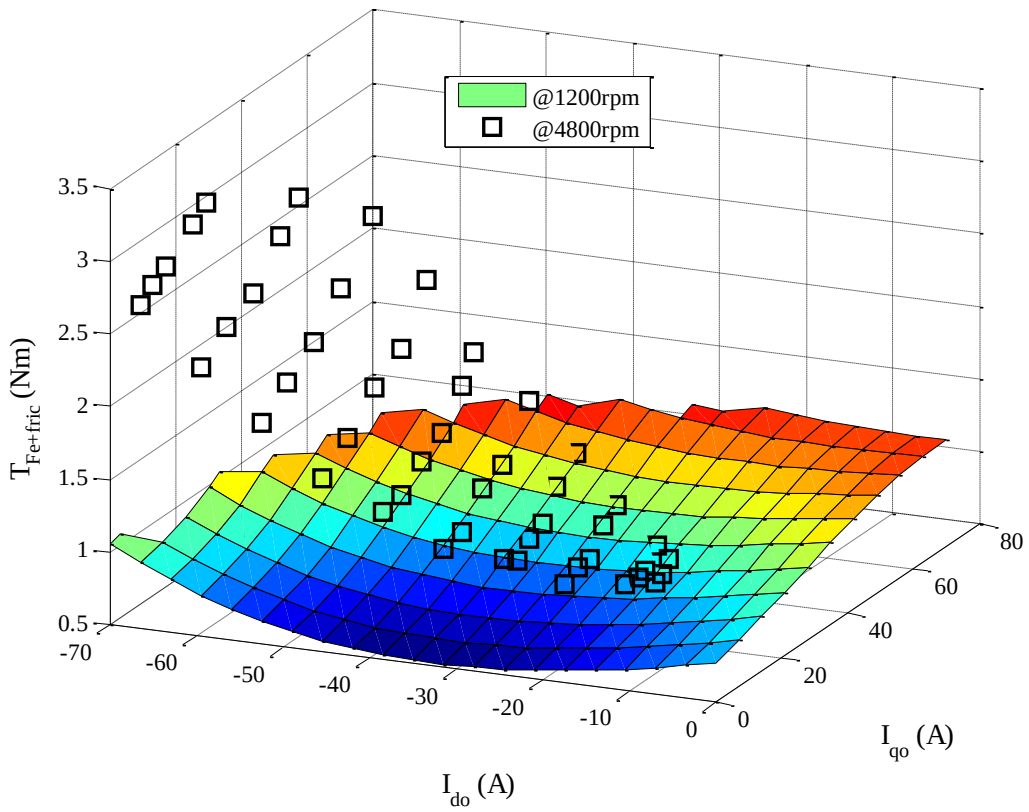

(b)

Fig. 5.7. Nonlinear parameters at different speeds. (a) Equivalent inverter-loss resistance. (b) Equivalent loss torque $T_{Fe+fric}$.

Due to the magnetizing saturation and the core loss, the flux-linkage profiles also vary at different speeds. In order to precisely describe the behavior of the IPMSM drive, 4D LUTs with respect to i_{do}, i_{qo}, and ω_e for R_{Inv} in (5.8), $T_{Fe+fric}$ in (5.14), Λ_d in (5.9), and Λ_q in (5.10) should be established. The approach for characterization is same as illustrated in section 5.4.1, but the experiments should be implemented at different speeds. Below base

speed, the operating points in the tables should mesh within the current limit circle. Above the base speed, the experiments should be done carefully within both current and voltage constraints.

In Fig. 5.8, the estimated voltage limit ellipses based on the proposed model with 4D parameter LUTs are plotted in red. The black curves are drawn by using the measured output voltage of the current controller. The ellipses in different colors almost coincide at 3600rpm, 4800rpm and 6000rpm. In other words, for given current command at certain speed, the voltage equation (4.2) with characterized parameters can provide precise voltage reference for the IPMSM control. If it is used for the current feedforward control, the burden of the current feedback regulator can be significantly reduced, and the dynamic performance can be improved.

In Fig. 5.8, the constant torque loci based on the proposed model with 4D LUTs are plotted in pink. They match the measurement. Thus, if the torque equation (5.13) with characterized parameters is applied for estimation, the high-accuracy torque control can be achieved.

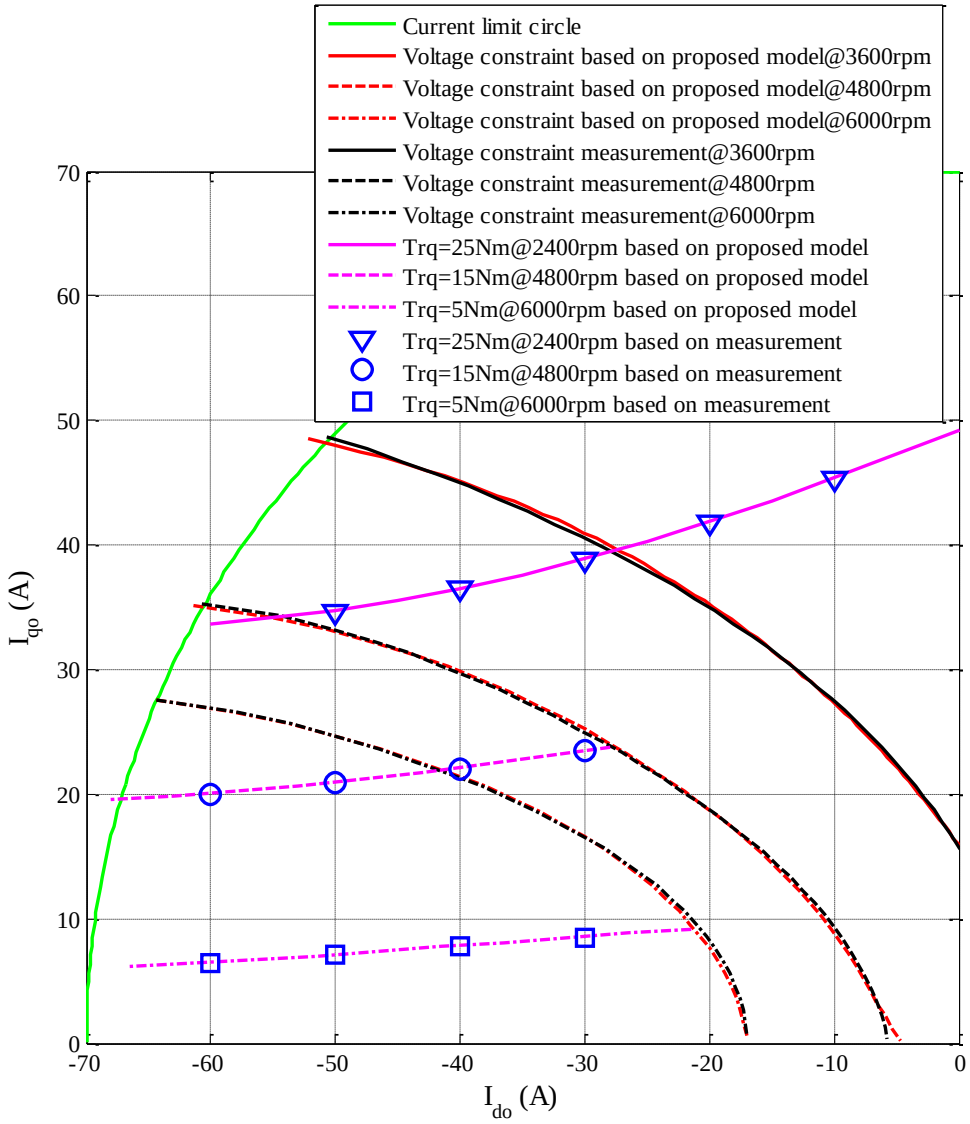

Fig. 5.8. Voltage constraints and constant torque loci based on the proposed model and measurement.

5.5.2 Loss-Minimization-Based Current Reference

When the motor's parameters change in a wide range, as shown in Fig. 5.7, all the optimal curves, voltage limit ellipses and the constant torque loci are distorted compared to the ones depicted in chapter 4. The current commands for given torque and speed should be recalculated; otherwise, they could be far away from the optimal operating points. Besides, the inaccuracy of the operating boundaries can result in unsecured operation for the machine. For example, at high speed, if the applied negative *d*-axis current is not big enough, the current vector can be located outside of the voltage limit ellipse. It can lead to control oscillation. No matter which situation happens, the burden of the current feedback regulators could be increased.

Based on the LUTs of the equivalent inverter-loss resistance, loss torque $T_{Fe+fric}$, *d*- and *q*-axis flux-linkage profiles, here proposes the algorithm to obtain the optimal current references at different loads and speeds. First of all, the torque-speed envelope should be determined. In other words, within the current and voltage constraints, the maximum output torque at each speed should be calculated. It can be accomplished by solving the optimization problem shown in (5.16). The cost function is built while the machine is operating in the motoring mode.

Minimize

$$-T_o = T_{Fe+fric} - \frac{3}{2}P\left(\Lambda_d i_{qo} - \Lambda_q i_{do}\right) \tag{5.16}$$

Subject to

$$i_{do}^2 + i_{qo}^2 \le I_{am}^2$$

$$v_d^2 + v_q^2 = \left[\left(R_s + R_{inv}\right) i_{do} - \omega_e \Lambda_q\right]^2 + \left[\left(R_s + R_{inv}\right) i_{qo} + \omega_e \Lambda_d\right]^2 \le V_{am}^2$$

The optimum current reference at each given torque and speed can be found by solving the optimization problem in (5.17). The cost function is the total electrical loss in the IPMSM drive system. The optimization is constrained by the torque command, current limit circle, and voltage limit ellipse.

Minimize

$$P_E = P_{Cu} + P_{Inv} + P_{Fe} = \frac{3}{2}\left(R_s + 2R_{Inv}\right)\left(i_{do}^2 + i_{qo}^2\right) + \frac{3\omega_e^2}{2R_c}\left(\Lambda_d^2 + \Lambda_q^2\right) \tag{5.17}$$

Subject to

$$T_o^* = \frac{3}{2} P\left(\Lambda_d i_{qo} - \Lambda_q i_{do}\right) - T_{Fe+fric}$$

$$i_{do}^2 + i_{qo}^2 \le I_{am}^2$$

$$v_d^2 + v_q^2 = \left[\left(R_s + R_{inv}\right) i_{do} - \omega_e \Lambda_q\right]^2 + \left[\left(R_s + R_{inv}\right) i_{qo} + \omega_e \Lambda_d\right]^2 \le V_{am}^2$$

where T_o^* is the desired output torque.

However, R_c is included in the cost function of (5.17). In order to eliminate the necessity of the separation of the core loss from the mechanical loss, the minimization object should be replaced by the total loss of the IPMSM drive. The optimization problem is revised and shown in (5.18).

Minimize

$$P_{loss} = P_{in} - P_{out} = \frac{3}{2}\left(v_d i_{do} + v_q i_{qo}\right) - T_o \omega_m \tag{5.18}$$

Subject to

$$T_o^* = \frac{3}{2} P\left(\Lambda_d i_{qo} - \Lambda_q i_{do}\right) - T_{Fe+fric}$$

$$i_{do}^2 + i_{qo}^2 \le I_{am}^2$$

$$v_d^2 + v_q^2 = \left[\left(R_s + R_{inv}\right) i_{do} - \omega_e \Lambda_q\right]^2 + \left[\left(R_s + R_{inv}\right) i_{qo} + \omega_e \Lambda_d\right]^2 \le V_{am}^2$$

The cost function in (5.18) has only one more term, which is the mechanical loss, than the optimization object in (5.17). It can be proved as shown below.

$$P_{loss} = P_{In} - P_{out} = \frac{3}{2}\left(v_d i_{do} + v_q i_{qo}\right) - T_o \omega_m$$

$$= \frac{3}{2}\left\{\left[\left(R_s + R_{Inv}\right) i_{do} - \omega_e \Lambda_q\right] i_{do} + \left[\left(R_s + R_{Inv}\right) i_{qo} + \omega_e \Lambda_d\right] i_{qo}\right\}$$
$$- \left\{\frac{3}{2} P\left[\Lambda_d\left(i_{qo} - \frac{\omega_e \Lambda_d}{R_c}\right) - \Lambda_q\left(i_{do} + \frac{\omega_e \Lambda_q}{R_c}\right)\right] - T_{fric}\right\}\omega_m$$

$$= \frac{3}{2}\left(R_s + R_{Inv}\right)\left(i_{do}^2 + i_{qo}^2\right) + \frac{3\omega_e^2}{2R_c}\left(\Lambda_d^2 + \Lambda_q^2\right) + T_{fric}\omega_m$$

$$= P_{Cu} + P_{Inv} + P_{Fe} + P_m$$

The solutions to the optimization problems in (5.18) and (5.17) are same. At a fixed speed, the mechanical loss is constant. It is only an offset to the cost function. Besides, these two optimization problems share the same constraints. In one word, the identical

optimal current reference can be obtained by solving (5.18) as the reference is generated in (5.17). In (5.18), the equivalent core-loss resistance is not required for the optimization. The proposed algorithm for the optimal current reference generation is easier to implement.

The detailed procedure to obtain the optimal *d*- and *q*-axis current reference is shown in Fig. 5.9. In the figure, *i* and *j* are the indexes referring to different speed and torque, respectively; ω_{min} and ω_{max} are the minimum and maximum operating speed of the IPM machine; T_{min} is the minimum operating torque; $T_{max}(i)$ is the maximum output torque at *i*th speed; $\Delta\omega$ and ΔT denote the speed and torque step length. The optimum current references for the DUT are shown in Fig. 5.10.

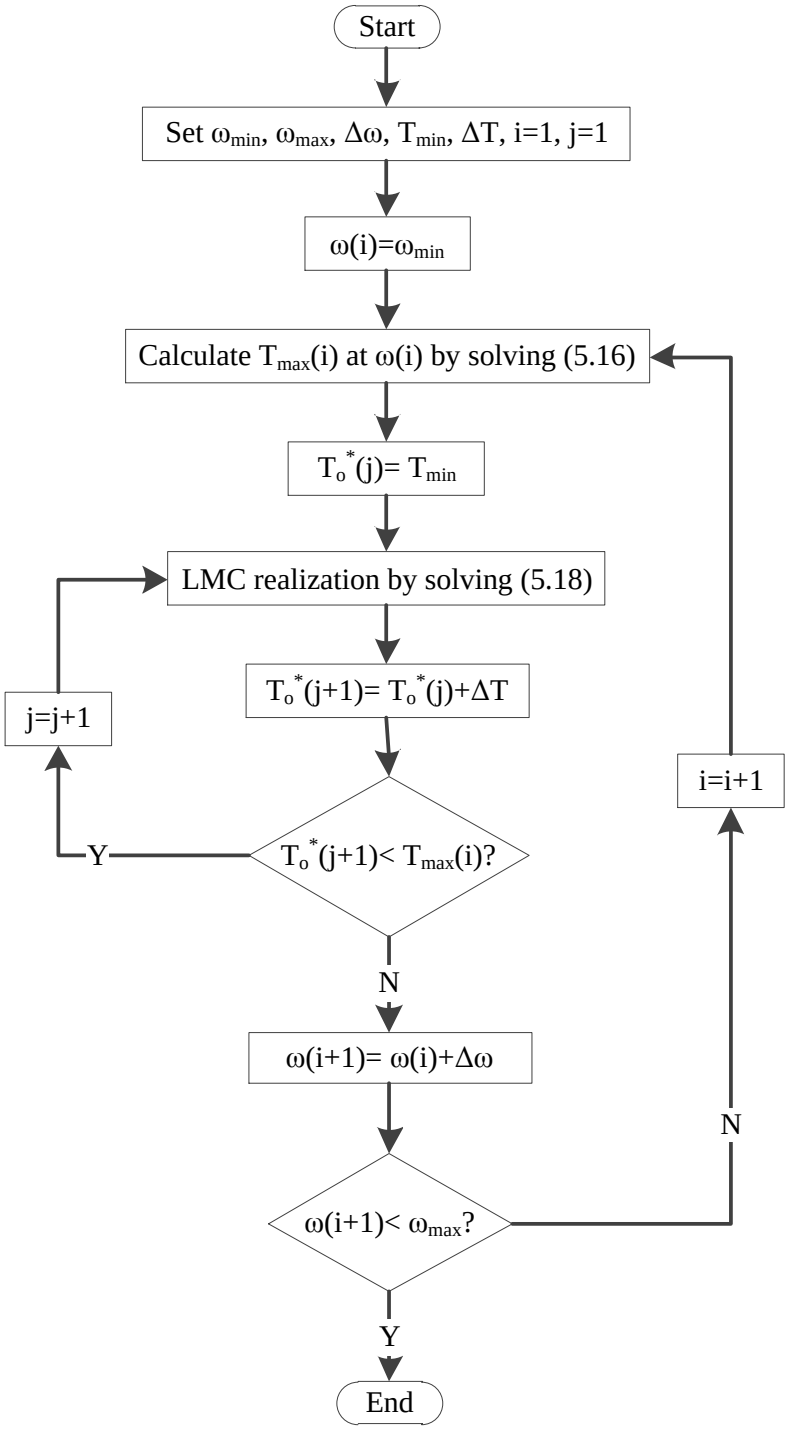

Fig. 5.9. Flowchart of the optimal current command generation.

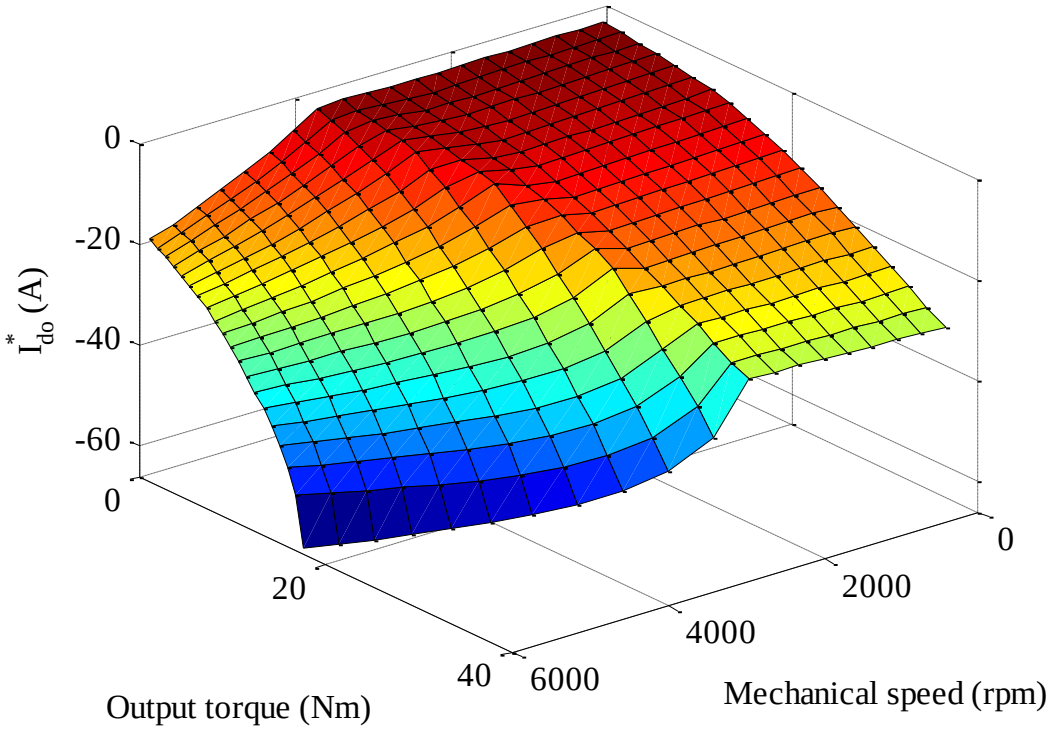
0
-20
-40
-60
I^*_{do} (A)
0
20
40
Output torque (Nm)
0
2000
4000
6000
Mechanical speed (rpm)

(a)

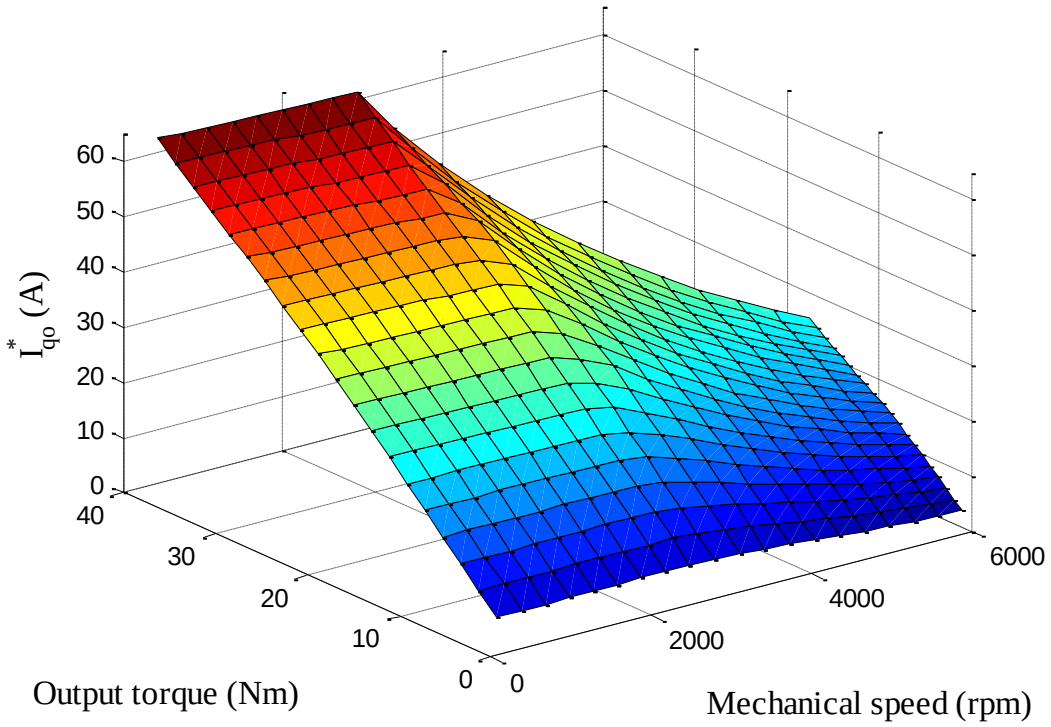

(b)

Fig. 5.10. Optimal current commands. (a) *d*-axis current; (b) *q*-axis current.

5.5.3 Torque Control System Design for IPMSM Drives

Based on the proposed algorithms for IPMSM drive modeling, the parameter characterization, torque estimation, and loss minimization, here proposes the torque control system, aiming at high-accuracy torque control, high efficiency, and fast dynamic response. Fig. 5.11 shows the diagram of the proposed control system. The voltage source inverter (VSI) converts DC power into AC power to drive the IPM motor. For the closed-

loop control, the machine's current and rotor position/speed are monitored. The similar structure of torque control system is proposed in [56].

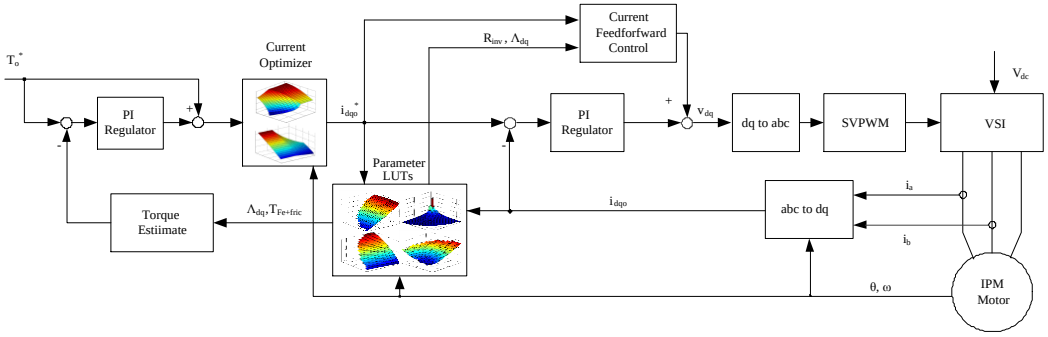

Fig. 5.11. Diagram of the proposed IPMSM drive system.

The proposed IPMSM drive system contains two control loops. The inner loop is the current-control loop and the outer one is for torque control. Both the torque and current control include the feedforward and feedback control. The feedforward controllers are designed for the fast dynamic response performance. On one hand, the feedforward controller can directly output the desired commands for given references. On the other hand, when the maximum power output is required, the overmodulation or even six-step operation is involved. In this case, the feedback controller can be saturated, thus the response of the IPMSM drive becomes slow. The problem can be solved by only using feedforward control and disabling the feedback control when the control saturation appears. Besides, the utilization of the proposed algorithms enables the feedforward controller to output very accurate voltage commands, which significantly reduces the current feedback controller's burden. The feedback controllers are designed to eliminate

the steady-state error due to the uncertainty nature of the parameters' estimation, and dynamically regulate the torque and current.

The 4D LUTs built in section 5.5.1 are used for torque estimation in (5.13) and current feedforward control in (4.2) in real time. For the torque estimation, the inputs of the parameter LUTs are the machine's speed, the feedback *d*- and *q*-axis current, and the outputs are the equivalent loss torque, the *d*- and *q*-axis flux-linkage. For the current feedforward control, the inputs of the LUTs are the machine's speed and the *d*- and *q*-axis current commands, and the outputs are the equivalent inverter-loss resistance, the *d*- and *q*-axis flux-linkage.

The optimal current reference within the current and voltage limitation can be found in the LUTs for the current optimizer. The tables are established by solving the optimization problem in (5.18). Their inputs are the torque control command and the feedback speed. The utilization of these LUTs involves the interpolation technique.

5.6 Experimental Results

The test bench shown in Fig. 3.7 is used to validate the proposed algorithms. Expect the equipment mentioned in chapter 3, YOKOGAWA WT1800 is used to monitor the electrical input power and the inverter output power. The high-precision current transducer, ULTRASTAB 867, is applied to guarantee the accuracy of the measurement. VN1630 is adopted as the physical layer of the CAN bus communication between the computer and the control board. The interface software is CANoe 8.1.

First of all, the torque accuracy is examined by using the current references in Fig. 5.12. In this section, torque estimation error is defined as $\frac{T_{estimate}-T_{measured}}{T_{estimate}}\times 100\%$, and the flux-linkage profiles are calculated by using (5.9) and (5.10). When torque equation (5.1) is applied, the maximum error of the torque estimation is 6%, as shown in Fig. 5.12(a). In most cases, the estimated torque is bigger than the output torque because the core loss is not considered in the conventional motor model. However, the no-load torque contains the core loss generated by the permanent-magnet flux-linkage. Besides, small negative *d*-axis current can decrease the core loss. Thus, in the low-torque region, the error is negative. In Fig. 5.12(b), the torque estimation error based on the proposed torque equation in (5.13) with 3D LUTs of the parameters is shown. The maximum error is reduced to 3%. The method does not consider the parameters' variation with respect to speed. It can be seen that the torque is over-compensated at lower speed and under-compensated at higher speed. In Fig. 5.12(c), it shows that the maximum torque estimation error based on the proposed model with 4D parameter LUTs is only 1.5% in full speed range. The high-accuracy torque control is achieved.

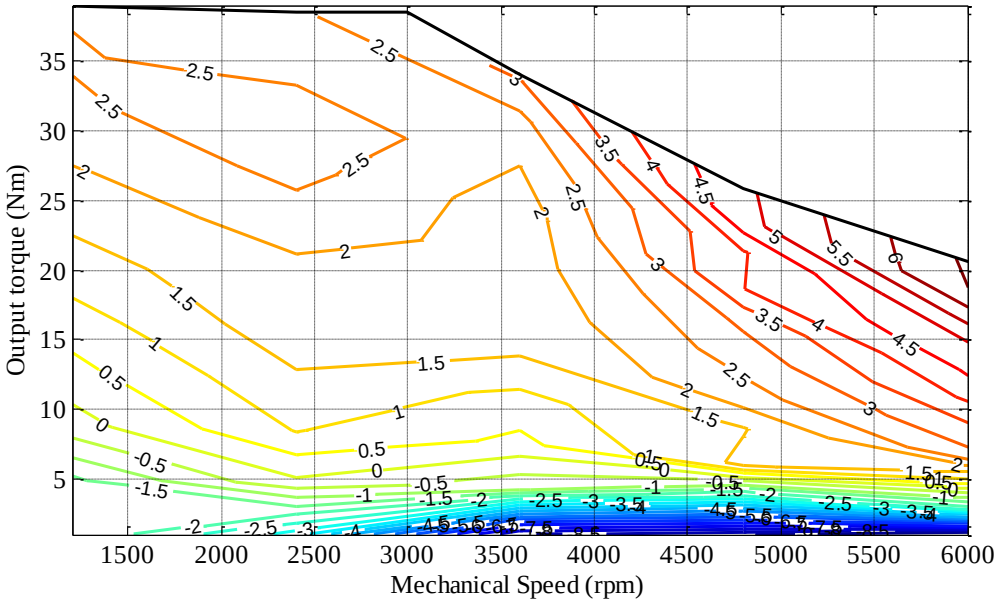
Output torque (Nm)
Mechanical Speed (rpm)
35
30
25
20
15
10
5
1500
2000
2500
3000
3500
4000
4500
5000
5500
6000

(a)

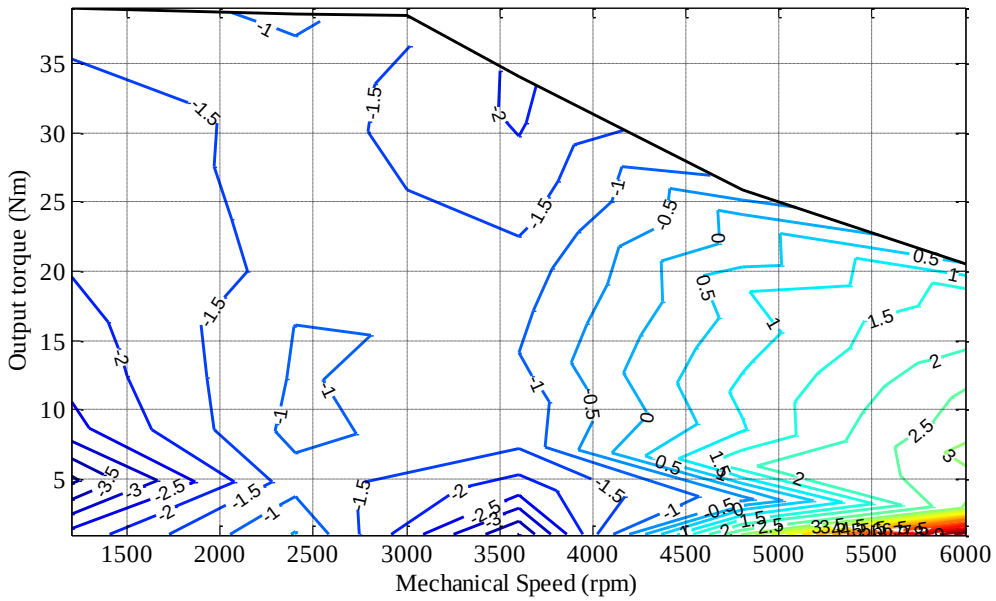
Output torque (Nm)
Mechanical Speed (rpm)
35
30
25
20
15
10
5
1500
2000
2500
3000
3500
4000
4500
5000
5500
6000

(b)

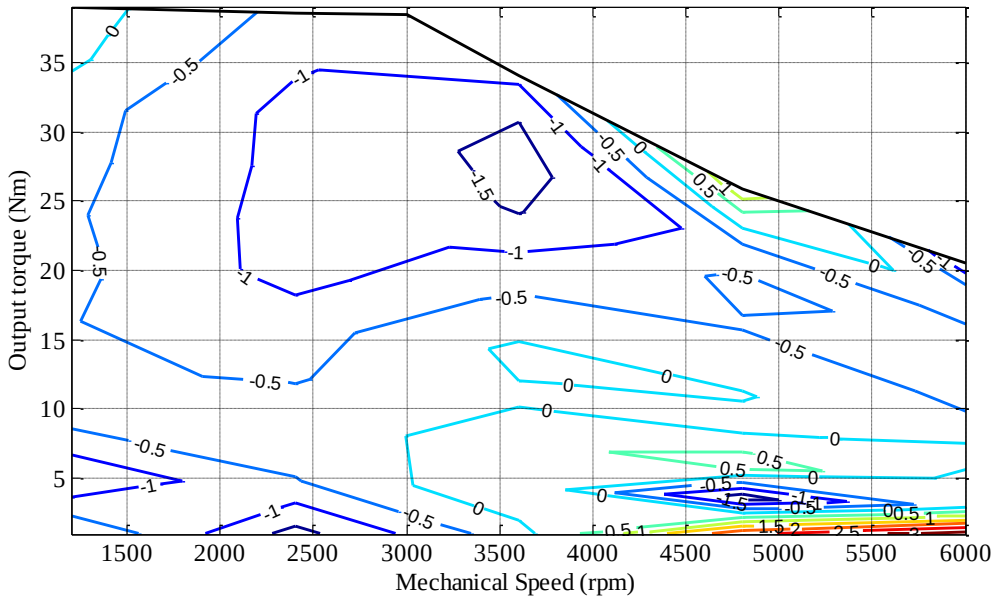

(c)

Fig. 5.12. Torque estimation error (%) of the IPMSM drive under test. (a) Based on the conventional IPMSM model with no-load torque compensation. (b) Based on the proposed IPMSM drive modeling with 3D parameter LUTs and no-load torque compensation. (c) Based on the proposed IPMSM drive modeling with 4D parameter LUTs.

The proposed LMC algorithm is validated and the experimental result is shown in Fig. 5.13. In Fig. 5.13(a) the tested operating points are selected at 10Nm@1200rpm, 30Nm@1200rpm, and 10Nm@6000rpm, respectively. The red markers are chosen by the proposed optimization algorithm in (5.18). In Fig. 5.13(b) the total losses (P_{in} - P_{out}) vs. the applied *d*-axis current at the selected operating points are plotted. It can be seen that the loss increase as the speed increases at 10Nm. The total loss becomes bigger as the

output torque increases at 1200rpm. The proposed optimization algorithm looks more 'efficient' in the flux-weakening region since the loss is relatively big. At lower speed, the optimization looks more 'flat'.

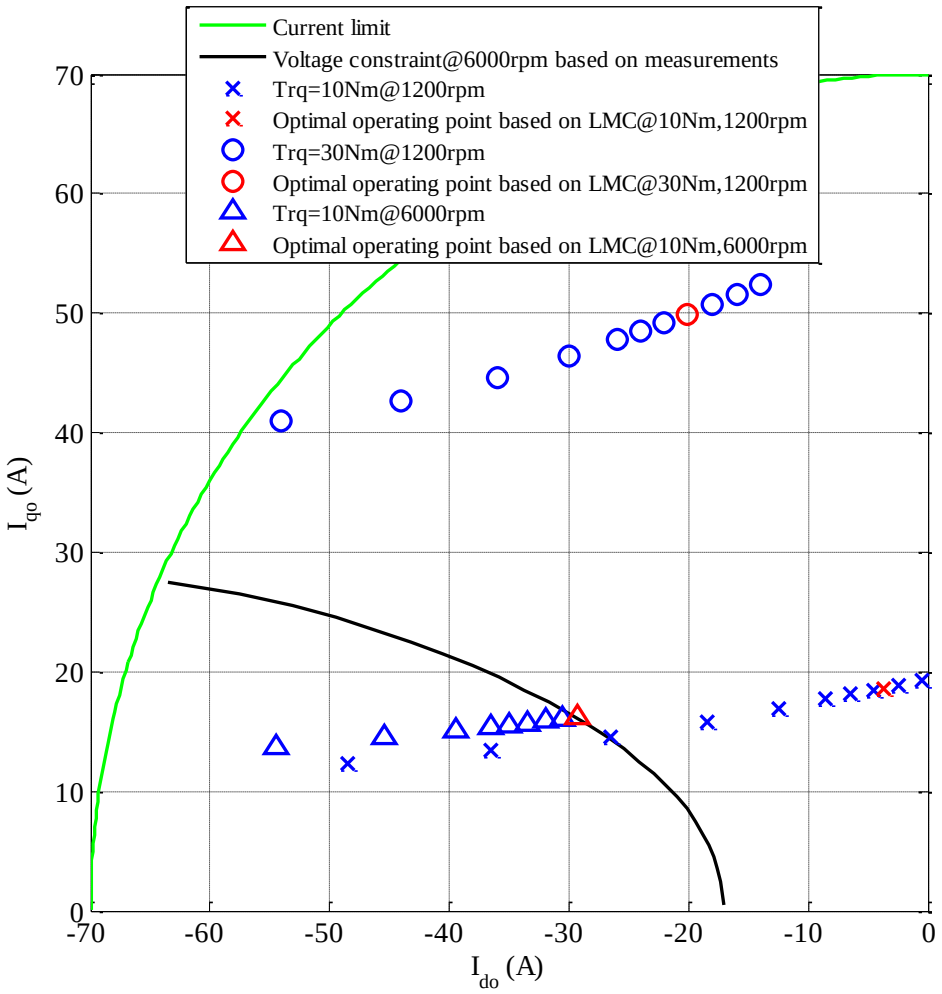

(a)

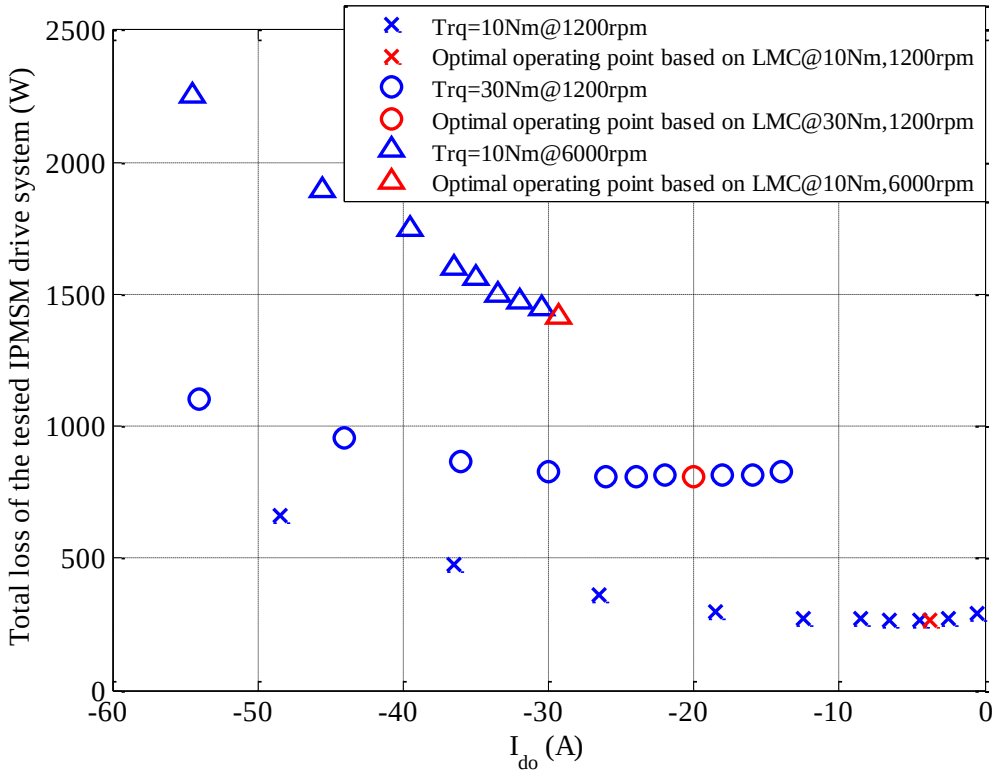

(b)

Fig. 5.13. LMC validation. (a) Selection of the tested operating points. (b) Total losses at the selected operating points.

The efficiency map based on the proposed LMC in (5.18) is shown in Fig. 5.14. The DC input power is measured by using the power analyzer and the mechanical output power is sampled by the torque transducer. The efficiency is calculated as $\eta = \frac{P_{out}}{P_{in}} \times 100\%$.

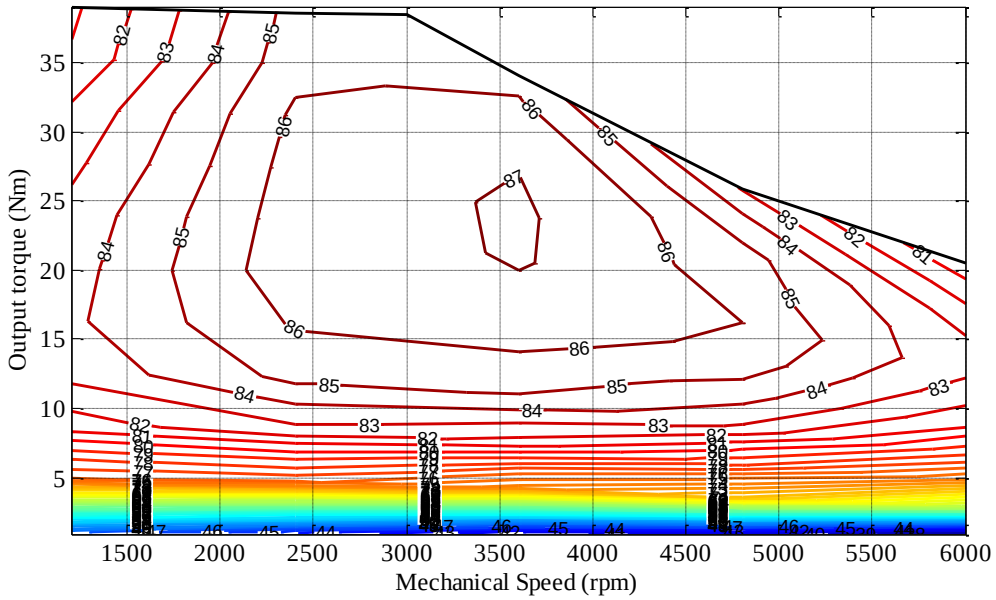

Fig. 5.14. Efficiency map of the IPMSM drive system under test.

5.7 Conclusions

All the nonlinearities in the IPMSM drives have been studied. The detailed scheme for the parameters' characterization in the proposed equivalent circuit is illustrated, including the *d*- and *q*-axis flux-linkage profiles, the equivalent inverter-loss resistance, and loss torque caused by the core loss and mechanical loss. The back-fitting based algorithm for torque estimation is proposed. The separation of the mechanical loss and the core loss is not required for the calculation. The influence of the nonlinearities on voltage limit ellipse is analyzed. Compared to the conventional IPMSM modeling, the proposed model offers more accurate voltage constraint prediction. The method to obtain the optimal current reference based on the 4D parameter LUTs is proposed. The torque control system for

IPMSM drives is designed, aiming at high-accuracy torque delivery, high efficiency, and fast dynamic response performance. The experimental results reveal that the maximum error of the torque control is only 1.5% in the entire torque-speed range. For given torque and speed, the minimum total loss is produced.

Chapter 6

Conclusions and Future Work

6.1 Conclusions

This thesis presents the high-accuracy torque control and estimation for IPMSM drives with loss minimization.

The nonlinear flux-linkage model for IPMSM, aiming at MTPA fitting and torque estimation, is proposed. The saturation and cross-coupling effects are considered while the model is designed. An optimization problem is formulated to find the constant coefficients in the proposed model based on the measured flux-linkage data at only nine specific operating points. No selection of weight factors is required in the cost function. The proposed algorithm can be implemented without the machine's information and the torque sensor. Both simulation and experiment have been conducted for validation in motoring and generating modes. The results show that the desired copper-loss minimization control can be achieved. The torque identification algorithm can be used as a torque sensor with 5% full-scale error.

A novel IPMSM drive model is proposed with all the losses considered. The analytical expressions with constant parameters for the loss minimization control with respect to the different reference current, including the current in the flux-linkage branch and the

winding current, are established. How to find the optimal operating point for given torque and speed is formulated. The optimality is also proved. Compared to MTPA control, LMC introduces more efficient energy utilization. The influence of different parameters on the current limit circle and the voltage limit ellipse is explicitly analyzed in different coordinates. The simulation results validate the mathematical deductions. Although all the parameters are not invariant in a real machine, the proposed algorithms provide with the overview of the variation of the optimal current reference and operating constraints in terms of different parameters. They can be used as the powerful tool for analysis in the local region.

The nonlinearities of IPMSM drives are studied. Based on the proposed model, the experiment-based parameter characterization is illustrated. The back-fitting based torque identification technique is proposed. It can be implemented without the manufacturing the dummy rotor. The influence of the nonlinearities on the voltage limit ellipse is analyzed. Based on the proposed IPMSM drive model and the characterized parameters, both accurate torque estimation and precise voltage output prediction can be realized. The optimization algorithm is presented. The resulted current reference leads to the minimum total loss for given torque and speed. The torque control system is designed for the IPMSM drives, aiming at high-accuracy torque delivery, high operating efficiency, and fast dynamic response performance. The experimental results reveal that the maximum torque control error is only 1.5% at all speeds, and the efficiency of the IPMSM drive system is maximized by the proposed loss-minimization algorithm.

6.2 Future Work

The research topics that can be further investigated are listed as follows.

Firstly, expect the current and speed, the DC bus voltage also has an impact on the machine's parameters, especially the inverter loss, and the feasible operating region at high speed. It is interesting to identify how they change and how to adjust the control to the variation.

Secondly, although the flux-linkage characterization is researched, how to distinguish the values of the *d*-axis inductance and the permanent-magnet flux-linkage is challenging. On one hand, the identified L_d and Λ_{pm} can be used in many applications, such as sensorless control. On the other hand, once the relationship between the permanent-magnet flux-linkage and the temperature is established, the rotor's temperature can be estimated. The result can be applied to protect the machine in case the permanent magnet is demagnetized forever and keep the IPMSM drive's performance. For example, it is interesting to hold the output torque invariant with the changing temperature.

References

[1] T. M. Jahns, G. B. Kliman, and T. W. Neumann, "Interior permanent-magnet synchronous motors for adjustable-speed drives," *IEEE Trans. Ind. Appl.*, vol. IA-22, no. 4, pp. 738–747, Jul. 1986.

[2] J. Wai and T. M. Jahns, "A new control technique for achieving wide constant power speed operation with an interior PM alternator machine," in *Conference Record of the 2001 IEEE Industry Applications Conference*, Chicago, IL, USA, USA, 2001, vol. 2, pp. 807–814.

[3] Y. Yang *et al.*, "Design and Comparison of Interior Permanent Magnet Motor Topologies for Traction Applications," *IEEE Trans. Transp. Electrification*, vol. 3, no. 1, pp. 86–97, Mar. 2017.

[4] J. Li and X. Cheng, "The development trend of PM synchronous machine," *Explos.-Proof Electr. Mach.*, vol. 44, no. 5, pp. 1–4, Sep. 2009.

[5] S. Morimoto, K. Kawamoto, M. Sanada, and Y. Takeda, "Sensorless control strategy for salient-pole PMSM based on extended EMF in rotating reference frame," *IEEE Trans. Ind. Appl.*, vol. 38, no. 4, pp. 1054–1061, Jul. 2002.

[6] Y. Sun, M. Preindl, S. Sirouspour, and A. Emadi, "Unified Wide-Speed Sensorless Scheme Using Nonlinear Optimization for IPMSM Drives," *IEEE Trans. Power Electron.*, vol. 32, no. 8, pp. 6308–6322, Aug. 2017.

[7] H. Ge, *Fractional slot concentrated winding interior permanent magnet machines with reluctance torque: inductance-based methodology for comprehensive analysis, design, and control*, Ph. D. Dissertation. Hamilton, ON, Canada: McMaster University, 2016.

[8] W. Liang, W. Fei, and P. C.-K. Luk, "An improved sideband current harmonic model of interior PMSM drive by considering magnetic saturation and cross-coupling effects," *IEEE Trans. Ind. Electron.*, vol. 63, no. 7, pp. 4097–4104, Jul. 2016.

[9] X. Liu, H. Chen, J. Zhao, and A. Belahcen, "Research on the performances and parameters of interior PMSM used for electric vehicles," *IEEE Trans. Ind. Electron.*, vol. 63, no. 6, pp. 3533–3545, Jun. 2016.

[10] A. Pouramin, R. Dutta, M. F. Rahman, J. E. Fletcher, and D. Xiao, "A preliminary study of the effect of saturation and cross-magnetization on the inductances of a fractional-slot concentrated-wound interior PM synchronous machine," in *IEEE 11th International Conference on Power Electronics and Drive Systems (PEDS)*, Sydney, NSW, Australia, 2015, pp. 828–833.

[11] S. Morimoto, K. Hatanaka, Y. Tong, Y. Takeda, and T. Hirasa, "Servo drive system and control characteristics of salient pole permanent magnet synchronous motor," *IEEE Trans. Ind. Appl.*, vol. 29, no. 2, pp. 338–343, Apr. 1993.

[12] S. Morimoto, Y. Takeda, T. Hirasa, and K. Taniguchi, "Expansion of operating limits for permanent magnet motor by current vector control considering inverter capacity," *IEEE Trans. Ind. Appl.*, vol. 26, no. 5, pp. 866–871, Oct. 1990.

[13] Bon-Ho Bae, N. Patel, S. Schulz, and Seung-Ki Sul, "New field weakening technique for high saliency interior permanent magnet motor," in *38th IAS Annual Meeting*, Salt Lake City, UT, USA, 2003, vol. 2, pp. 898–905.

[14] Kaiping Yu, Hong Guo, Zedong Sun, and Zhiyong Wu, "Efficiency optimization control of Permanent Magnet Synchronous Motor for Electric Propulsion System," in *2013 International Conference on Electrical Machines and Systems (ICEMS)*, Busan, South Korea, 2013, pp. 56–61.

[15] F. C. F. Azevedo and M. N. Uddin, "Recent advances in loss minimization algorithms for IPMSM drives," in *2014 IEEE Industry Applications Society Annual Meeting*, Vancouver, BC, Canada, 2014, pp. 1–9.

[16] Meifen Cao, J. Egashira, and K. Kaneko, "High efficiency control of IPMSM for electric motorcycles," in *IEEE 6th International Power Electronics and Motion Control Conference (IPEMC)*, Wuhan, China, 2009, pp. 1893–1897.

[17] R. S. Colby and D. W. Novotny, "An efficiency-optimizing permanent-magnet synchronous motor drive," *IEEE Trans. Ind. Appl.*, vol. 24, no. 3, pp. 462–469, Jun. 1988.

[18] S. Vaez, V. I. John, and M. A. Rahman, "An on-line loss minimization controller for interior permanent magnet motor drives," *IEEE Trans. Energy Convers.*, vol. 14, no. 4, pp. 1435–1440, Dec. 1999.

[19] M. Cao, "Online loss minimization control of IPMSM for electric scooters," in *2010 International Power Electronics Conference (IPEC)*, Sapporo, Japan, 2010, pp. 1388–1392.

[20] E. S. Sergaki, P. S. Georgilakis, A. G. Kladas, and G. S. Stavrakakis, "Fuzzy logic based online electromagnetic loss minimization of permanent magnet synchronous motor drives," in *18th International Conference on Electrical Machines (ICEM)*, Vilamoura, Portugal, 2008, pp. 1–7.

[21] Xianqing Cao and Liping Fan, "Efficiency-optimized vector control of PMSM drive for hybrid electric vehicle," in *International Conference on Mechatronics and Automation*, Changchun, China, 2009, pp. 423–427.

[22] M. Cao and N. Hoshi, "Electrical loss minimization strategy for interior permanent magnet synchronous motor drives," in *IEEE Vehicle Power and Propulsion Conference (VPPC)*, Lille, France, 2010, pp. 1–6.

[23] M. Nasir Uddin and J. Khastoo, "Fuzzy logic-based efficiency optimization and high dynamic performance of IPMSM drive system in both transient and steady-state conditions," *IEEE Trans. Ind. Appl.*, vol. 50, no. 6, pp. 4251–4259, Nov. 2014.

[24] M. Nasir Uddin and B. Patel, "Loss minimization control of interior permanent magnet synchronous motor drive using adaptive backstepping technique," in *IEEE Industry Applications Society Annual Meeting*, Lake Buena Vista, FL, USA, 2013, pp. 1–7.

[25] C. Mademlis, I. Kioskeridis, and N. Margaris, "Optimal efficiency control strategy for interior permanent-magnet synchronous motor drives," *IEEE Trans. Energy Convers.*, vol. 19, no. 4, pp. 715–723, Dec. 2004.

[26] O. Ojo, F. Osaloni, Zhiqiao Wu, and M. Omoigui, "A control strategy for optimum efficiency operation of high performance interior permanent magnet motor drives," in *38th IAS Annual Meeting*, Salt Lake City, UT, USA, 2003, vol. 1, pp. 604–610.

[27] S. Morimoto, Y. Tong, Y. Takeda, and T. Hirasa, "Loss minimization control of permanent magnet synchronous motor drives," *IEEE Trans. Ind. Electron.*, vol. 41, no. 5, pp. 511–517, Oct. 1994.

[28] S. Vaez-Zadeh, M. Zamanifar, and J. Soltani, "Nonlinear efficiency optimization control of IPM synchronous motor drives with online parameter estimation," in *37th IEEE Power Electronics Specialists Conference*, Jeju, South Korea, 2006, pp. 1–6.

[29] M. N. Uddin and R. S. Rebeiro, "Online efficiency optimization of a fuzzy-logic-controller-based IPMSM drive," *IEEE Trans. Ind. Appl.*, vol. 47, no. 2, pp. 1043–1050, Mar. 2011.

[30] B. Stumberger, G. Stumberger, D. Dolinar, A. Hamler, and M. Trlep, "Evaluation of saturation and cross-magnetization effects in interior permanent-magnet synchronous motor," *IEEE Trans. Ind. Appl.*, vol. 39, no. 5, pp. 1264–1271, Sep. 2003.

[31] S. J. Underwood and I. Husain, "Online parameter estimation and adaptive control of permanent-magnet synchronous machines," *IEEE Trans. Ind. Electron.*, vol. 57, no. 7, pp. 2435–2443, Jul. 2010.

[32] N. C. Kar, S. Hamidifar, and M. Kazerooni, "Analytical modelling and parametric sensitivity analysis for the PMSM steady-state performance prediction," *IET Electr. Power Appl.*, vol. 7, no. 7, pp. 586–596, Aug. 2013.

[33] C. Mademlis and N. Margaris, "Loss minimization in vector-controlled interior permanent-magnet synchronous motor drives," *IEEE Trans. Ind. Electron.*, vol. 49, no. 6, pp. 1344–1347, Dec. 2002.

[34] H. Ge, B. Bilgin, and A. Emadi, "Global loss minimization control of PMSM considering cross-coupling and saturation," in *IEEE Energy Conversion Congress and Exposition (ECCE)*, Montreal, QC, Canada, 2015, pp. 6139–6144.

[35] Fang Deng, "An improved iron loss estimation for permanent magnet brushless machines," *IEEE Trans. Energy Convers.*, vol. 14, no. 4, pp. 1391–1395, Dec. 1999.

[36] Jin Hur, "Characteristic analysis of interior permanent-magnet synchronous motor in electrohydraulic power steering systems," *IEEE Trans. Ind. Electron.*, vol. 55, no. 6, pp. 2316–2323, Jun. 2008.

[37] H. Domeki *et al.*, "Investigation of benchmark model for estimating iron loss in rotating machine," *IEEE Trans. Magn.*, vol. 40, no. 2, pp. 794–797, Mar. 2004.

[38] H. Cao, B. Kou, D. Zhang, W. Li, and X. Zhang, "Research on loss of high speed permanent magnet synchronous motor for flywheel energy storage," in *16th*

International Symposium on Electromagnetic Launch Technology (EML), Beijing, China, 2012, pp. 1–6.

[39] Chunting Mi, G. R. Slemon, and R. Bonert, "Modeling of iron losses of permanent-magnet synchronous motors," *IEEE Trans. Ind. Appl.*, vol. 39, no. 3, pp. 734–742, May 2003.

[40] K. Yamazaki and A. Abe, "Loss investigation of interior permanent-magnet motors considering carrier harmonics and magnet eddy currents," *IEEE Trans. Ind. Appl.*, vol. 45, no. 2, pp. 659–665, 2009.

[41] K. Yamazaki and Y. Kato, "Iron loss analysis of interior permanent magnet synchronous motors by considering mechanical stress and deformation of stators and rotors," *IEEE Trans. Magn.*, vol. 50, no. 2, pp. 909–912, Feb. 2014.

[42] B. Stumberger, A. Hamler, and B. Hribernik, "Analysis of iron loss in interior permanent magnet synchronous motor over a wide-speed range of constant output power operation," *IEEE Trans. Magn.*, vol. 36, no. 4, pp. 1846–1849, Jul. 2000.

[43] R. Ni, D. Xu, G. Wang, L. Ding, G. Zhang, and L. Qu, "Maximum efficiency per ampere control of permanent-magnet synchronous machines," *IEEE Trans. Ind. Electron.*, vol. 62, no. 4, pp. 2135–2143, Apr. 2015.

[44] H. Ge, Y. Miao, B. Bilgin, B. Nahid-Mobarakeh, and A. Emadi, "Speed range extended maximum torque per ampere control for PM drives considering inverter and motor nonlinearities," *IEEE Trans. Power Electron.*, vol. 32, no. 9, pp. 7151–7159, Sep. 2017.

[45] N. Urasaki, T. Senjyu, and K. Uezato, "A novel calculation method for iron loss resistance suitable in modeling permanent-magnet synchronous motors," *IEEE Trans. Energy Convers.*, vol. 18, no. 1, pp. 41–47, Mar. 2003.

[46] N. Urasaki, T. Senjyu, and K. Uezato, "Investigation of influences of various losses on electromagnetic torque for surface-mounted permanent magnet synchronous motors," *IEEE Trans. Power Electron.*, vol. 18, no. 1, pp. 131–139, Jan. 2003.

[47] Y. Miao, H. Ge, M. Preindl, J. Ye, B. Cheng, and A. Emadi, "MTPA fitting and torque estimation technique based on a new flux-linkage model for interior permanent magnet synchronous machines," *IEEE Trans. Ind. Appl.*, vol. 53, no. 6, pp. 5451–5460, Nov.-Dec. 2017.

[48] Y. Miao, B. Cheng, and A. Emadi, "A method and circuit for simulating an interior permanent magnet synchronous machine drive system with high accuracy torque control and loss minimization," U.S. Patent, 2017P00504IN, filed in Dec. 20th, 2017.

[49] M. Preindl and S. Bolognani, "Optimal state reference computation with constrained MTPA criterion for PM motor drives," *IEEE Trans. Power Electron.*, vol. 30, no. 8, pp. 4524–4535, Aug. 2015.

[50] S. Morimoto, M. Sanada, Y. Takeda, and K. Taniguchi, "Optimum machine parameters and design of inverter-driven synchronous motors for wide constant power operation," in *Industry Applications Society Annual Meeting*, Denver, CO, US, 1994, pp. 177–182.

[51] K. Chang, *Loss minimization control of permanent magnet synchronous machine for electric vehicle applications*, Master thesis. Montreal, Quebec, Canada: Concordia University, 2013.

[52] M. Preindl and S. Bolognani, "Model predictive direct torque control with finite control set for PMSM drive systems, part 2: field weakening operation," *IEEE Trans. Ind. Inform.*, vol. 9, no. 2, pp. 648–657, May 2013.

[53] T. Inoue, Y. Inoue, S. Morimoto, and M. Sanada, "Mathematical model for MTPA control of permanent-magnet synchronous motor in stator flux linkage synchronous frame," *IEEE Trans. Ind. Appl.*, vol. 51, no. 5, pp. 3620–3628, Sep. 2015.

[54] Y. A.-R. I. Mohamed and T. K. Lee, "Adaptive self-tuning MTPA vector controller for IPMSM drive system," *IEEE Trans. Energy Convers.*, vol. 21, no. 3, pp. 636–644, Sep. 2006.

[55] T. Sun, J. Wang, and X. Chen, "Maximum torque per ampere (MTPA) control for interior permanent magnet synchronous machine drives based on virtual signal injection," *IEEE Trans. Power Electron.*, vol. 30, no. 9, pp. 5036–5045, Sep. 2015.

[56] Bing Cheng and T. R. Tesch, "Torque feedforward control technique for permanent-magnet synchronous motors," *IEEE Trans. Ind. Electron.*, vol. 57, no. 3, pp. 969–974, Mar. 2010.

[57] C.-T. Pan and S.-M. Sue, "A linear maximum torque per ampere control for IPMSM drives over full-speed range," *IEEE Trans. Energy Convers.*, vol. 20, no. 2, pp. 359–366, Jun. 2005.

[58] K. J. Meessen, P. Thelin, J. Soulard, and E. A. Lomonova, "Inductance calculations of permanent-magnet synchronous machines including flux change and self- and cross-saturations," *IEEE Trans. Magn.*, vol. 44, no. 10, pp. 2324–2331, Oct. 2008.

[59] Seungho Lee, Yu-Seok Jeong, Yong-Jae Kim, and Sang-Yong Jung, "Novel analysis and design methodology of interior permanent-magnet synchronous motor using newly adopted synthetic flux linkage," *IEEE Trans. Ind. Electron.*, vol. 58, no. 9, pp. 3806–3814, Sep. 2011.

[60] M. N. Uddin, T. S. Radwan, and M. A. Rahman, "Performance of interior permanent magnet motor drive over wide speed range," *IEEE Trans. Energy Convers.*, vol. 17, no. 1, pp. 79–84, Mar. 2002.

[61] Q. Liu, A. Thul, and K. Hameyer, "A robust model reference adaptive controller for the PMSM drive system with torque estimation and compensation," in *2014 International Conference on Electrical Machines (ICEM)*, Berlin, Germany, 2014, pp. 665–671.

[62] W. Huang, Y. Zhang, X. Zhang, and G. Sun, "Accurate torque control of interior permanent magnet synchronous machine," *IEEE Trans. Energy Convers.*, vol. 29, no. 1, pp. 29–37, Mar. 2014.

[63] S. Bolognani, R. Petrella, A. Prearo, and L. Sgarbossa, "Automatic tracking of MTPA trajectory in IPM motor drives based on AC current injection," *IEEE Trans. Ind. Appl.*, vol. 47, no. 1, pp. 105–114, Jan. 2011.

[64] S. Kim, Y.-D. Yoon, S.-K. Sul, and K. Ide, "Maximum torque per ampere (MTPA) control of an IPM machine based on signal injection considering inductance saturation," *IEEE Trans. Power Electron.*, vol. 28, no. 1, pp. 488–497, Jan. 2013.

[65] R. Antonello, M. Carraro, and M. Zigliotto, "Maximum-torque-per-ampere operation of anisotropic synchronous permanent-magnet motors based on extremum seeking control," *IEEE Trans. Ind. Electron.*, vol. 61, no. 9, pp. 5086–5093, Sep. 2014.

[66] C. B. Butt, M. A. Hoque, and M. A. Rahman, "Simplified fuzzy-logic-based MTPA speed control of IPMSM drive," *IEEE Trans. Ind. Appl.*, vol. 40, no. 6, pp. 1529–1535, Nov. 2004.

[67] W. H. Press, Ed., *Numerical recipes in C: the art of scientific computing*, 2nd ed. Cambridge; New York: Cambridge University Press, 1992.

[68] S.-M. Sue and C.-T. Pan, "Voltage-constraint-tracking-based field-weakening control of IPM synchronous motor drives," *IEEE Trans. Ind. Electron.*, vol. 55, no. 1, pp. 340–347, Jan. 2008.

[69] E. C. Lovelace, T. M. Jahns, and J. H. Lang, "A saturating lumped-parameter model for an interior PM synchronous machine," *IEEE Trans. Ind. Appl.*, vol. 38, no. 3, pp. 645–650, May 2002.

[70] D. S. Kirschen, D. W. Novotny, and T. A. Lipo, "On-line efficiency optimization of a variable frequency induction motor drive," *IEEE Trans. Ind. Appl.*, vol. IA-21, no. 3, pp. 610–616, May 1985.

[71] Gyu-Sik Kim, In-Joong Ha, and Myoung-Sam Ko, "Control of induction motors for both high dynamic performance and high power efficiency," *IEEE Trans. Ind. Electron.*, vol. 39, no. 4, pp. 323–333, Aug. 1992.

[72] M. Zamanifar and S. Vaez-Zadeh, "Loss minimization sliding mode control of IPM synchronous motor drives," *SID J. Trans. Elect Tech*, vol. 2, pp. 67–73, 2010.

[73] N. Urasaki, T. Senjyu, and K. Uezato, "Neural network based high efficiency drive for interior permanent magnet synchronous motors compensating EMF constant variation," in *Power Conversion Conference*, Osaka, Japan, 2002, vol. 3, pp. 1273–1278.

[74] M. N. Uddin, R. S. Rebeiro, and Sheng Hua Lee, "Online efficiency optimization of an IPMSM drive incorporating loss minimization algorithm and an FLC as speed controller," in *IEEE International Symposium on Industrial Electronics*, Seoul, South Korea, 2009, pp. 1263–1268.

[75] N. R. Abjadi, J. Soltani, M. Pahlavaninizhad, and J. Askari, "A nonlinear adaptive controller for speed sensorless PMSM taking the iron loss resistance into account," in *Eighth International Conference on Electrical Machines and Systems (ICEMS)*, Nanjing, China, 2005, p. 188–193 Vol. 1.

[76] T. Senjyu, Y. Kuwae, N. Urasaki, and K. Uezato, "Accurate parameter measurement for high speed permanent magnet synchronous motors," in *IEEE 32nd Annual Power Electronics Specialists Conference*, Vancouver, BC, Canada, 2001, vol. 2, pp. 772–777.

[77] N. Urasaki, T. Senjyu, and K. Uezato, "An accurate modeling for permanent magnet synchronous motor drives," in *Fifteenth Annual IEEE Applied Power Electronics Conference and Exposition (APEC)*, New Orleans, LA, US, 2000, vol. 1, pp. 387–392.

[78] Q. K. Nguyen and J. Roth-Stielow, "Analysis and modelling of the losses for the electrical drive system of an electric vehicle," in *IEEE Vehicle Power and Propulsion Conference (VPPC)*, Coimbra, Portugal, 2014, pp. 1–6.

[79] J. Kim, I. Jeong, K. Nam, J. Yang, and T. Hwang, "Sensorless control of PMSM in a high-speed region considering iron loss," *IEEE Trans. Ind. Electron.*, vol. 62, no. 10, pp. 6151–6159, Oct. 2015.

[80] J. F. Gieras and M. Wing, *Permanent magnet motor technology: design and applications*, 2nd ed. New York: Marcel Dekker, 2002.

[81] S. L. Shmakov, "A universal method of solving quartic equations," *Int. J. Pure Appl. Math.*, vol. 71, pp. 251–259, 2011.

[82] C. P. Simon and L. Blume, *Mathematics for economists*, 1st ed. New York: Norton, 1994.

[83] A. E. Bryson and Y.-C. Ho, *Applied optimal control: optimization, estimation and control*. Washington, DC: Hemisphere Publ. [u.a.], 1975.

[84] D. P. Bertsekas, A. Nedić, and A. E. Ozdaglar, *Convex analysis and optimization*. Belmont, Mass: Athena Scientific, 2003.

[85] S. P. Boyd and L. Vandenberghe, *Convex optimization*. Cambridge, UK; New York: Cambridge University Press, 2004.

[86] F. L. Lewis, D. L. Vrabie, and V. L. Syrmos, *Optimal control*, 3. ed. Hoboken, NJ: Wiley, 2012.

[87] H. Aorith, J. Wang, and P. Lazari, "A new loss minimization algorithm for interior permanent magnet synchronous machine drives," in *IEEE International Electric Machines & Drives Conference (IEMDC)*, Chicago, IL, US, 2013, pp. 526–533.

[88] Junggi Lee, Kwanghee Nam, Seoho Choi, and Soonwoo Kwon, "Loss-minimizing control of PMSM with the use of polynomial approximations," *IEEE Trans. Power Electron.*, vol. 24, no. 4, pp. 1071–1082, Apr. 2009.

[89] G.-S. Li, J.-F. Xie, and L.-Y. Xu, "Maximum efficiency control method of permanent magnet synchronous motor based on three-dimensional table," in *International Conference on Advanced Mechatronic Systems (ICAMechS)*, Beijing, China, 2015, pp. 392–396.

[90] A. O. Di Tommaso, R. Miceli, G. R. Galluzzo, and M. Trapanese, "Efficiency maximization of permanent magnet synchronous generators coupled coupled to wind turbines," in *Power Electronics Specialists Conference*, Orlando, FL, US, 2007, pp. 1267–1272.

[91] W. Hassan and Bingsen Wang, "Efficiency optimization of PMSM based drive system," in *7th International Power Electronics and Motion Control Conference (IPEMC)*, Harbin, China, 2012, pp. 1027–1033.

[92] A. Rabiei, T. Thiringer, and J. Lindberg, "Maximizing the energy efficiency of a PMSM for vehicular applications using an iron loss accounting optimization based on nonlinear programming," in *International Conference on Electrical Machines (ICEM)*, Marseille, France, 2012, pp. 1001–1007.

[93] Shuo Zhang, Xiaomin Zhou, and Dawei Gao, "Strategy of efficiency optimization of PMSM-DTC system used for EVs," in *IEEE Conference and Expo Transportation Electrification Asia-Pacific (ITEC Asia-Pacific)*, Beijing, China, 2014, pp. 1–4.

[94] J. Zou, D. Zeng, Y. Xu, B. Wang, and Q. Wang, "An indirect testing method for the mechanical characteristic of multiunit permanent-magnet synchronous machines with concentrated windings," *IEEE Trans. Ind. Electron.*, vol. 62, no. 12, pp. 7402–7411, Dec. 2015.

[95] K. Yamazaki and Y. Seto, "Iron loss analysis of interior permanent-magnet synchronous motors-variation of main loss factors due to driving condition," *IEEE Trans. Ind. Appl.*, vol. 42, no. 4, pp. 1045–1052, Jul. 2006.

[96] Q. Wu, Y. Xu, Y. Liu, and S. Wei, "The influence analysis of resistance change to efficiency-optimization control for IPMSMs used in electric vehicle," in *25th Chinese Control and Decision Conference (CCDC)*, Guiyang, China, 2013, pp. 5189–5193.

[97] R. Dutta, L. Chong, and M. F. Rahman, "Analysis of CPSR in motoring and generating modes of an IPM motor," in *IEEE International Electric Machines & Drives Conference (IEMDC)*, Niagara Falls, ON, Canada, 2011, pp. 1474–1479.

[98] L. T. Beti and U. Schafer, "Loss minimization algorithm of an IPMSM based on analytical expressions," in *2014 16th European Conference on Power Electronics and Applications (EPE'14-ECCE Europe)*, Lappeenranta, Finland, 2014, pp. 1–7.

[99] Y. Yang *et al.*, "Thermal management of electric machines," *IET Electr. Syst. Transp.*, vol. 7, no. 2, pp. 104–116, Jun. 2017.

[100] A. A. Almeida, D. L. Rodrigues-Jr, L. S. P. Perassa, J. Leicht, and F. J. G. Landgraf, "Anomalous loss hysteresis loop," *Mater. Res.*, vol. 17, no. 2, pp. 494–497, Feb. 2014.

[101] D. Chen, B. Kwon, and B. Bai, "Selection of IGBTs for controlling rectifier and inverter based upon a novel analytical approach for loss calculation," in *2015 9th International Conference on Power Electronics and ECCE Asia (ICPE-ECCE Asia)*, Seoul, South Korea, 2015, pp. 1109–1115.

[102] A. D. Rajapakse, A. M. Gole, and P. L. Wilson, "Electromagnetic transients simulation models for accurate representation of switching losses and thermal performance in power electronic systems," *IEEE Trans. Power Deliv.*, vol. 20, no. 1, pp. 319–327, Jan. 2005.

[103] J. W. Kolar, "Losses in PWM inverters using IGBTs," *IEE Proc. - Electr. Power Appl.*, vol. 142, no. 4, p. 285, 1995.

[104] L. K. Mestha and P. D. Evans, "Analysis of on-state losses in PWM inverters," *IEE Proc. B Electr. Power Appl.*, vol. 136, no. 4, p. 189, 1989.

[105] A. I. Maswood, "A switching loss study in SPWM IGBT inverter," in *IEEE 2nd International Power and Energy Conference (PECon)*, Johor Bahru, Malaysia, 2008, pp. 609–613.

[106] D. Graovac and M. Pürschel, *IGBT power losses calculation using the data-sheet parameters - Infineon application note*. Automotive Power, Infineon, 2009.